First-Principles Study of Asymmetric Monolayer of Transition Metal Dichalcogenides and Related Nanostructures

Physics Final Year Project

Soh Yong Sheng A0098745L
Supervised by Professor Feng Yuan Ping

April 3, 2016

Abstract

Transition metal dichalcogenides (TMDs), with chemical formula MX_2, have gained interest in recent years due to their atomic thinness and remarkable properties, making them ideal candidates for nanodevices. However, there is no reason to believe that asymmetric TMDs (aTMDs), with chemical formula XMY, cannot exist. If stable and can be grown, the asymmetric structure may have unexpected properties and open new applications.

For example, due to different electronegativities of chalcogens X and Y, we expect a charge transfer from the less electronegative to more electronegative chalcogen, resulting in a dipole moment. Such dipole-dipole interactions, instead of weak Van der Waals interactions, can be used to stack up layers of aTMDs and lead to interesting properties for such superlattices. The different charge densities on different sides of aTMDs result in different surface properties, which may have new applications. Also, we expect different M-X and M-Y bond lengths to cause aTMDs to curl up naturally.

We propose to investigate flat, nanotube and spherical monolayer aTMDs from first-principles using density functional theory (DFT). The structures will be optimised according to parameters like lattice constant and radius of curvature. Then, we study their electronic properties and explore their potential applications.

Dedication

To my parents who taught me the love for nature, and Yan Ting who taught me the nature of love.

Declaration

This report is a presentation of my original research work. Wherever contributions of others are involved, every effort is made to indicate this clearly, with due reference to the literature, and acknowledgement of collaborative research and discussions. This work was done under the guidance of Professor Feng Yuan Ping at the National University of Singapore.

Acknowledgements

We thank the High Performance Cluster at the Centre for Advanced 2D Materials of the National University of Singapore for support of this work.

I want to thank my supervisor, professor Feng Yuan Ping, for his kind and patient supervision. No matter how busy he is, he always makes time for weekly discussions, during which he provides very good insights and directions. Without him, this project would have been impossible.

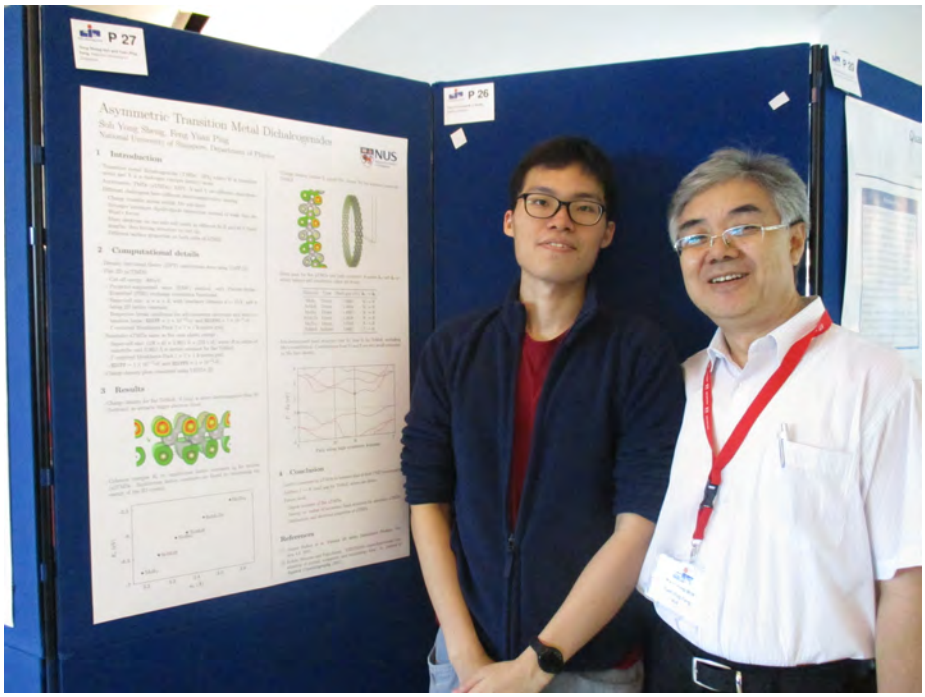

Figure 1: Professor Feng and I beside our poster during the Institute of Physics Singapore Meeting 2016 on 8 March.

Contents

Chapter 1

Introduction

In recent years, 2D materials like graphene and TMDs have garnered strong interest. Their atomic thinness makes them candidate materials for many nanodevices. TMDs have emerged as promising 2D materials with exceptional physical behaviours [26] that are distinct from graphene. Though graphene has a high carrier mobility [6], it lacks a direct band gap and graphene transistors cannot be switched off. On the other hand, due to quantum confinement, TMDs have direct band gaps [17], which make them potential candidates for transistors and optoelectronic devices. Moreover, TMDs have modest mobility and excellent on-off ratio in field effect transistors [23] comparable to thin silicon films, are strong and flexible [2], and are tunable under strain [12]. These properties make TMDs excellent candidates for flexible electronics.

However, to the best of our knowledge, no work has been done on aTMDs yet. Symmetric TMDs have a chemical formula of MX_2, with the M transition metal sub-layer being sandwiched by 2 X chalcogen sub-layers. aTMDs have the chemical formula XMY and are sandwiched by 2 different chalcogen sub-layers. Figure 2.4 shows the structure for TeMoS, which is an example of a aTMD.

The motivation for studying aTMDs is as follows: First, due to the different electronegativities of the 2 different chalcogen sub-layers, we expect a charge transfer across the middle Mo sub-layer from the less to more electronegative chalcogen sub-layer. For example, according to table 2.1, Te is less electronegative than S. Therefore, we expect some charge transfer from Te to S in TeMoS as shown in figure 1.1. This creates a dipole moment and stronger inter-layer dipole-dipole interactions. In contrast, symmetric TMDs do not have such dipole moments and reply on weak inter-layer Van der Waal's forces to hold different layers together. Stronger inter-layer dipole-dipole interactions may result in new properties of 2D superlattices formed by sandwiching different types of aTMDs.

Second, the different charge densities on different sides of a aTMD monolayer will result in different surface properties. For example, a floating electrophilic oxygen molecule approaching a TeMoS monolayer may be more strongly attracted to the more electron-rich S side as compared to the electron-poor Te

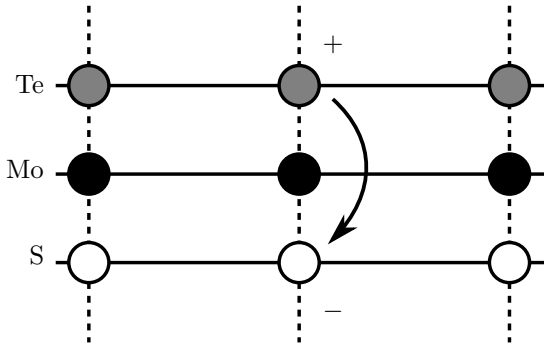

Figure 1.1: Charge transfer from the less electronegative Te ion to the more electronegative S ion results in an internal electric field and dipole moment for monolayer TeMoS.

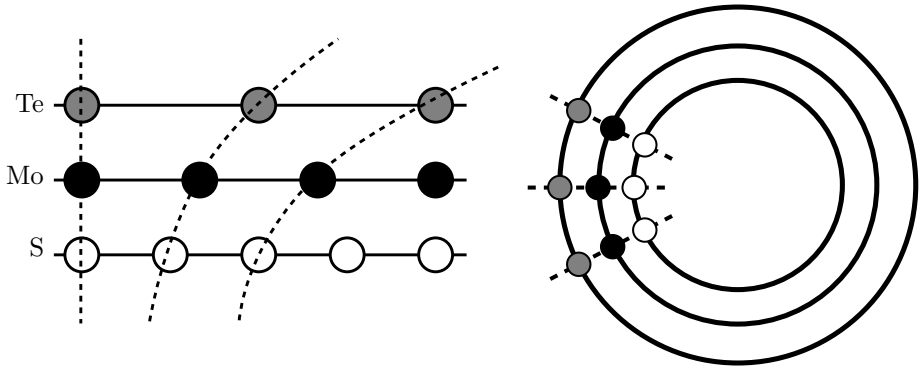

Figure 1.2: The less electronegative Te atom has larger radius than Se atom. Forcibly bonding the Te and S atoms to the Mo atom them using dotted lines will force the TeMoS monolayer to curl up into a sphere.

side. Such dual surface properties may lead to new applications.

Third, the difference in electronegativities of the 2 chalcogens X and Y results in different M-X and M-Y bond lengths. This causes the structure to curl up, as shown in figure 1.2. We thus expect aTMDs to be naturally spherical instead of flat like symmetric TMDs. Rolling naturally flat structures, like graphene and symmetric TMDs, into nanotubes and spherical shell structures may introduce significant strain. The natural radius of curvature in aTMDs may make aTMDs better candidates for fabricating nanotubes and spherical shell structures.

In this work, we investigate aTMDs such as SeMoS, SeMoTe and TeMoS from first-principles using DFT. However, we give TeMoS special attention because it has the highest asymmetry. We also expect TeMoS to have the smallest radius of curvature, thereby reducing the number of atoms of a unit cell of a nanotube or spherical shell structure. This reduces the cost involved in DFT

treatment and makes TeMoS most convenient to analyse. The structures (flat 2D, nanotube and spherical) of aTMDs will be optimised and their stability will be analysed first. For stable structures identified from the stability analysis, we carry out first-principles calculations to study their electronic properties and explore their potential applications. All DFT treatment is done using a software package called VASP [9]. Ball and stick structures are drawn using Materials Studio [15], and charge densities are visualised using VESTA [20] and VaspView [25]. Data is processed and plotted using GNU Octave [5].

Chapter 2

Background

2.1 Structures of MoS_2

MoS_2 is a well-known example of a traditional, symmetric TMD. As such, we use the example of MoS_2 to discuss the structure of symmetric TMDs. Figures 2.1 and 2.2 show the possible structures of molybdenum disulphide MoS_2. MoS_2 is made up of layers that are held together by weak Van der Waals forces; these layers can thus slide over each other easily like layers of graphene in graphite. Unlike graphene however, each layer of MoS_2 is constructed by laying 3 sub-layers of atoms as shown in figure 2.3. There are two resulting structures for a MoS_2 layer – 2H (figure 2.1) and 1T(figure 2.2). The 2H structure is more commonly found in nature [13].

To generate a layer, one can use the 2D Bravais hexagonal lattice defined by the primitive lattice vectors $\mathbf{a}_1$ and $\mathbf{a}_2$ and the angle ϕ between them:

$$|\mathbf{a}_1| = |\mathbf{a}_2| = a, \tag{2.1}$$

$$\phi = 2\pi/3. \tag{2.2}$$

In Cartesian coordinates, they are

$$\mathbf{a}_1 = -a\left(\frac{1}{2}\hat{\mathbf{x}} + \frac{\sqrt{3}}{2}\hat{\mathbf{y}}\right), \tag{2.3}$$

$$\mathbf{a}_2 = a\hat{\mathbf{x}}. \tag{2.4}$$

The corresponding reciprocal lattice vectors are

$$\mathbf{b}_1 = -\frac{4\pi}{\sqrt{3}a}\hat{\mathbf{y}}, \tag{2.5}$$

$$\mathbf{b}_2 = \frac{4\pi}{\sqrt{3}a}\left(\frac{\sqrt{3}}{2}\hat{\mathbf{x}} - \frac{1}{2}\hat{\mathbf{y}}\right), \tag{2.6}$$

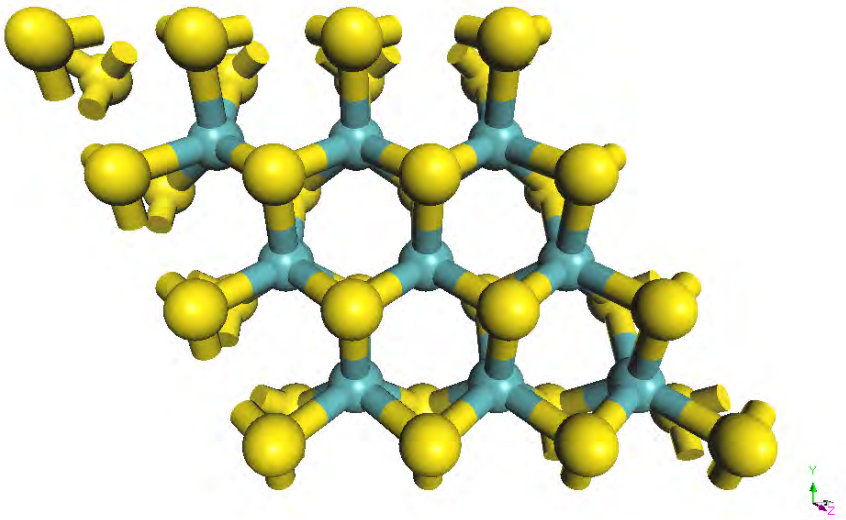

(a) Top down view.

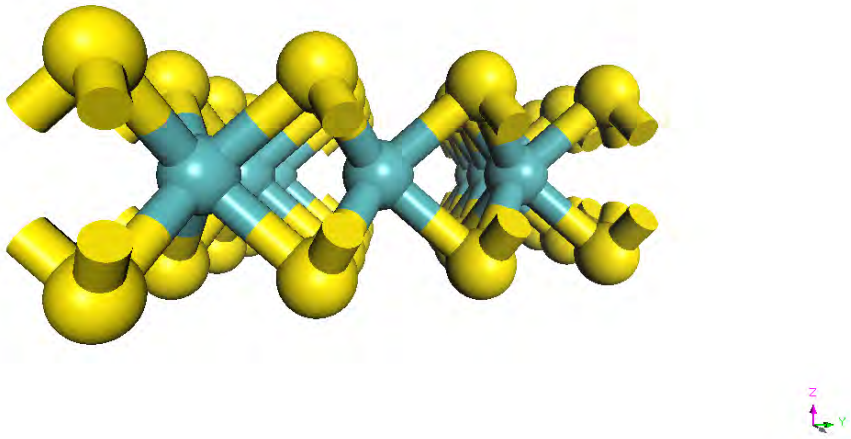

(b) Side view.

Figure 2.1: 2H structure for monolayer MoS_2, where bottom and top S atoms (yellow spheres) are aligned together such that their projections onto the x-y plane overlap. A middle Mo atom (blue sphere) bonded to 6 S atoms forms a trigonal prismatic molecular geometry.

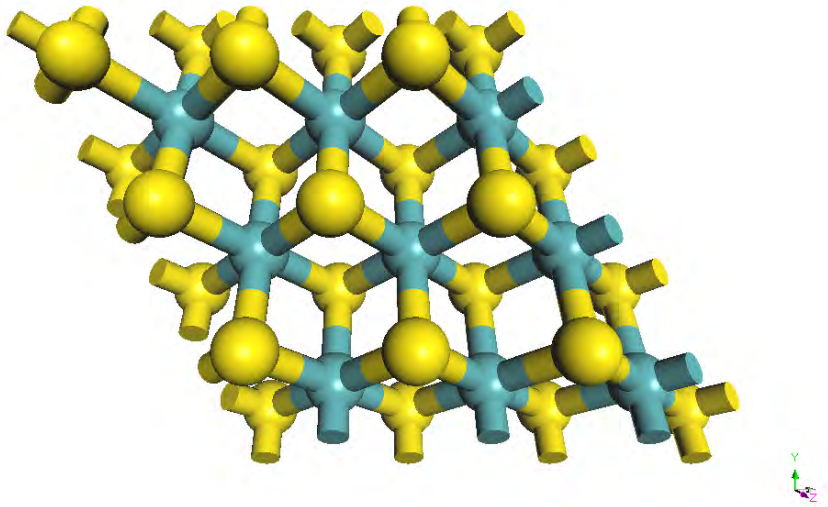

(a) Top down view.

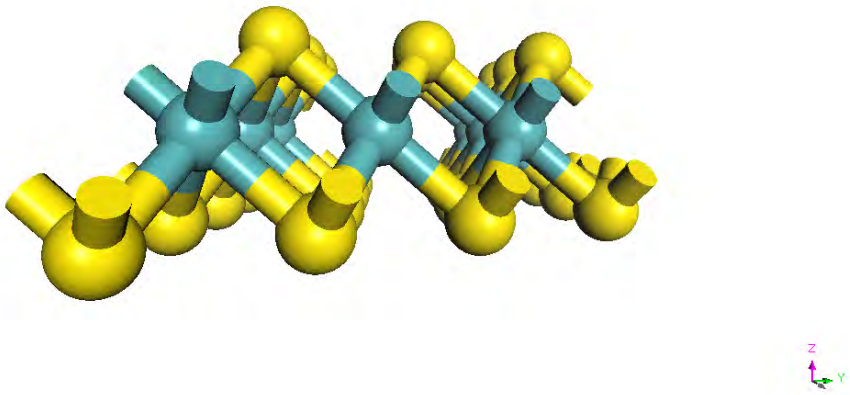

(b) Side view.

Figure 2.2: 1T structure for monolayer MoS_2, where bottom and top S atoms (yellow spheres) are not aligned together, i.e. their projections on the x-y plane do not overlap. A middle Mo atom (blue sphere) bonded to 6 S atoms forms a octahedral molecular geometry.

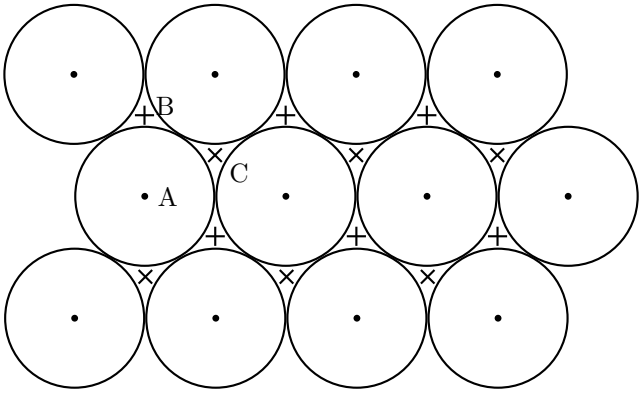

Figure 2.3: The first layer of spheres with centres marked A are the S atoms. A second layer of Mo atoms can be placed over points marked B. The third layer of S atoms can over either A or C, making the sequence ABA or ABC. The sequence ABA corresponds to the 2H structure in figure 2.1; the sequence ABC corresponds to the 1T structure in figure 2.2.

and can verified to be correct using

$$\mathbf{b}_i \cdot \mathbf{a}_j = 2\pi\delta_{ij}. \tag{2.7}$$

The primitive cell is thus a rhombus made up of 2 equilateral triangles. By picking any one of its 4 vertices as a lattice point, and duplicating another lattice point $\mathbf{T}(u_1, u_2)$ away for all integers u_1, u_2, where

$$\mathbf{T} = u_1\mathbf{a}_1 + u_2\mathbf{a}_2, \tag{2.8}$$

we generate an infinitely large sheet of lattice points arranged in the hexagonal way.

For the 2H structure of MoS_2, we attach 2 S atoms and 1 Mo atom to every lattice point in the following relative positions:

$$\mathbf{r}(\text{bottom S}) = 0, \tag{2.9}$$

$$\mathbf{r}(\text{middle Mo}) = \frac{1}{3}\mathbf{a}_1 + \frac{2}{3}\mathbf{a}_2 + \frac{1}{2}\mathbf{d}, \tag{2.10}$$

$$\mathbf{r}(\text{top S}) = \mathbf{d}, \tag{2.11}$$

where $|\mathbf{d}| = d$ is the distance between the bottom and top S atoms and $\mathbf{d}$ points in the $\hat{\mathbf{z}}$ direction.

For the 1T structure, we change the relative position of the top S atom to

$$\mathbf{r}(\text{top S}) = \frac{2}{3}\mathbf{a}_1 + \frac{1}{3}\mathbf{a}_2 + \mathbf{d} \tag{2.12}$$

while keeping the relative positions of bottom S and middle Mo the same in (2.10) and (2.11).

Table 2.1: Electronegativities [28] of S, Se and Te in Pauling units. The electronegativities of S and Se are quite close, whereas the electronegativity of Te is much less than those of S and Se.

S	Se	Te
2.58	2.55	2.01

2.2 Structure of aTMDs

For our study of aTMDs, we use the 2H symmetric TMD structure and replace one of the chalcogen sub-layer with another chalcogen type. For example, in TeMoS shown in figure 2.4, we replace the bottom sub-layer of S atoms of MoS_2 with Te atoms. In this work, all aTMDs are of the 2H structure; the 2H structure is more stable and more commonly found in nature than the 1T structure [13].

2.3 Electronegativities of chalcogens

Since we expect the interesting properties of aTMDs to come from the difference in electronegativities of the different chalcogen sub-layers, it is useful to first find these electronegativity values from current literature. The electronegativities of S, Se and Te are tabulated in table 2.1. We find that the electronegativities of S and Se are quite close, whereas the electronegativity of Te is much less than those of S and Se. Hence, we expect TMDs MoS_2, $MoSe_2$ and aTMD SeMoS to have similar properties.

2.4 Density functional theory

DFT searches for density distribution $n(\mathbf{r})$ of electrons and ions that minimises energy, similar to the variational principle; the density functional in "density functional theory" refers to the energy functional to be minimised. We first assume that the ions are fixed in position, whereas the electrons are free to move. This assumption is valid because the ions are much more massive than the electrons, and the ions move much more slowly than the electrons. This assumption, where the electrons react instantaneously to the change in ionic positions, is known as the Born-Oppenheimer approximation. In Hartree units, the electron charge density used to minimise energy is thus

$$n(\mathbf{r}) = \left|\Psi(\mathbf{r_1}, \mathbf{r_2}, \ldots, \mathbf{r_N})\right|^2, \tag{2.13}$$

where $\Psi(\mathbf{r_1}, \mathbf{r_2}, \ldots, \mathbf{r_N})$ is the all-electron wavefunction for N electrons. Within the Born-Oppenheimer approximation, the many-particle eigenvalue problem becomes

$$\left(\sum_{i=1}^{N}\left(-\frac{1}{2}\boldsymbol{\nabla}_i^2 + V_n(\mathbf{r}_i)\right) + \frac{1}{2}\sum_{i\neq j}\frac{1}{|\mathbf{r}_i - \mathbf{r}_j|}\right)\Psi = E\Psi, \tag{2.14}$$

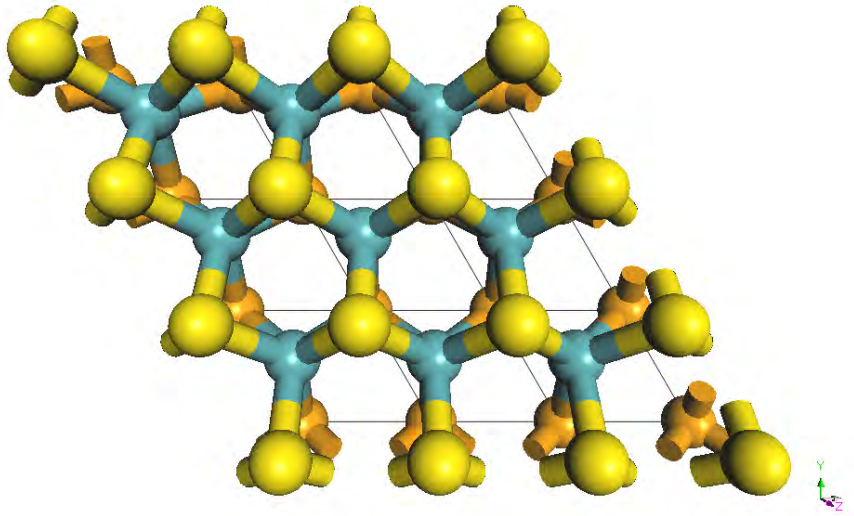

(a) Top down view.

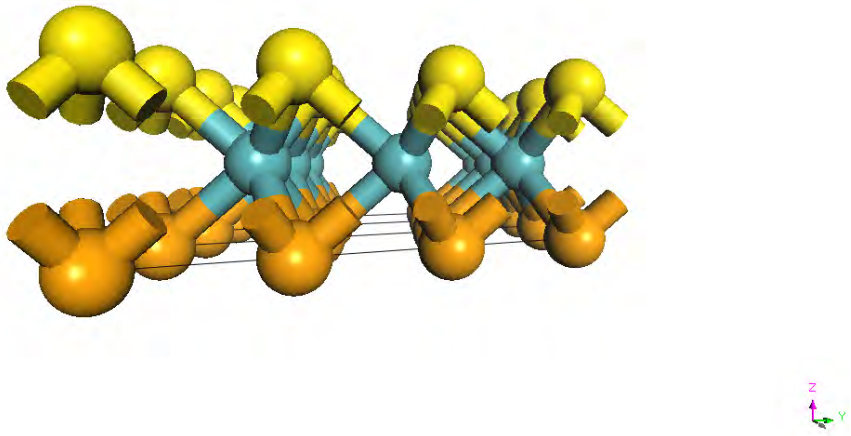

(b) Side view.

Figure 2.4: 2H structure of a layer of aTMD TeMoS, where the bottom brown sub-layer of atoms are Te atoms, the middle blue sub-layer of atoms are Mo atoms, and the top yellow sub-layer of atoms are S atoms. Generated by Materials Studio [15]. All other aTMDs in this work are of the 2H structure.

where

$$V_n(\mathbf{r}_i) = -\sum_I \frac{Z_I}{|\mathbf{r}_i - \mathbf{R}_I|} \tag{2.15}$$

is the external potential energy between the i-th electron and all the ions.

In the independent electron approximation, where electrons do not see one another, we drop the term describing the Coulomb repulsion among electrons

$$\sum_{i=1}^{N} \left(-\frac{1}{2}\boldsymbol{\nabla}_i^2 + V_n(\mathbf{r}_i) \right) \Psi = \sum_{i=1}^{N} H_0(\mathbf{r}_i)\Psi \tag{2.16}$$

$$= E\Psi, \tag{2.17}$$

and express the all-electron wavefunction as a product of N single-electron wavefunctions $\phi_i(\mathbf{r}_i)$:

$$\Psi(\mathbf{r_1}, \mathbf{r_2}, \ldots, \mathbf{r_N}) = \phi_1(\mathbf{r}_1)\phi_2(\mathbf{r}_2)\ldots\phi_N(\mathbf{r}_N). \tag{2.18}$$

Substituting the above expression into the right-hand side of (2.16), and using the fact that $H_0(\mathbf{r}_i)$ only acts on $\phi_i(\mathbf{r}_i)$, the N-particle eigenvalue problem in (2.16) reduces to N single-particle equations:

$$H_0(\mathbf{r})\phi_i(\mathbf{r}) = \epsilon_i\phi_i(\mathbf{r}) \quad \text{for } i = 1, 2, \ldots, N. \tag{2.19}$$

The energy of the system is

$$E = \epsilon_1 + \epsilon_2 + \cdots + \epsilon_N. \tag{2.20}$$

The greatest strength of this drastic approximation is that it reduces the N-particle eigenvalue problem to N single-particle eigenvalue problems. However, there are two serious shortcomings. First, electrons are fermions and according to Pauli's exclusion principle, the all-electron wavefunction Ψ must change sign if we exchange the position coordinates of any 2 electrons. The all-electron wavefunction should thus be written as the Slater determinant

$$\Psi(\mathbf{r_1}, \mathbf{r_2}, \ldots, \mathbf{r_N}) = \frac{1}{\sqrt{N!}} \begin{vmatrix} \phi_1(\mathbf{r}_1) & \phi_1(\mathbf{r}_2) & \ldots & \phi_1(\mathbf{r}_N) \\ \phi_2(\mathbf{r}_1) & \phi_2(\mathbf{r}_2) & \ldots & \phi_2(\mathbf{r}_N) \\ \vdots & \vdots & \ddots & \vdots \\ \phi_N(\mathbf{r}_1) & \phi_N(\mathbf{r}_2) & \ldots & \phi_N(\mathbf{r}_N) \end{vmatrix}, \tag{2.21}$$

so that the determinant changes sign whenever we exchange 2 rows or columns. Second, the magnitude of inter-electron Coulomb repulsion is comparable to other terms and we cannot neglect it.

Using the correct all-electron wavefunction in (2.21) for the Schrodinger equation in (2.14) that includes the inter-electron Coulomb repulsion, we now instead have the Kohn-Sham equations

$$\left(-\frac{1}{2}\boldsymbol{\nabla}^2 + V_n(\mathbf{r}) + V_{\mathrm{H}}(\mathbf{r}) + V_{\mathrm{xc}}(\mathbf{r}) \right) \phi_i(\mathbf{r}) = \epsilon_i\phi_i(\mathbf{r}), \tag{2.22}$$

which are inspired by the convenient but inaccurate independent electron approximation to reduce the N-particle eigenvalue problem to N single-particle eigenvalue problems.

The Hartree energy $V_{\mathrm{H}}(\mathbf{r})$ describes the potential energy an electron immersed in a electrostatic potential caused by other electrons:

$$V_{\mathrm{H}}(\mathbf{r}) = \int \frac{\mathrm{d}Q(\mathbf{r}')}{|\mathbf{r} - \mathbf{r}'|} \tag{2.23}$$

$$= \int \frac{n(\mathbf{r}')\,\mathrm{d}^3\mathbf{r}'}{|\mathbf{r} - \mathbf{r}'|}, \tag{2.24}$$

which satisfies the Poisson equation

$$\boldsymbol{\nabla}^2 V_{\mathrm{H}} = -4\pi n(\mathbf{r}). \tag{2.25}$$

The exchange-correlation energy $V_{\mathrm{xc}}(\mathbf{r})$ is the quantum correction needed when transforming the many-particle problem (defined by the Slater determinant) into the single particle picture. Hence, the many-body effect is included in the $V_{\mathrm{xc}}(\mathbf{r})$ term. The exchange correlation term is also a functional of electron density, i.e.

$$V_{\mathrm{xc}} = V_{\mathrm{xc}}[n(\mathbf{r})]. \tag{2.26}$$

We note that the Kohn-Sham energy functional in the left-hand side of (2.22) is a functional of charge density $n(\mathbf{r})$, i.e.

$$F[n] = -\frac{1}{2}\boldsymbol{\nabla}^2 + V_n[n] + V_{\mathrm{H}}[n] + V_{\mathrm{xc}}[n], \tag{2.27}$$

yet they determine the charge density through the Kohn-Sham orbitals $\phi_i(\mathbf{r})$ in (2.22):

$$n(\mathbf{r}) = \sum_{i=1}^{N} |\phi_i(\mathbf{r})|^2. \tag{2.28}$$

This points towards a self-consistent method in solving the Kohn-Sham equations. Algorithm 1 illustrates this.

Data: fixed ionic positions $\mathbf{R_I}$
Result: electron charge density $n(\mathbf{r})$
compute external potential $V_n(\mathbf{r}) = -\sum_I Z_I/|\mathbf{r} - \mathbf{R}_I|$;
guess $n(\mathbf{r})$;
do
  compute Hartree potential $\boldsymbol{\nabla}^2 V_{\mathrm{H}}[n] = -4\pi n(\mathbf{r})$;
  compute exchange-correlation potential $V_{\mathrm{xc}}[n]$;
  find $V_{\mathrm{tot}} = V_n + V_{\mathrm{H}} + V_{\mathrm{xc}}$;
  solve single particle eigenvalue problem (Kohn-Sham equations)
  $\left((-\boldsymbol{\nabla}^2/2) + V_{\mathrm{tot}}[n]\right)\phi_i(\mathbf{r}) = \epsilon_i\phi_i(\mathbf{r})$;
  get new charge density $n(\mathbf{r}) = \sum_i |\phi_i(\mathbf{r})|^2$;
while *new* $n(\mathbf{r}) \neq$ *old* $n(\mathbf{r})$;
return self-consistent electron charge density $n(\mathbf{r})$ and ground state energy $E = \sum_i \epsilon_i$;

Algorithm 1: Self-consistent electronic calculation to solve Kohn-Sham equations in (2.22).

Chapter 3

Methodology

3.1 Flat TMDs and aTMDs

3.1.1 Equilibrium lattice parameters

The equilibrium lattice parameter a_0 is the lattice parameter $a = |\mathbf{a_1}| = |\mathbf{a_2}|$ that minimises the energy of a (a)TMD monolayer ((a)TMD means symmetric TMDs or aTMDs). We simulate an isolated monolayer by stacking many monolayers vertically with a large enough separation, i.e. for a monolayer spanning the x-y plane, the vertical distance along the z-axis between two monolayers is sufficiently large to approximate the physics of a truly isolated monolayer surrounded by infinite vacuum. We thus use a super-cell defined by primitive lattice vectors $\mathbf{a}_1$ and $\mathbf{a}_2$, as well as $\mathbf{a}_3$, which characterises the vertical distance between two far-apart monolayers. We choose $|\mathbf{a}_3| = 15\,\text{Å}$.

For a certain lattice parameter a, we allow the atoms to relax freely and be influenced by the forces acting on them using the conjugate gradient method. For each set of atomic positions in this relaxation, we use the Born-Oppenheimer approximation to determine the electron wavefunctions in a self-consistent way. Algorithm 3 illustrates this succinctly, while table 3.1 shows the relevant computational details.

3.1.2 Average cohesive energies per atom

We can obtain the average cohesive energy per atom E_c using

$$E_\text{c} = \left(F_0 - \sum_\alpha F_\alpha \right) \Big/ N_\text{I} \,, \tag{3.1}$$

where F_0 is the total equilibrium energy for the super-cell, α is the type of single atom, F_α is the total energy for the α single atom and N_I is the number of atoms in the super-cell. Using the self-consistent electronic relaxation treatment for fixed single atoms placed sufficiently far apart, we obtain the total energies F_α for $\alpha = \text{Mo}, \text{S}, \text{Se}, \text{Te}$.

Data: initial ionic positions and electronic charge density
Result: equilibrium ionic positions, charge density n and energy F per super-cell
compute forces on ions based on Coulomb interaction with electron charge density n and with another ions;
move ions according using conjugate gradient method using computed forces;
while *ions still move* **do**
    guess electron wavefunction for new set of atomic positions;
    while *electron wavefunction not converged* **do**
        continue with self-consistent electronic calculation using algorithm 1;
    end
    compute forces on ions based on Coulomb interaction with electron charge density n and with another ions;
    move ions according using conjugate gradient method using computed forces;
end
compute energy F per super-cell;
return equilibrium ionic positions, n and F;

Algorithm 2: Both electronic and ionic relaxations.

Result: equilibrium lattice parameter a_0
foreach *lattice parameter* a **do**
    relax ionic and electronic charge density using algorithm 2
end
plot energy F per super-cell vs. a;
fit a quadratic curve to points near the lowest energy;
return value of a corresponding to minimum point of quadratic fit;

Algorithm 3: Atomic relaxation to obtain equilibrium lattice parameter a_0.

Table 3.1: DFT parameters for flat 2D monolayers, where a is the trial lattice parameter; E_{cut} is the cut-off energy; `EDIFF` and `EDIFFG` are the break conditions for self-consistent electronic and ionic relaxation loops respectively.

Pseudo-potential	Projector-augmented wave method [3]
Exchange-correlation functional	Perdew-Burke-Ernzerhof [21]
E_{cut}	$400\,\text{eV}$
Super-cell dimensions	$a \times a \times 15\,\text{Å}$
Ionic relaxation method	Conjugate gradient descent
`EDIFF`	$1 \times 10^{-6}\,\text{eV}$
`EDIFFG`	$1 \times 10^{-5}\,\text{eV}$
k-points mesh	Γ-centered Monkhorst-Pack $7 \times 7 \times 1$

3.1.3 Bader analysis

To quantify the charge transfer from the less to more electronegative chalcogen in aTMDs, we need a way of dividing the charge density amongst ions. An intuitive way of doing so is to use the 2D surface on which the charge density is minimum perpendicular to this surface. Such surfaces are called zero flux surfaces by Bader [1]. Using the algorithm and program developed by Henkelman's group [14], we divide the charge density and volume of a unit cell and assign them to the constituent ions.

3.1.4 Dipole moment

Another way of quantifying the charge transfer in flat aTMDs is to get the dipole moment $\mathbf{p}$ associated with the charge asymmetry. For TeMoS, in units of the elementary charge,

$$\mathbf{p} = \hat{\mathbf{z}} \int_{-\infty}^{\infty} \big(n(z) + 6\delta(z - z_{\mathrm{S}}) + 6\delta(z - z_{\mathrm{Mo}}) + 6\delta(z - z_{\mathrm{Te}})\big) z \, \mathrm{d}z, \tag{3.2}$$

$$= \hat{\mathbf{z}} \left(\left(\int_{-\infty}^{\infty} n(z) \, \mathrm{d}z \right) + 6z_{\mathrm{S}} + 6z_{\mathrm{Mo}} + 6z_{\mathrm{Te}} \right) \tag{3.3}$$

where 6 comes from the effective nuclear charge of the ions (Te, Mo, S all have 6 valence electrons),

$$z_{\mathrm{S}} = \mathbf{r}(\mathrm{S}) \cdot \hat{\mathbf{z}}, \tag{3.4}$$

and likewise for z_{Mo} and z_{Te}, and n is the *negative* electron charge density with

$$n(z) = \iint_S n(x, y, z) \, \mathrm{d}x \, \mathrm{d}y < 0, \tag{3.5}$$

and S is the area of the primitive unit cell. The dipole moment points from the *negative to positive* charge. Since we expect the more electronegative chalcogen to attract more negative electron charge, the dipole moment should point from the more to less electronegative chalcogen in aTMDs. On the other hand, we expect no dipole moment for symmetric TMDs.

3.2 Spherical aTMDs

The difference in equilibrium lattice parameters for different chalcogens in symmetric TMDs MoS_2, $MoSe_2$ and $MoTe_2$ in figure 4.3 suggests that flat 2D aTMDs are not energetically stable. For example, in TeMoS, the larger Te atoms push against one another and the smaller S atoms pull on one another. This tension at the S side and compression at the Te side will cause a flat piece of TeMoS to curl up into a sphere. We need to first estimate the radius of such a sphere, map the ionic positions from the flat structure to the sphere and then relax the structure using DFT treatment.

Figure 3.1 illustrates the curling of a aTMD to form a sphere. The radius

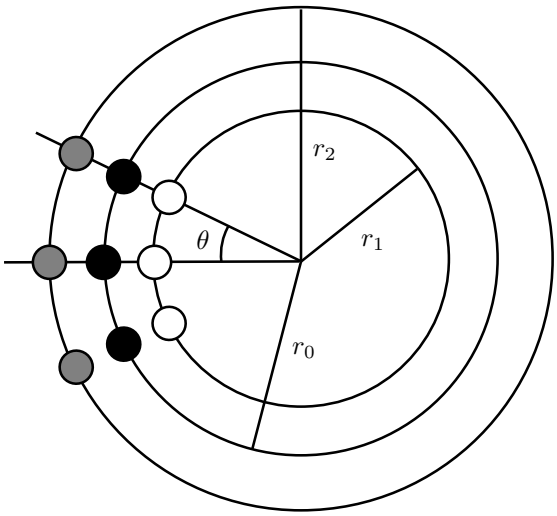

Figure 3.1: Spherical aTMD formed due to different sizes of chalcogens. The three layers are formed by the smaller chalcogen, the middle transition metal and larger chalcogen, with radii r_1, r_0 and r_2 respectively. The angle subtended by two adjacent atoms is θ.

of curvature is estimated by

$$\frac{r_2\theta}{r_1\theta} = \frac{a_0^{(2)}}{a_0^{(1)}}, \tag{3.6}$$

where $a_0^{(2)}$ and $a_0^{(1)}$ are the distances between two adjacent chalcogen atoms on the outer and inner sphere respectively. Letting

$$r_1 + d = r_2, \tag{3.7}$$

we have

$$r_1 = \frac{d}{\left(a_0^{(2)}/a_0^{(1)}\right) - 1}. \tag{3.8}$$

For TeMoS, we assume the distance between two adjacent S atoms to be that of the equilibrium lattice constant for that of MoS_2, and likewise for the outer Te atoms and $MoTe_2$. Referring to table 4.1, this means

$$a_0^{(2)} = a_0(\mathrm{MoTe_2}) = 3.552\,\text{Å}, \tag{3.9}$$

$$a_0^{(1)} = a_0(\mathrm{MoS_2}) = 3.185\,\text{Å}. \tag{3.10}$$

The sphere's thickness d is obtained from the equilibrium vertical distance between the Te and S atom found from the equilibrium electron and ion distributions in figure 4.6:

$$d = 3.373\,\text{Å}. \tag{3.11}$$

Substituting the above values into (3.8) and (3.7), we get r_1 and r_2 shown in table 3.2. The radius of the middle sphere for the Mo ions can be obtained from

$$r_1 + c = r_0, \tag{3.12}$$

where c, similar to d, is the equilibrium vertical distance between the S and Mo atom found when drawing figure 4.6.

Algorithm 4 outlines the steps of mapping ionic positions from a flat aTMD to a sphere. The main idea is to create a sphere made of triangles [18], also

```
Result: initial ionic positions for spherical aTMDs
/* 3 layers:  inner, middle and outer spheres                */
foreach layer do
    /* regular octahedron is a polyhedron made of 8
       equilateral triangles of the same size                 */
    draw a regular octahedron;
    foreach octahedron face do
        divide octahedron face into f rows of sub-triangles;
        /* to obtain geodesic sphere                          */
        set radial component of every vertex of sub-triangle to same
        radius r of this layer;
    end
    if layer is inner or outer sphere then
        foreach sub-triangle vertex do
            place chalcogen ion;
        end
    else
        /* layer is middle layer                              */
        for every alternate sub-triangle do
            place metal ion in the middle of sub-triangle;
        end
    end
end
return ionic positions for all 3 layers;
```

Algorithm 4: Initialising ionic positions of a spherical aTMD. The different ways of placing the chalcogens and metal ion ensures most of the metal ions to form the trigonal prismatic geometry with 6 other chalcogen ions.

known as a geodesic sphere, and to use the triangles to place the ions. The primitive cell for the 2D hexagonal lattice comprises 2 equilateral triangles. However, the highest regular polyhedron made up of equilateral triangles we can have is the 20-faced icosahedron; anything higher is at best made up of *approximately* equilateral triangles. Nevertheless, this is merely an initialisation of the ionic positions, and we only need an estimate of the ionic positions for now; the precise ionic positions will be determined after DFT relaxation.

Table 3.2: Key parameters of initial ionic positions for optimal TeMoS. r is radius of geodesic sphere, f is frequency of which the octahedron faces are subdivided into smaller triangles, N is number of atoms on a sphere, $\langle a \rangle$ is the average distance between two atoms of the same sphere, and the subscripts 0, 1 and 2 denote the middle, inner and outer sphere respectively.

r_0	30.727 Å
r_1	29.255 Å
r_2	32.628 Å
f	18
N_0	1296
$N_1 = N_2$	1714
$\langle a \rangle_0$	3.072 Å
$\langle a \rangle_1$	3.227 Å
$\langle a \rangle_2$	3.426 Å

Because TeMoS has the largest difference between chalcogen sizes as compared to SeMoS and SeMoTe, its radius of curvature is smallest and thus the number of atoms involved for DFT computation is also smallest. Hence, we shall focus on TeMoS for concrete calculations. Table 3.2 tabulates the parameters characterising the geodesic spheres for initialising the spherical TeMoS.

The frequency f in table 3.2 refers to the number of rows of smaller sub-triangles which a regular octahedron's face (an equilateral triangle) is divided to. The number of smaller sub-triangles in an octahedron face is thus f^2. If we consider the half of the sphere's circumference to be made of 2 adjacent octahedron faces, then we have

$$2 \times f \times \frac{\sqrt{3}}{2} a = \pi r, \tag{3.13}$$

where r is the radius of the sphere.

Figures 3.2 and 3.3 plot the initial ionic positions for spherical TeMoS.

However, the large number of atoms involved

$$N_0 + N_1 + N_2 = 4724 \tag{3.14}$$

makes DFT treatment too expensive. Instead, we decrease the radius by 8 times to reduce the number of atoms. The key parameters for such a drastically reduced scheme is shown in table 3.3. Although the huge decrease in radius will result in significant strain, the number of atoms involved in DFT computation is now

$$N_0 + N_1 + N_2 = 112, \tag{3.15}$$

much smaller than 4724 atoms in the optimal structure. Figures 3.4 and 3.5 plot the initial atomic positions for the reduced spherical TeMoS, and these are left to relax based on algorithm 2 and table 3.4.

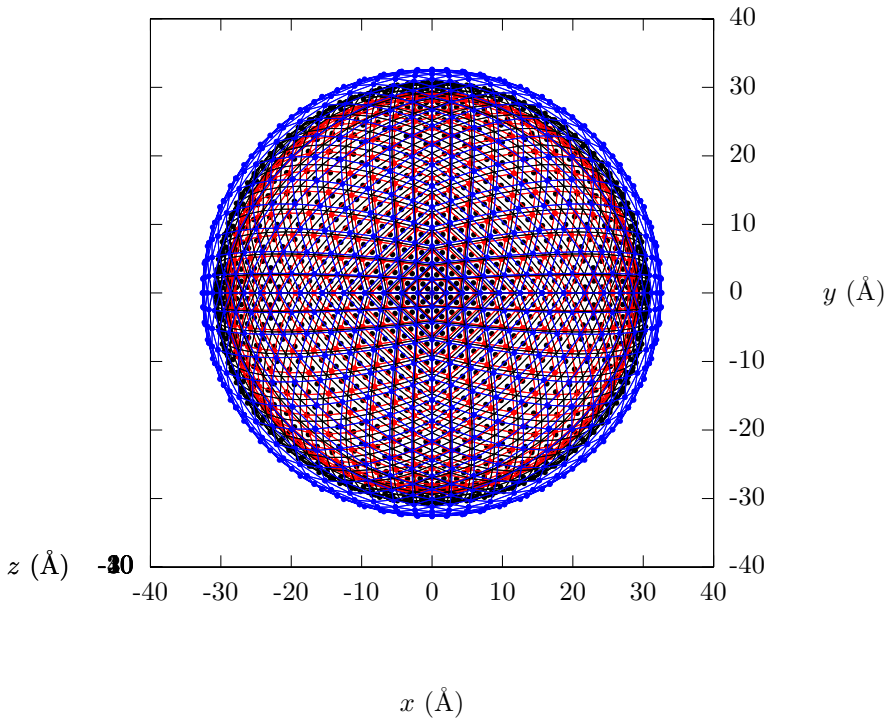

Figure 3.2: Initial atomic positions for *optimal* spherical TeMoS for ionic and electronic relaxations. The inner, middle and outer spheres comprise S (red), Mo (black) and Te (blue) atoms respectively.

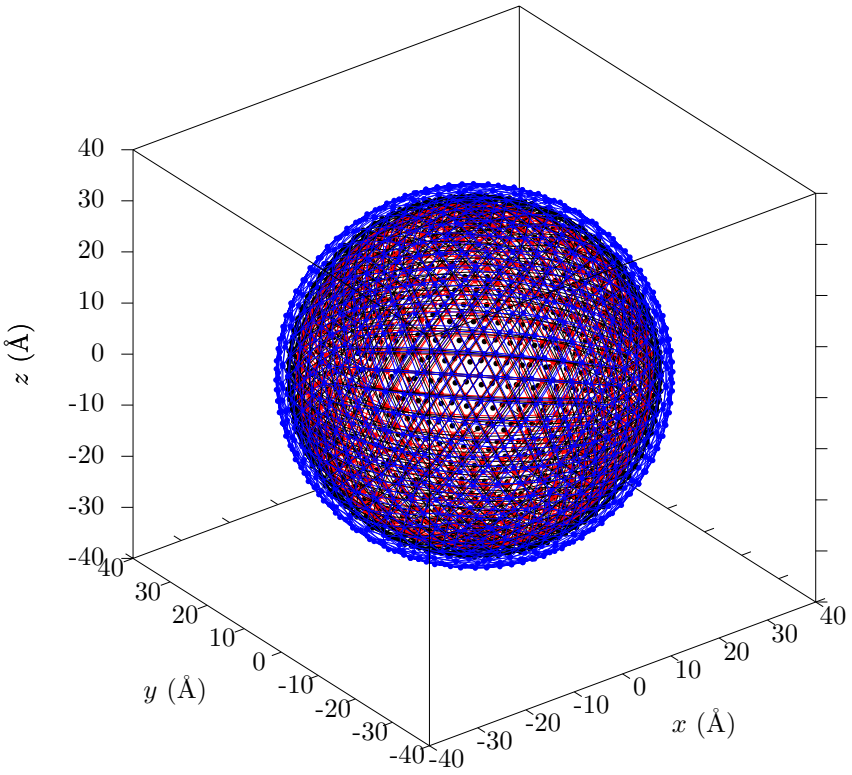

Figure 3.3: Different view of initial atomic positions for *optimal* spherical TeMoS.

Table 3.3: Key parameters of initial ionic positions for *reduced* TeMoS. r is radius of geodesic sphere, f is frequency of which the octahedron faces are subdivided into smaller triangles, N is number of atoms on a sphere, $\langle a \rangle$ is the average distance between two atoms of the same sphere, and the subscripts 0, 1 and 2 denote the middle, inner and outer sphere respectively.

r_0	5.129 Å
r_1	3.657 Å
r_2	7.030 Å
f	3
N_0	36
$N_1 = N_2$	38
$\langle a \rangle_0$	3.136 Å
$\langle a \rangle_1$	2.236 Å
$\langle a \rangle_2$	4.298 Å

Table 3.4: DFT parameters for *reduced* spherical TeMoS, where r_0 is the estimated radius of curvature; 15 Å is the distance between two spherical surfaces; E_{cut} is the cut-off energy; `EDIFF` and `EDIFFG` are the break conditions for self-consistent electronic and ionic relaxation loops respectively.

Pseudo-potential	Projector-augmented wave method [3]
Exchange-correlation functional	Perdew-Burke-Ernzerhof [21]
E_{cut}	400 eV
Super-cell dimensions	$(2r_0 + 15\,\text{Å}) \times (2r_0 + 15\,\text{Å}) \times (2r_0 + 15\,\text{Å})$
Ionic relaxation method	Conjugate gradient descent
`EDIFF`	1×10^{-4} eV
`EDIFFG`	1×10^{-3} eV
k-points mesh	Γ point only

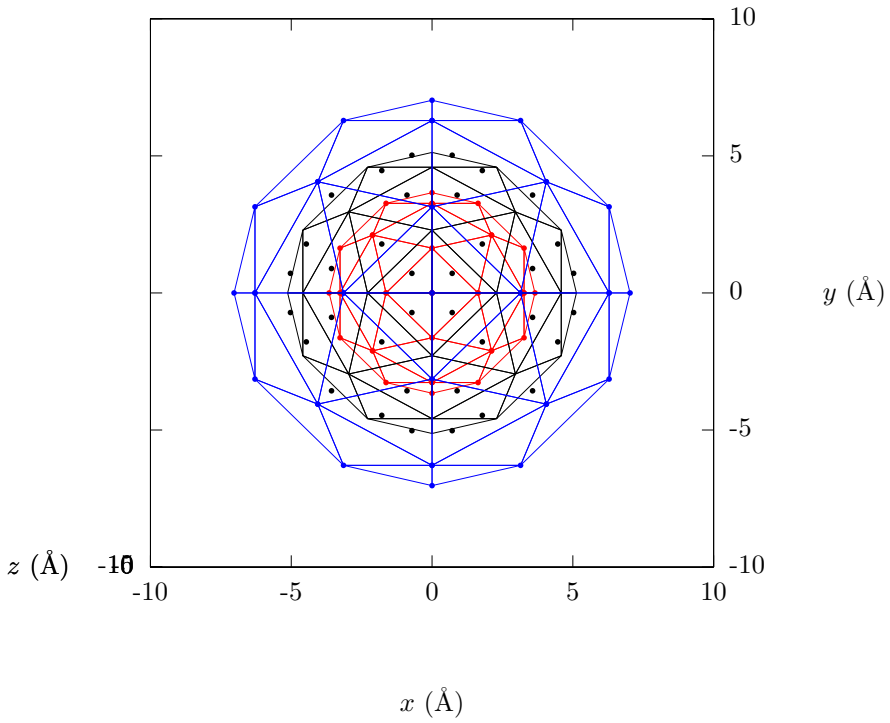

Figure 3.4: Initial atomic positions for *reduced* spherical TeMoS for ionic and electronic relaxations. The inner, middle and outer spheres comprise S (red), Mo (black) and Te (blue) atoms respectively.

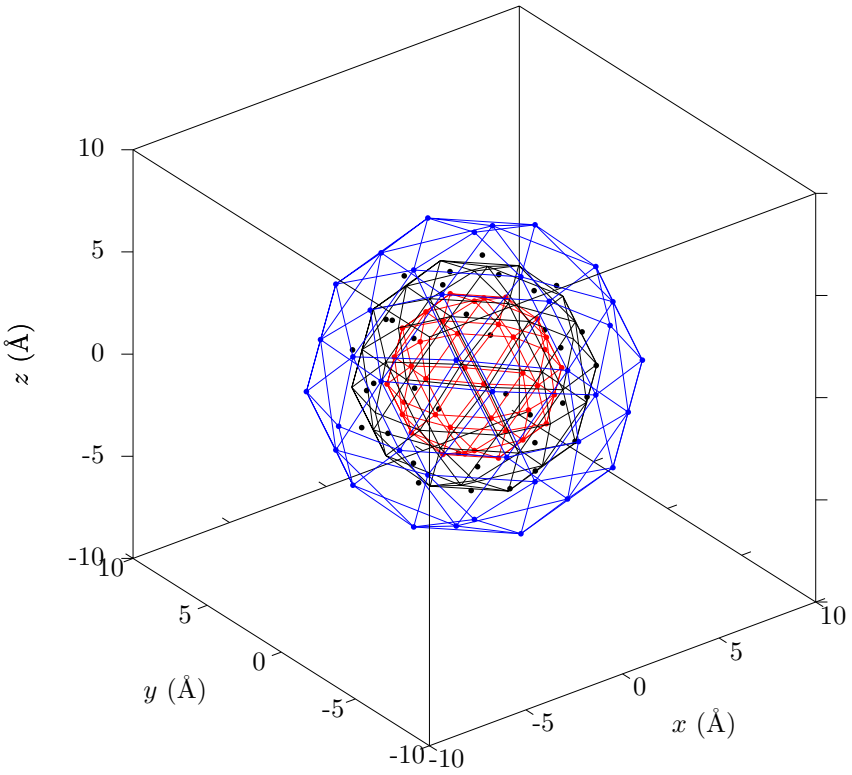

Figure 3.5: Different view of initial atomic positions for *reduced* spherical TeMoS.

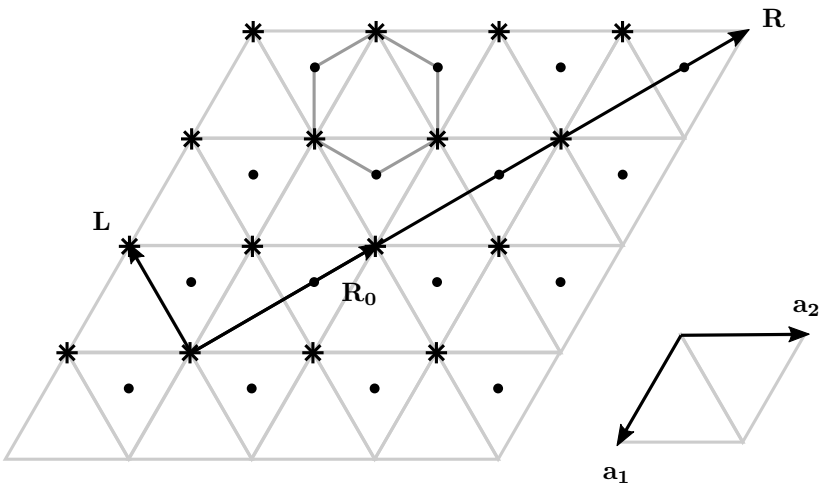

Figure 3.6: Rolling **R** and longitudinal **L** vectors for armchair aTMDs. The plus and cross represent the smaller and bigger chalcogen ions respectively, while the dot represents the middle metal ion. The rolling vector with the smallest possible length is $\mathbf{R_0}$. The rectangular strip whose area bounded by **R** and **L** is rolled up to form the primitive unit cell of the nanotube.

3.3 Nanotube aTMDs

It is difficult to study spherical aTMDs due to the expensive computational cost involved with a large number of atoms. However, we still want to at least verify directly that aTMDs will naturally curl up because of different M-X and M-Y bonds. Fortunately, we can still take advantage of the asymmetry in aTMDs by constructing nanotubes. Due to translational symmetry along the tube's axis, the number of atoms in a unit cell reduces significantly, making DFT computation much more manageable than that for spherical aTMDs.

To construct a nanotube from flat aTMDs, we need two vectors – longitudinal **L** and rolling **R** vectors. These vectors are shown in figure 3.6. **L** is the tube's axis and the primitive lattice vector for the nanotube's 1D lattice. **R** is the vector along which the flat piece is to be rolled, with

$$|\mathbf{R}| = R = 2\pi r_1, \tag{3.16}$$

where r_1 is the radius of the inner tube, similar to the radius of the inner sphere for spherical aTMDs. The way the nanotube is rolled up, or its chirality, is defined by **R** entirely in terms of

$$\mathbf{R} = n_1\mathbf{a_1} + n_2\mathbf{a_2}. \tag{3.17}$$

Such a nanotube is also called a (n_1, n_2) nanotube. The rolling vector with the smallest possible length is $\mathbf{R_0}$ and we can write

$$\mathbf{R} = f\mathbf{R_0}, \tag{3.18}$$

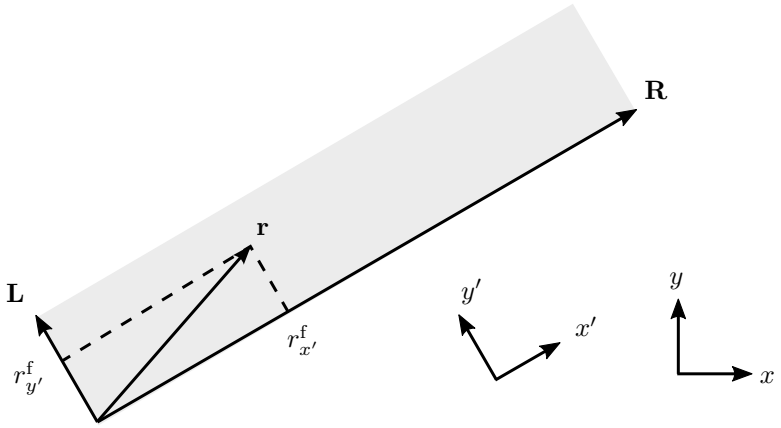

Figure 3.7: Using coordinates x' and y', which are parallel to $\mathbf{R}$ and $\mathbf{L}$ respectively, instead of x and y coordinates for rolling up grey rectangular strip to nanotube. The 'f' in the projections $r^{\mathrm{f}}_{x'}$ and $r^{\mathrm{f}}_{y'}$ means 'flat'.

where f is the frequency analogous to the one used for spherical aTMDs. For example, we have $f = 3$ for figure 3.6.

To roll up the strip whose area is bounded by $\mathbf{R}$ and $\mathbf{L}$, it is useful to first re-define our coordinate system along $\mathbf{R}$ and $\mathbf{L}$ as shown in figure 3.7. For an ion at position $\mathbf{r}$, we have

$$r^{\mathrm{f}}_{x'} = \mathbf{r} \cdot \hat{\mathbf{R}}, \tag{3.19}$$

$$r^{\mathrm{f}}_{y'} = \mathbf{r} \cdot \hat{\mathbf{L}}, \tag{3.20}$$

$$r^{\mathrm{f}}_{z'} = r^{\mathrm{f}}_{z} = \mathbf{r} \cdot \hat{\mathbf{z}}, \tag{3.21}$$

where the 'f' superscript refers to 'flat'. Using figure 3.8, it is easy to see that

$$\frac{\phi}{2\pi} = \frac{r^{\mathrm{f}}_{x'}}{R}. \tag{3.22}$$

Then we have

$$r^{\mathrm{c}}_{x'} = (r_1 + \delta)\cos\phi, \tag{3.23}$$

$$r^{\mathrm{c}}_{z'} = (r_1 + \delta)\sin\phi, \tag{3.24}$$

$$r^{\mathrm{c}}_{y'} = r^{\mathrm{f}}_{y'}. \tag{3.25}$$

Two common nanotube chiralities are the armchair and zigzag variants. Their rolling and longitudinal vectors for TeMoS, as well as their key parameters, are written in table 3.5. There are more atoms in the 1D primitive unit cell of the zigzag nanotube due to a smaller $\mathbf{R}_0$.

Figures 3.9 and 3.10 plot the initial ionic positions for the armchair nanotube, whereas figures 3.11 and 3.12 plot those for the zigzag variant. These initial ionic positions are left to relax according to algorithm 2 and table 3.6.

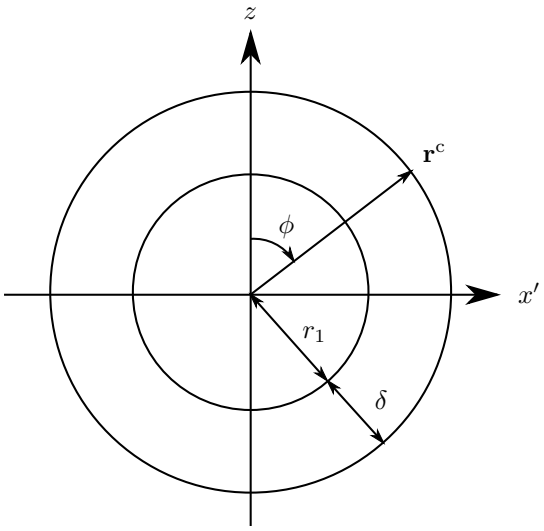

Figure 3.8: Mapping position $\mathbf{r}^{\mathrm{f}}$ from flat rectangular strip in figure 3.7 to position $\mathbf{r}^{\mathrm{c}}$ onto the curved surface of the nanotube. The tube's axis lies along the y' axis, which points into the page. The smaller circle has a circumference R from the rolling vector and has a radius of the inner radius r_1. δ is the height of the position $\mathbf{r}^{\mathrm{f}}$ above the x'-y' plane in the flat strip picture. For aTMDs, δ can be c from (3.12) or d from (3.7).

Table 3.5: Key parameters of initial ionic positions for optimal nanotube TeMoS. $\mathbf{L}$ and $\mathbf{R_0}$ are the longitudinal and smallest rolling vectors respectively, r_1 is the inner radius, f is the number of $\mathbf{R_0}$s contained in $\mathbf{R}$, and N_0, N_1 and N_2 are the number of ions in the middle, inner and outer tubes in the nanotube's primitive unit cell, which is defined by $\mathbf{L}$, respectively.

	Armchair	Zigzag
$\mathbf{L}$	$-\mathbf{a}_1 - \mathbf{a}_2$	$-2\mathbf{a}_1 - \mathbf{a}_2$
$\mathbf{R}_0$	$-\mathbf{a}_1 + \mathbf{a}_2$	$\mathbf{a}_2$
r_1	29.68 Å	30.53 Å
f	32	57
$N_0 = N_1 = N_2$	64	114

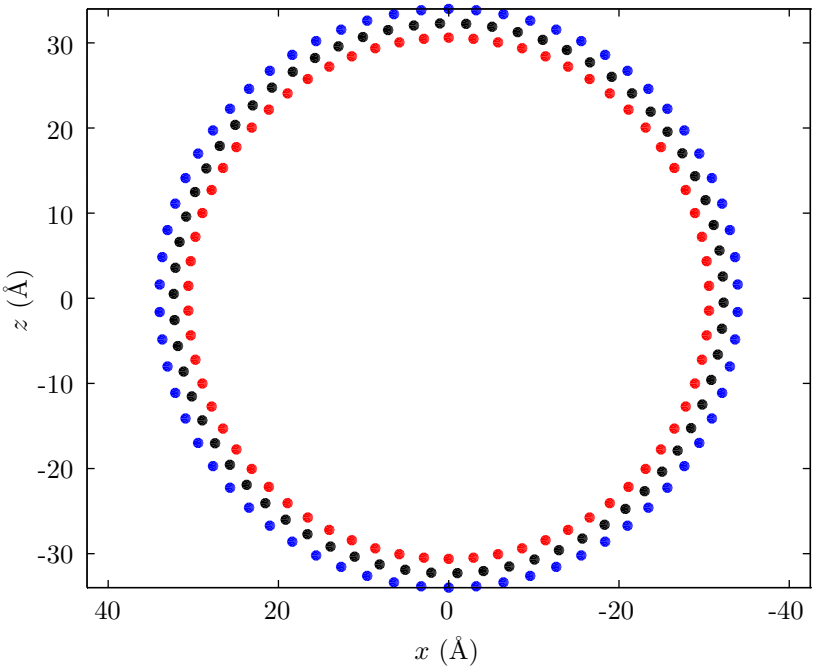

Figure 3.9: Initial atomic positions (front view) in primitive cell of *armchair* nanotube TeMoS for ionic and electronic relaxations. The inner, middle and outer spheres comprise S (red), Mo (black) and Te (blue) atoms respectively.

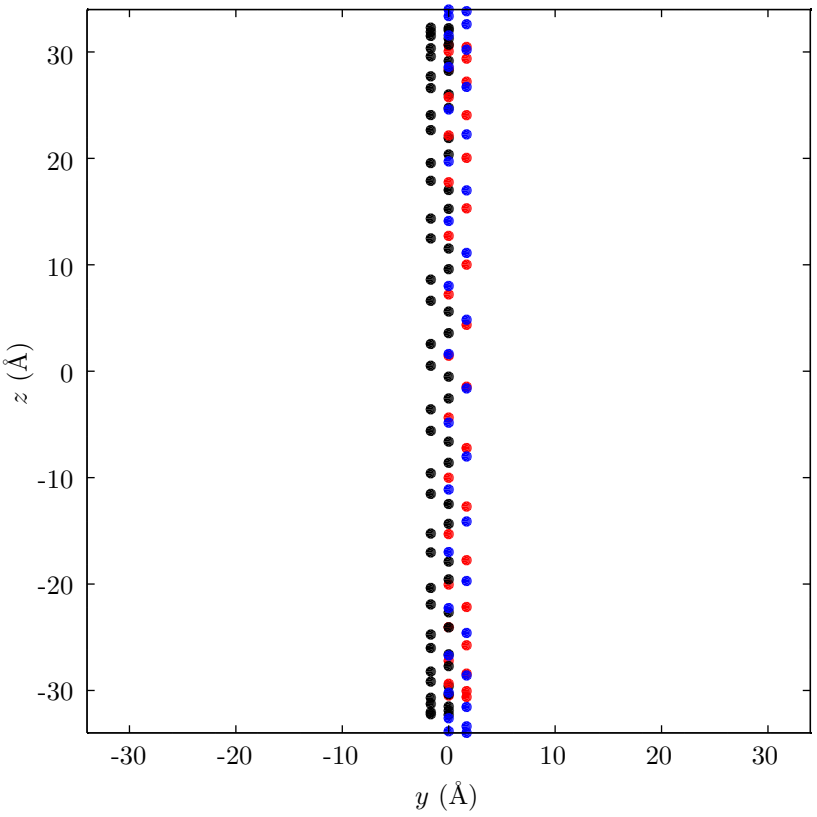

Figure 3.10: Initial atomic positions (side view) in primitive cell of *armchair* nanotube TeMoS for ionic and electronic relaxations.

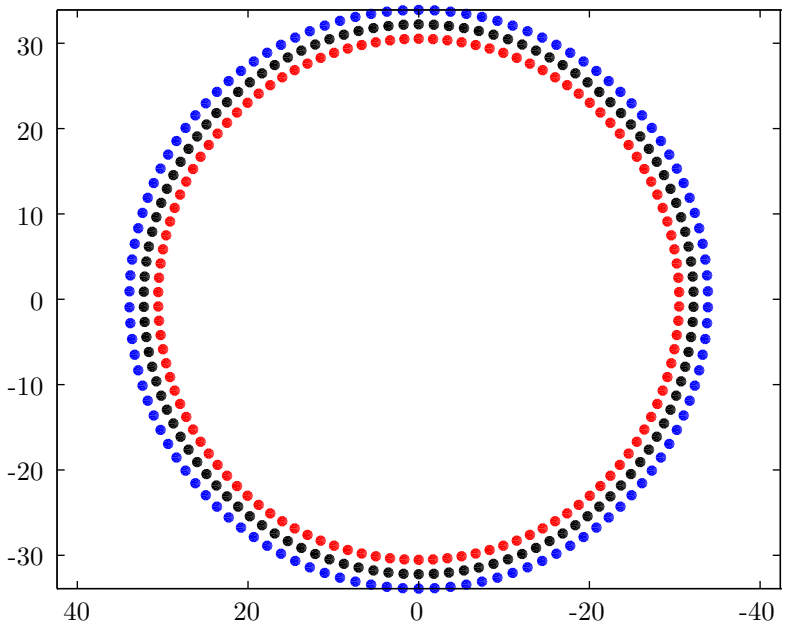

Figure 3.11: Initial atomic positions (front view) in primitive cell of *zigzag* nanotube TeMoS for ionic and electronic relaxations. The inner, middle and outer spheres comprise S (red), Mo (black) and Te (blue) atoms respectively.

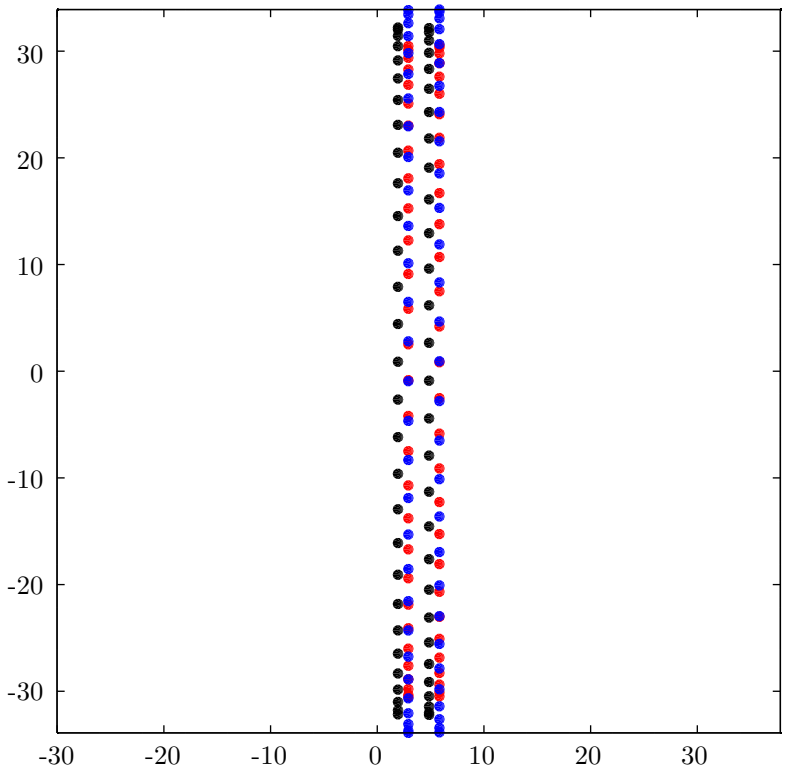

Figure 3.12: Initial atomic positions (side view) in primitive cell of *zigzag* nanotube TeMoS for ionic and electronic relaxations.

Table 3.6: DFT parameters for TeMoS nanotubes, where R is the estimated radius of the nanotube; 15 Å is the distance between two cylindrical surfaces; E_{cut} is the cut-off energy; 3.365 Å is lattice constant for flat TeMoS found later in table 4.1; `EDIFF` and `EDIFFG` are the break conditions for self-consistent electronic and ionic relaxation loops respectively.

Pseudo-potential	Projector-augmented wave method [3]
Exchange-correlation functional	Perdew-Burke-Ernzerhof [21]
E_{cut}	$400\,\text{eV}$
Super-cell dimensions	$(2r_0 + 15\,\text{Å}) \times 3.365\,\text{Å} \times (2r_0 + 15\,\text{Å})$
Ionic relaxation method	Conjugate gradient descent
`EDIFF`	$1 \times 10^{-5}\,\text{eV}$
`EDIFFG`	$1 \times 10^{-4}\,\text{eV}$
k-points mesh	Γ-centered Monkhorst-Pack $1 \times 7 \times 1$

Chapter 4

Results and discussion

4.1 Flat TMDs and aTMDs

4.1.1 Equilibrium lattice parameters

The energy F per super-cell defined by vectors $\mathbf{a}_1$, $\mathbf{a}_2$ and $\mathbf{a}_3$ vs. lattice parameter $a = |\mathbf{a_1}| = |\mathbf{a_2}|$ plots are shown in figures 4.1 and 4.2 for MoS_2. The plots for the rest of the TMDs and aTMDs are drawn in the appendix: A.1 and A.2 for SeMoS, A.3 and A.4 for $MoSe_2$, A.7 and A.8 for SeMoTe, and A.9 and A.10 for $MoTe_2$. The first plot for each material is a rough plot with large increments of a by 0.1 Å to estimate the region near the equilibrium lattice parameter. The second plot zooms in to this region and increments a by a finer 0.01 Å. Near the equilibrium lattice parameter a_0, we have

$$F(a - a_0) = F(a_0) + F'(a_0)(a - a_0) + \frac{1}{2}F''(a_0)(a - a_0)^2 + \dots . \tag{4.1}$$

At the minimum point, $F'(a_0)$ vanishes, leaving only the quadratic term if we ignore the negligibly small higher terms. We thus fit a quadratic curve in the fine plots for each material to obtain the equilibrium lattice parameters a_0, which are tabulated in table 4.1.

The equilibrium lattice parameters from our fits agree well with the experimental values with $< 1\%$ error. The equilibrium lattice parameter increases from MoS_2 to $MoSe_2$ to $MoTe_2$, which is to be expected since the atomic radii of the chalcogens increase down the group from S (1.00 Å) to Se (1.15 Å) to Te (1.40 Å) [24]. Also, SeMoS having a radius between that of MoS_2 and $MoSe_2$ (similarly for SeMoTe) is intuitive.

4.1.2 Average Cohesive Energies per Atom

Using the single atom energies in table 4.2 and (3.1), we determine the average cohesive energies per atom in table 4.3.

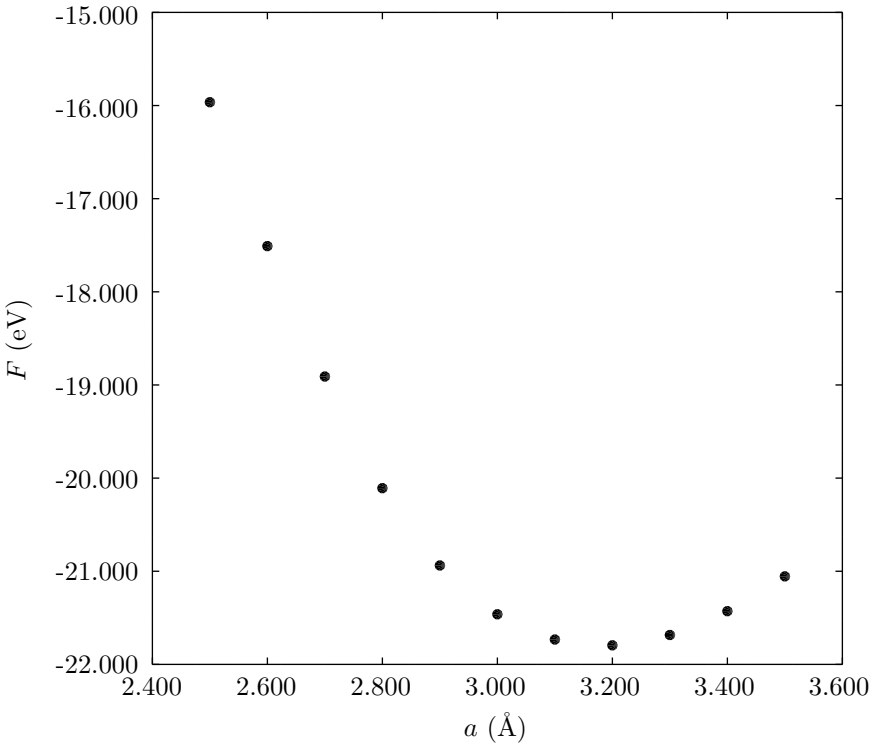

Figure 4.1: Rough plot of total energy F per super-cell defined by vectors $\mathbf{a}_1$, $\mathbf{a}_2$ and $\mathbf{a}_3$ vs. lattice parameter $a = |\mathbf{a_1}| = |\mathbf{a_2}|$ for MoS_2. For each fixed value of a, the positions of the ions are allowed to relax until convergence.

Table 4.1: Fitted equilibrium lattice parameters a_0 arranged in ascending order for various flat (a)TMDs. Blank cells mean no experimental values for a_0 are available.

Material	a_0 (Å)	Experimental value (Å)	Error (%)
MoS_2	3.185	3.1602 [27]	0.7721
SeMoS	3.249		
$MoSe_2$	3.319	3.289(1) [4]	0.9243
TeMoS	3.365		
SeMoTe	3.435		
$MoTe_2$	3.552	3.519(1) [22]	0.9321

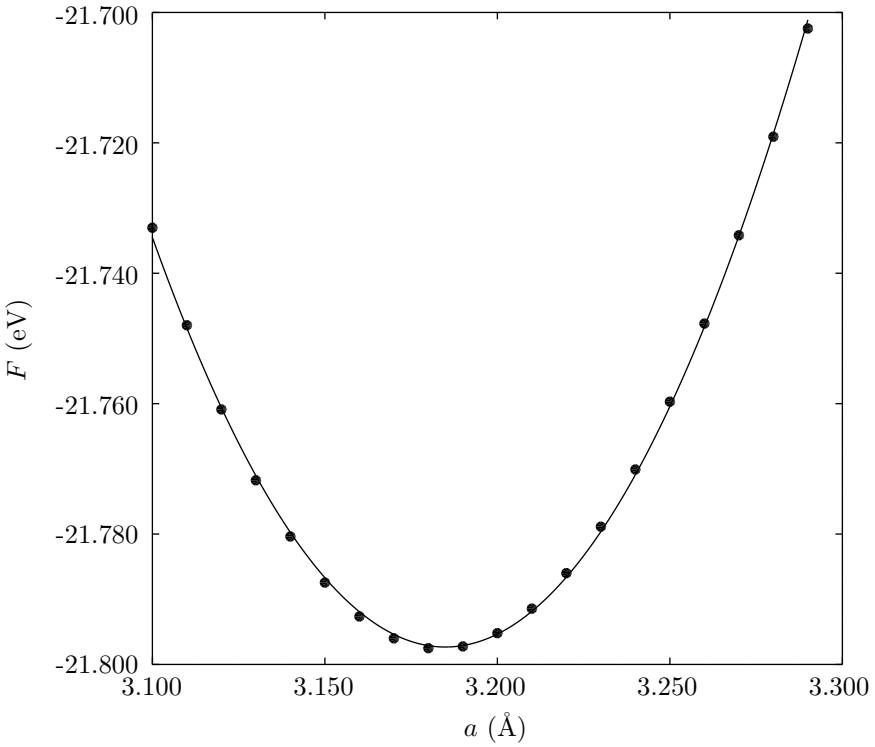

Figure 4.2: Fine plot of total energy F per super-cell vs. lattice parameter $a = |\mathbf{a_1}| = |\mathbf{a_2}|$ for MoS_2.

Table 4.2: Total energies F_α for single atom α.

α	F_α (eV)
Mo	-0.723
S	-0.324
Se	-0.322
Te	-0.319

Table 4.3: Average cohesive energies per atom E_c determined from total energies for entire primitive cell F for various flat (a)TMDs.

Material	F (eV)	E_c (eV)
MoS_2	-21.783	-6.80
SeMoS	-20.832	-6.49
$MoSe_2$	-19.937	-6.19
TeMoS	-19.705	-6.11
SeMoTe	-18.904	-5.85
$MoTe_2$	-18.024	-5.55

Table 4.4: Bader analysis for SeMoS

Atom	Charge (e)	Assigned volume (Å^3)
Se	6.6797	59.7143
Mo	4.4640	12.0419
S	6.8563	59.7091

4.1.3 Equilibrium Lattice Parameters vs. Average Cohesive Energies per Atom

Figure 4.3 plots the average cohesive energies E_c per atom vs. equilibrium lattice parameter a_0 relationship using tables 4.1 and 4.3.

4.1.4 Charge Distributions of Asymmetric Transition Metal Dichalcogenides

Figures 4.4, 4.5 and 4.6 show the charge densities for aTMDs SeMoS, SeMoTe and TeMoS respectively. As expected, TeMoS shows the greatest difference in charge densities between the two chalcogens.

4.1.5 Bader Analysis

Bader analysis divides the electron charge density and unit cell volume, and assigns them to the constituent atoms. The results are tabulated from tables 4.4 to 4.6. As expected, the charge densities assigned to the more electronegative atoms are larger. TeMoS shows the greatest difference in assigned charge between the two chalcogens, in agreement with the charge density plots.

4.1.6 Dipole moment

The asymmetry in charge density in a aTMD will result in a dipole moment. Figure 4.7 shows the sum of charge density $n(z)$ in x-y plane of the primitive cell for TeMoS, and figures A.11 to A.15 show $n(z)$ for other flat (a)TMDs. Table 4.7 show the dipole moment magnitudes calculated using (3.3). Surprisingly,

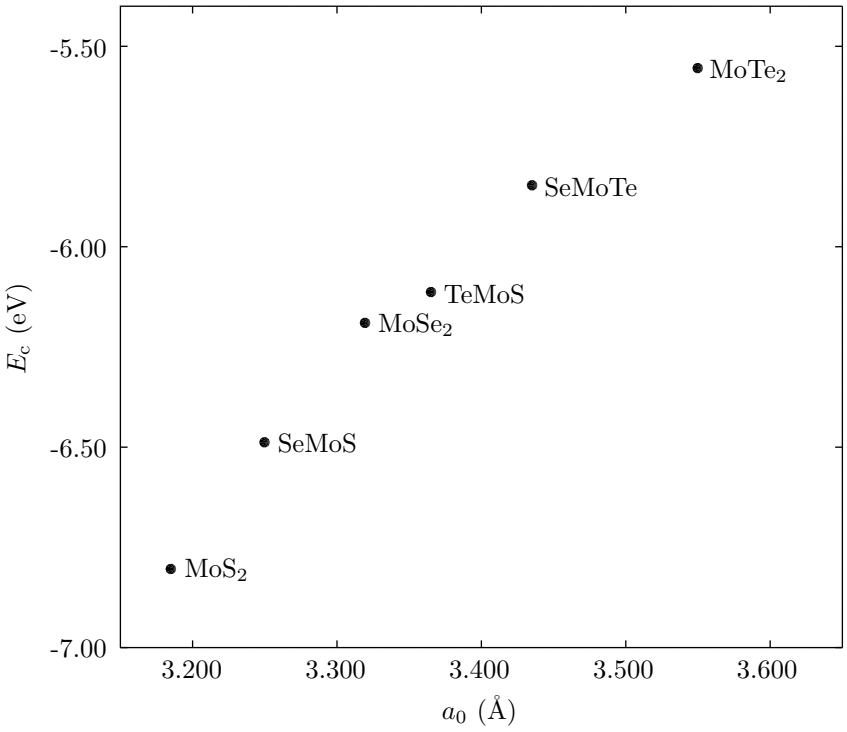

Figure 4.3: Plot of fitted equilibrium lattice parameters a_0 and average cohesive energy E_c for each material. As the size of the constituent chalcogens increase, both a_0 and E_c increase.

Table 4.5: Bader analysis for SeMoTe

Atom	Charge (e)	Assigned volume (Å^3)
Se	6.6943	64.6254
Mo	4.8839	14.1299
Te	6.4217	71.6697

Table 4.6: Bader analysis for TeMoS

Atom	Charge (e)	Assigned volume (Å^3)
Te	6.4071	64.7791
Mo	4.7111	13.3969
S	6.8818	63.2514

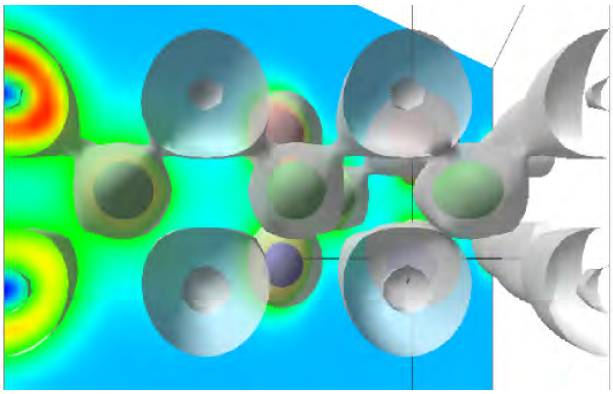

Figure 4.4: Equilibrium charge density for SeMoS. Bottom atoms are Se atoms, middle atoms are Mo atoms, and top atoms are S atoms. The grey surface is an isosurface, whereas reddish (bluish) colours on the slice indicate greater (less) charge density.

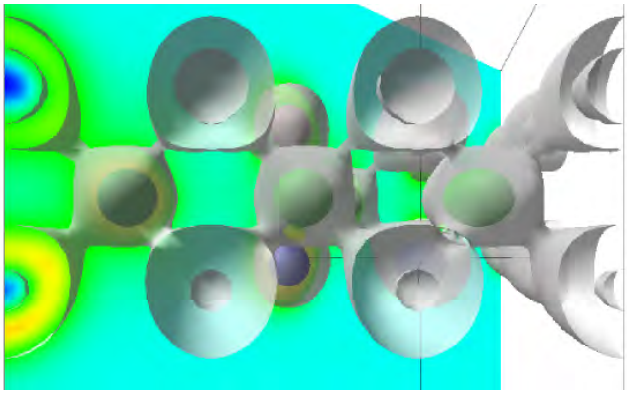

Figure 4.5: Equilibrium charge density for SeMoTe. Bottom atoms are Se atoms, middle atoms are Mo atoms, and top atoms are Te atoms.

Table 4.7: Dipole moment magnitudes for various (a)TMDs. All dipole moments point from the more electronegative to less electronegative chalcogen.

Material	d (e Å)
SeMoS	1.12
SeMoTe	1.09
TeMoS	2.43

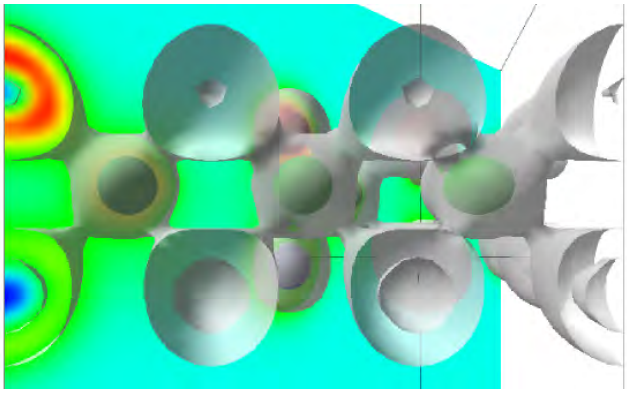

Figure 4.6: Equilibrium charge density for TeMoS. Bottom atoms are Te atoms, middle atoms are Mo atoms, and top atoms are S atoms.

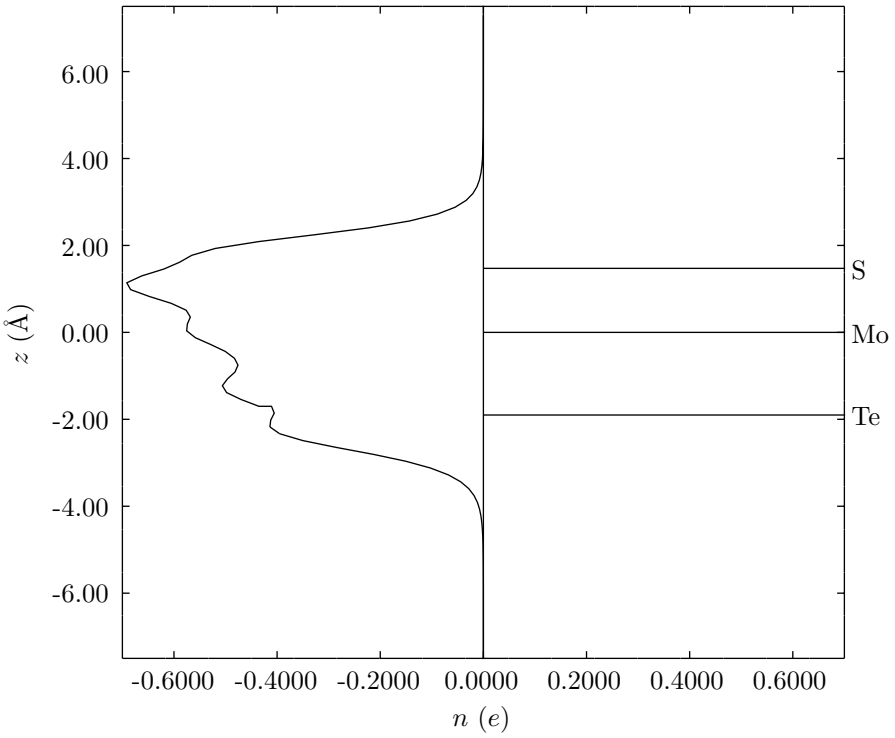

Figure 4.7: Charge density $n(z)$ for TeMoS. Negative $n(z)$ is the electron charge density, whereas the positive delta functions are the ionic charge density.

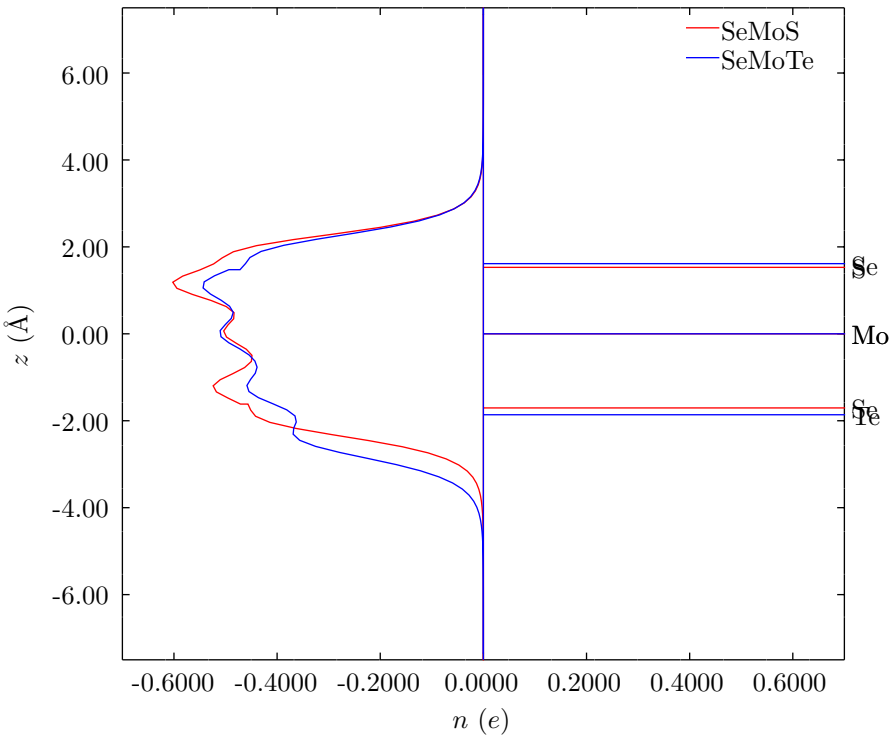

Figure 4.8: Charge density $n(z)$ for SeMoS and SeMoTe. The order of ions in increasing z is Se, Mo, S for SeMoS, and Te, Mo, Se for SeMoTe.

the dipole moment for SeMoTe is less than that of SeMoS, even though the electronegativity difference is larger in SeMoTe than that of SeMoS. Figure 4.8 shows the charge density $n(z)$ for SeMoS and SeMoTe.

The dipole moment of $2.43\,e\,\text{Å} = 11.6\,\text{D}$ for each primitive unit cell of TeMoS (contains 1 Te, 1 Mo and 1 S ion) is significant. A water molecule has only a dipole moment of $1.85\,\text{D} = 0.385\,e\,\text{Å}$ [11]. However, the aTMD monolayer resembles a layer of lipids more than a single water molecule. According to Mohwald [19], the dipole moment for typical phospholipids are estimated be around 15 D but are measured to be less than 1 D due to the screening effect of mobile ions in the solution. 15 D is of the same order of magnitude for TeMoS.

The electron rich side of aTMD monolayers, e.g. S side for TeMoS, may be used for catalysis. In gold catalysis, the gold atom absorbs negative charge and uses this extra negative charge to cleave bonds [10]. Similarly, the electron rich S side for TeMoS may also be used to cleave bonds to lower the activation energy of a reaction, thus speeding up the reaction.

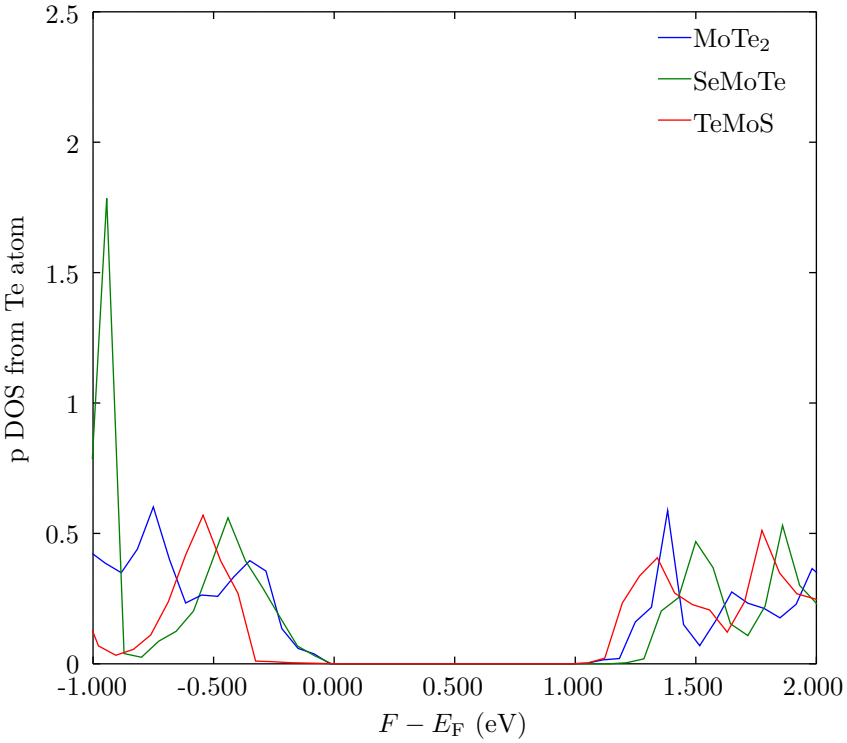

Figure 4.9: Receding p DOS of Te atom from Fermi energy E_F when asymmetry in TMD increases from $MoTe_2$ to SeMoTe to TeMoS.

4.1.7 Density of states

Figures A.16 to A.21 show the density of states (DOS) for various (a)TMDs. In general, the sum of all the atom and orbital decomposed DOS's is not the total DOS. This is because the interstitial regions are not projected onto the spherical harmonics of the atoms. From these figures, we see that the valence and conduction states are contributed by hybridisation of Mo's d shell and the chalcogens' p shell. The contributions from the p shells of the chalcogens are small compared to that from the d shells of Mo.

Looking closely at the Te atom in DOS plots for $MoTe_2$, SeMoTe and TeMoS, we find that the p DOS recedes from below the Fermi energy when the asymmetry in the (a)TMD increases. Figure 4.9 zooms in to the Fermi energy and plots the Te p DOS for these three (a)TMDs.

Table 4.8: Band gaps for flat (a)TMDs and high symmetry k-points $\mathbf{k}_\mathrm{v}$ and $\mathbf{k}_\mathrm{c}$ at which valence and conduction edges are found.

Material	Type	Band gap (eV)	$\mathbf{k}_\mathrm{v} \to \mathbf{k}_\mathrm{c}$
MoS_2	Direct	1.667	K $\to$ K
SeMoS	Direct	1.560	K $\to$ K
$MoSe_2$	Direct	1.437	K $\to$ K
SeMoTe	Direct	1.266	K $\to$ K
$MoTe_2$	Direct	1.074	K $\to$ K
TeMoS	Indirect	1.046	$\Gamma \to$ K

4.1.8 Band structure

Figures A.22 to A.33 show the band structures for various flat TMDs and aTMDs. The crosses represent the highest point of the valence band and lowest point of the conduction band, i.e. the valence and conduction edges. The types and values of the band gaps are tabulated in table 4.8. As expected, the direct band gaps increase with increasing electronegativity. Increasing electronegativity from the ion makes it more difficult to excite electrons, which implies a larger energy gap. All (a)TMDs, except TeMoS, have direct band gaps.

Focusing on the valence and conduction bands for $MoTe_2$, SeMoTe and TeMoS (in order of increasing asymmetry) in figure 4.10, we see that the change from a direct K $\to$ K band gap to an indirect $\Gamma \to$ K band gap is due to a relative increase in valence energy $E_\mathrm{v}(\Gamma)$ at the Γ point (or relative decrease in valence energy E_v(K) at the K point). This relative decrease in E_v(K) corresponds to the receding p DOS of the Te ion from the Fermi energy in figure 4.9. From the atom and orbital decomposed DOS plots in figure A.21, we see that the Fermi energy E_F is held up by the pd hybridised DOS from the S and Mo ions. This suggests that E_v(K) is contributed by the Te ion, whereas $E_\mathrm{v}(\Gamma)$ is contributed by the Mo and S ions. For completeness, we also plot the valence and conduction bands with increasing asymmetry from MoS_2 to SeMoS to TeMoS in figure 4.11.

Figures 4.12 and 4.13 show the ion-decomposed band structure for TeMoS, with the colour of every point defined by

$$(r, g, b) = \frac{(c_\mathrm{Te}, c_\mathrm{Mo}, c_\mathrm{S})}{c_\mathrm{Te} + c_\mathrm{Mo} + c_\mathrm{S}}, \tag{4.2}$$

where r, g, b stand for the intensities of red, green, blue respectively; and c_Te is the contribution from the Te ion and likewise for c_Mo and c_S. $(0, 0, 0)$ is black and $(1, 1, 1)$ is white. We see that the conduction and valence bands are supplied mostly by the Mo atom, consistent with the DOS plots in A.21.

The small contributions from the chalcogens are isolated, renormalised without the Mo's contribution

$$(r, g, b) = \frac{(c_\mathrm{Te}, 0, c_\mathrm{S})}{c_\mathrm{Te} + c_\mathrm{S}}, \tag{4.3}$$

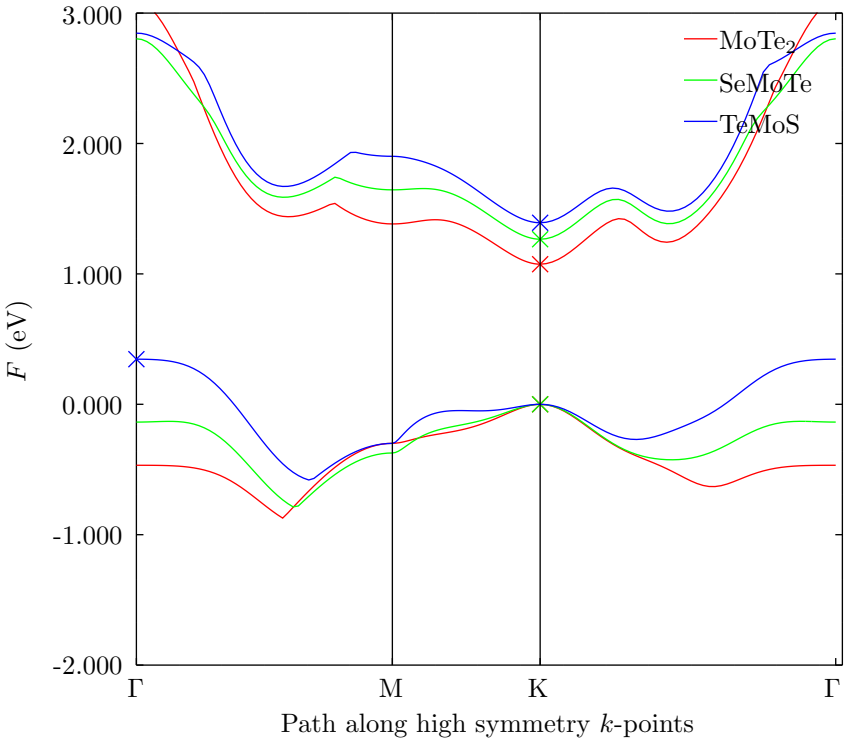

Figure 4.10: Valence and conduction bands with increasing asymmetry from $MoTe_2$ to SeMoTe to TeMoS. The change from a direct K $\rightarrow$ K band gap to an indirect $\Gamma \rightarrow$ K band gap is due to a relative increase in valence energy at the Γ point (or relative decrease in valence energy at the K point). The energy gap at the K point also increases with increasing electronegativity of one of the chalcogens, which is expected because more energy is needed to excite an electron for more tightly-bound systems.

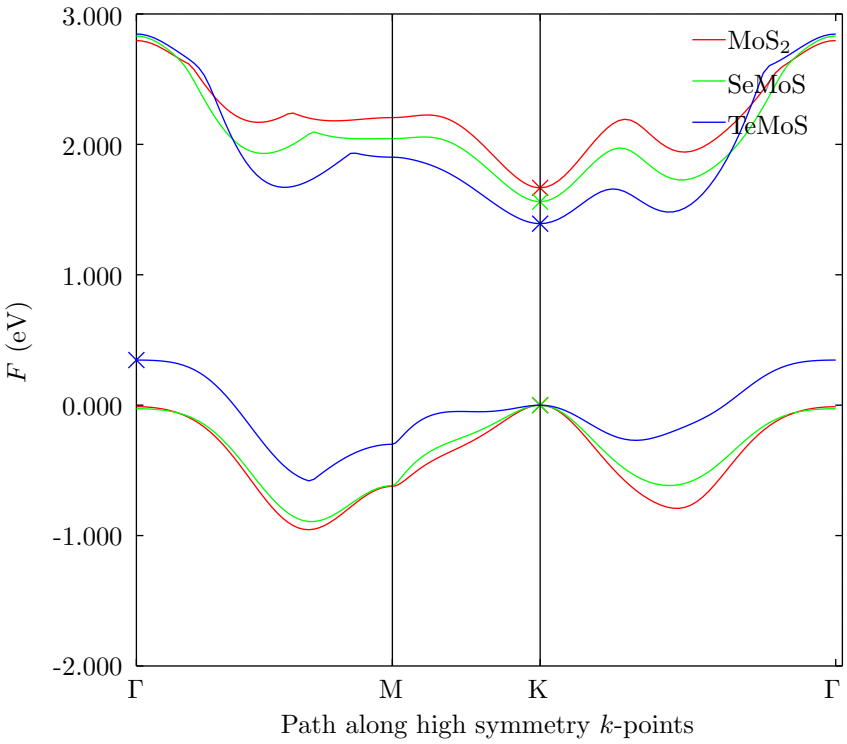

Figure 4.11: Valence and conduction bands with increasing asymmetry from MoS_2 to SeMoS to TeMoS. The change from direct K $\rightarrow$ K band gap to an indirect $\Gamma \rightarrow$ K band gap is due to a relative increase in valence energy at the Γ point (or relative decrease in valence energy at the K point). MoS_2 and SeMoS look similar because the electronegativities of S and Se are very close.

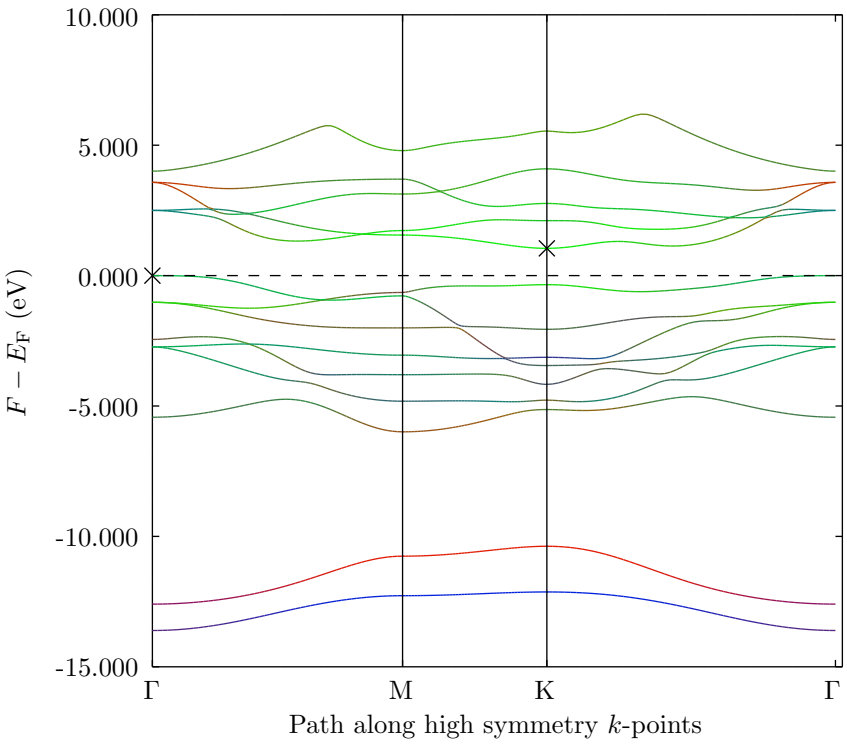

Figure 4.12: Ion-decomposed band structure for TeMoS. The contributions by Te, Mo and S ions are coloured red, green and blue respectively.

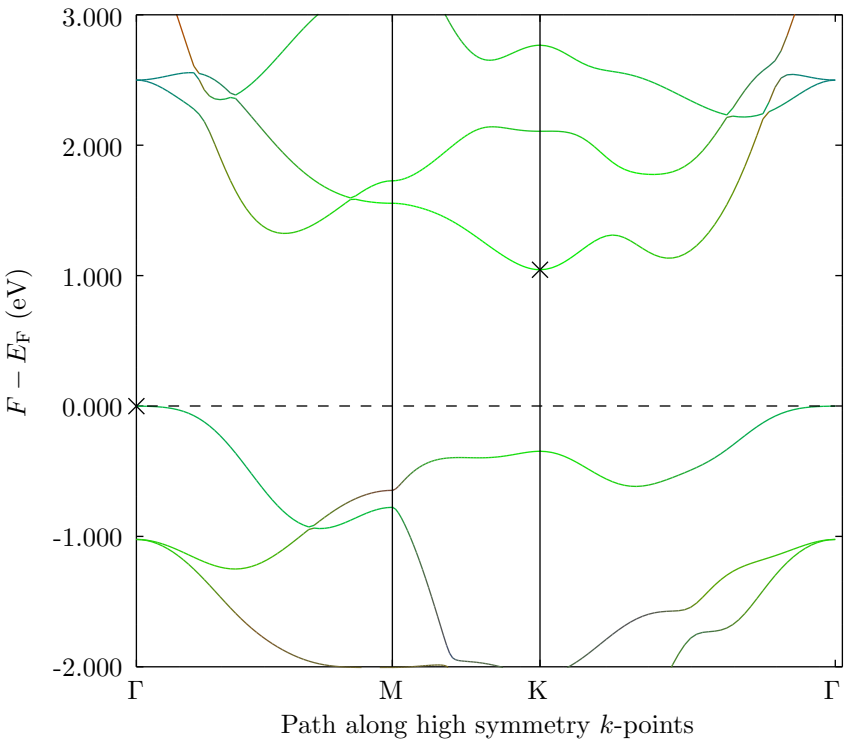

Figure 4.13: Ion-decomposed band structure (zoomed in) for TeMoS. The contributions by Te, Mo and S ions are coloured red, green and blue respectively.

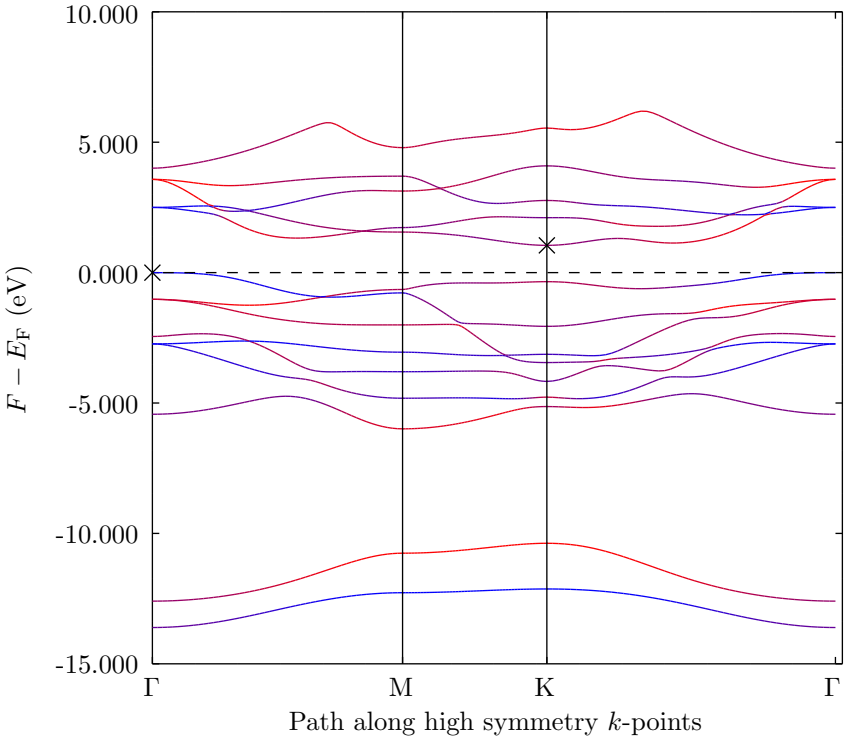

Figure 4.14: Ion-decomposed band structure for TeMoS, *excluding* Mo's contribution and renormalised to the sum of S's and Te's contributions. The contributions by Te and S ions are coloured red and blue respectively. Note that the contributions from Te and S are very small compared to Mo.

and are shown in figures 4.14 and 4.15. We find that the valence edge $E_v(\Gamma)$ is contributed by the S ion, whereas the conduction edge $E_c(\mathrm{K})$, as well as $E_v(\mathrm{K})$ is contributed by the Te ion.

The decomposed band structure of TeMoS helps to further explain figures 4.10 and 4.11. Literature regarding the strain-induced effects on DFT-calculated band structures of MoS_2 [7] and $MoTe_2$ [16] report that $E_v(\Gamma)$ for MoS_2 increases with tensile strain, whereas $E_v(\mathrm{K})$ for $MoTe_2$ decreases with compressive strain. As the asymmetry in figure 4.10 increases from $MoTe_2$ to TeMoS, the equilibrium lattice constant is influenced by the non-Te chalcogen and decreases according to table 4.1. The Te ion thus sees compressive strain and $E_v(\mathrm{K})$ decreases with increasing asymmetry. On the other hand, the S ion from MoS_2 to TeMoS in figure 4.11 sees an increasing equilibrium lattice constant as the other chalcogen atom becomes larger. It thus experiences a tensile strain and $E_v(\Gamma)$

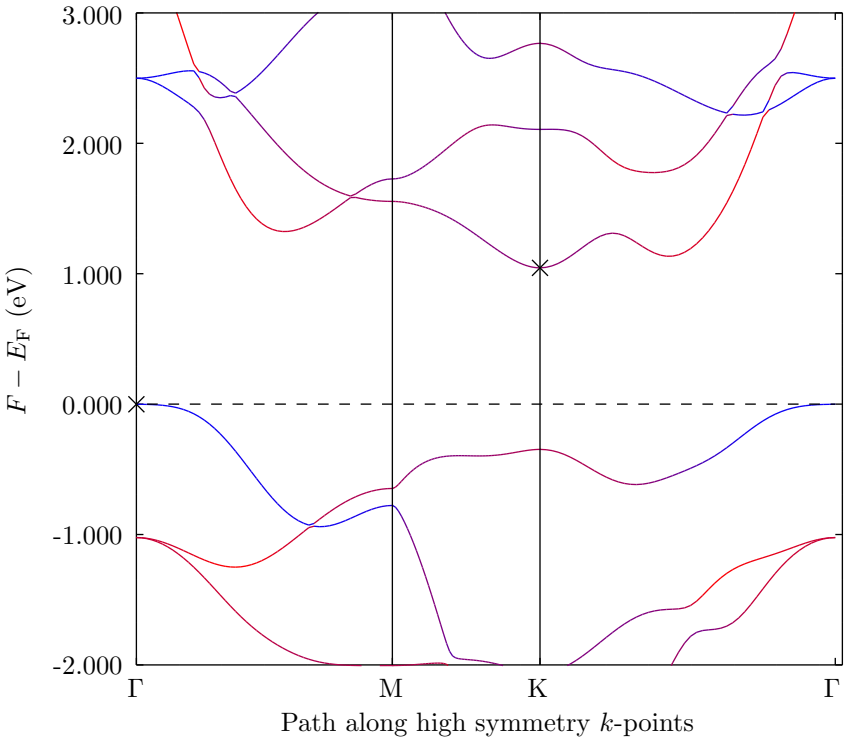

Figure 4.15: Ion-decomposed band structure (zoomed in) for TeMoS, *excluding* Mo's contribution and renormalised to the sum of S's and Te's contributions. The contributions by Te and S ions are coloured red and blue respectively. Note that the contributions from Te and S are very small compared to Mo.

increases. The simultaneous decrease in $E_{\mathrm{v}}(\mathrm{K})$ by the Te ion and increase in $E_{\mathrm{v}}(\Gamma)$ by the S ion causes the switch to an indirect $\Gamma \rightarrow \mathrm{K}$ band gap in TeMoS.

4.1.9 K and Γ Point Charge Densities

Indirect band gaps decrease optical efficiency because additional phonons are needed to impart momentum to the electron for excitation to occur. Despite this, the indirect band gap in TeMoS may still be useful for photonic applications. Because the S ion contributes more to the valence edge $E_{\mathrm{v}}(\Gamma)$ at the Γ point, and the Te ion contributes more to the conduction edge $E_{\mathrm{c}}(\mathrm{K})$ at the K point, the electron can be seen as disappearing from the S ion and appearing at the Te ion after excitation. This separation of holes at the S ion and electrons at the Te ion makes it easier for collection by an external circuit.

Figures 4.16 to 4.19 show the charge density at the valence edge for TeMoS, whereas figures 4.20 and 4.23 show the charge density at the conduction edge. These charge densities are

$$n(\mathbf{r}) = |\phi(r)|^2, \tag{4.4}$$

where $\phi(r)$ is the wavefunction that can contain 2 electrons and gives the valence $E_{\mathrm{v}}(\Gamma)$ or conduction edge $E_{\mathrm{c}}(\mathrm{K})$.

These charge density plots at the valence and conduction edges show the spatial distributions of the hole and electron respectively after electron-hole pair separation. Due to the high charge densities around the Mo atom for both the conduction and valence edges, the spatial separation between electron and hole is much less pronounced. This was also pre-empted by the large Mo contributions to the valence and conduction bands in figure 4.13. Unfortunately, electron-hole pair separation is poor for TeMoS.

4.2 Spherical aTMDs

Figures 4.25 to 4.28 show the equilibrium ionic positions and charge density for reduced spherical TeMoS after full relaxation. As mentioned earlier, this reduced sphere has a radius of 8 times smaller than what we estimate to be optimal; the optimal sphere contains too many atoms and makes DFT treatment infeasibly expensive. We expect this reduced spherical structure to be highly strained.

4.3 Nanotube aTMDs

4.3.1 Equilibrium charge density

Figures 4.29, 4.30 and 4.31 plot the equilibrium charge densities for the $f = 3$, or $(-3, 3)$, armchair TeMoS nanotube. Similarly, figures 4.32, 4.33 and 4.34 plot the equilibrium charge density for the $f = 3$, or $(0, 3)$, zigzag variant. These nanotubes have much smaller radii of curvature than the optimal ones in table 3.5 and are severely strained. We can see from figures 4.30 and 4.33

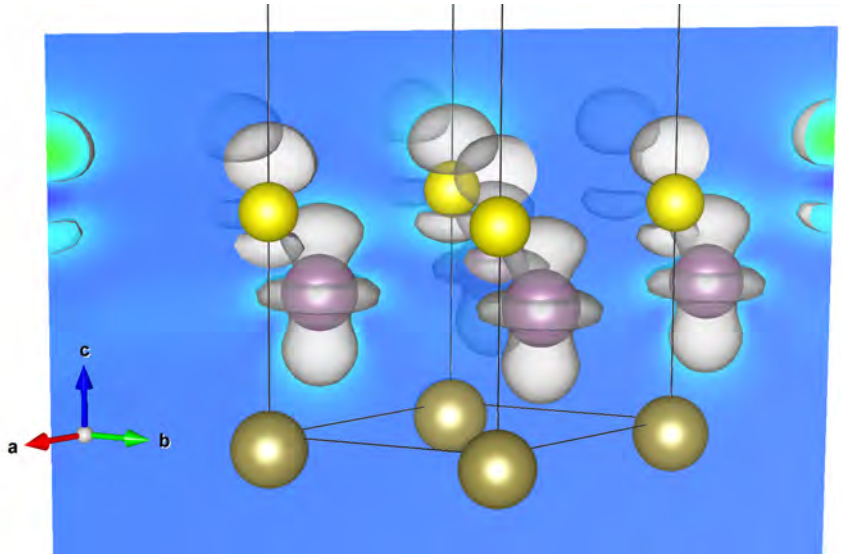

Figure 4.16: Charge density at valence edge with isosurface for TeMoS. The bottom brown spheres are Te ions, the middle purple spheres are Mo ions and the top yellow spheres are S ions. The blue plane slices through the d_z-like electron cloud surrounding the middle Mo ion and the lop-sided p_z-like electron cloud surrounding the top S ion. This charge density reflects the hole density left behind by the electron after it has been excited to the conduction edge at the K point.

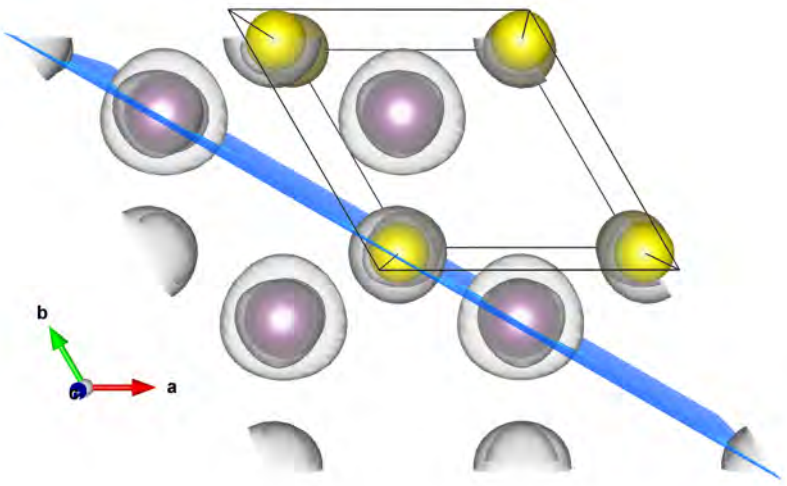

Figure 4.17: Charge density (top view) at valence edge with isosurface for TeMoS.

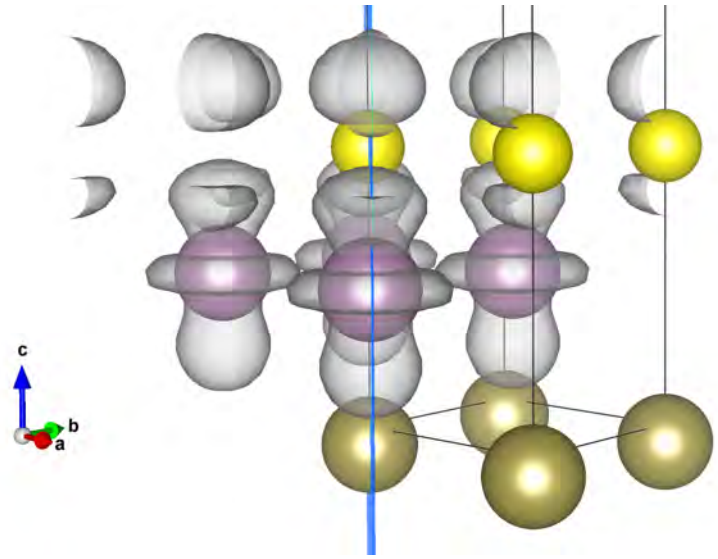

Figure 4.18: Charge density (side view) at valence edge with isosurface for TeMoS.

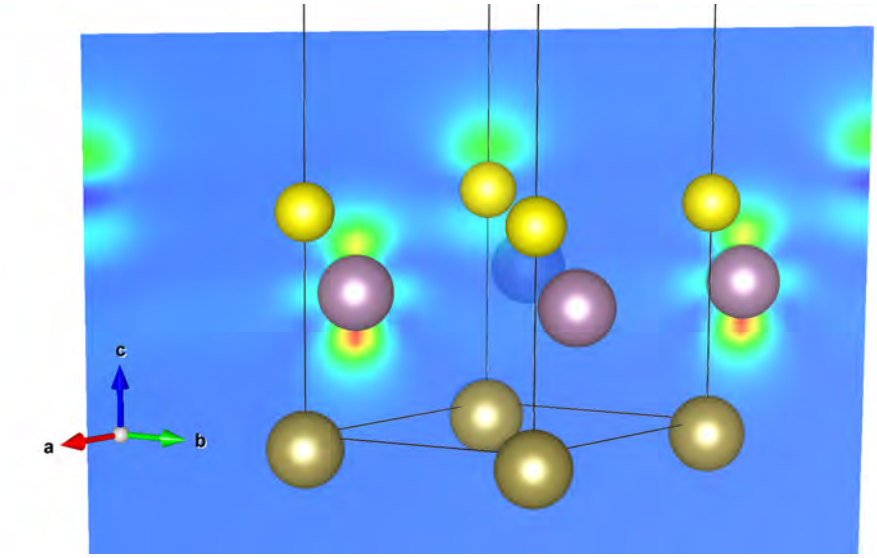

Figure 4.19: Charge density at valence edge shown using slice for TeMoS. Most of the hole charge density is captured by the middle Mo ion, a significant portion is captured by the top S ion, and no hole charge density is captured by the bottom Te ion.

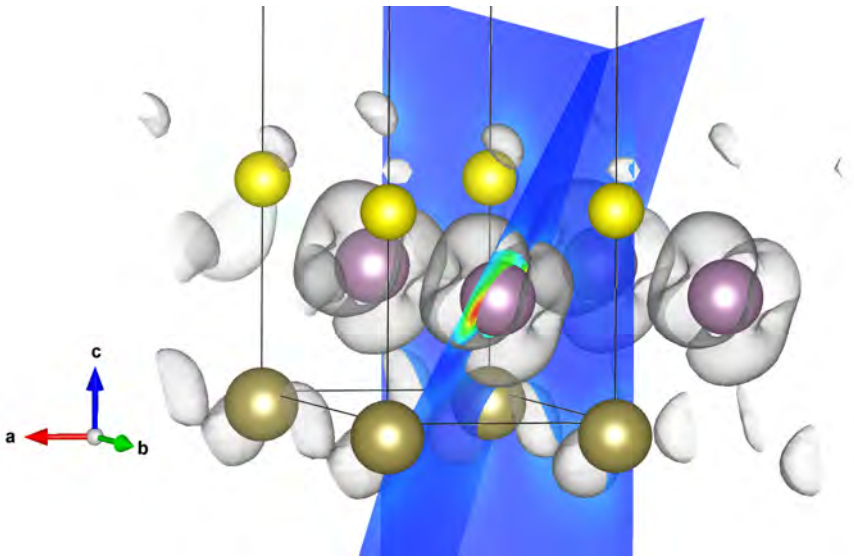

Figure 4.20: Charge density at conduction edge with isosurface for TeMoS. The bottom brown spheres are Te ions, the middle purple spheres are Mo ions and the top yellow spheres are S ions. The blue planes slice through the double-doughnut shaped electron cloud surrounding the middle Mo ion and the butterfly-wing shaped electron cloud surrounding the bottom Te ion. This charge density reflects the conduction electron density after excitation from the Γ point.

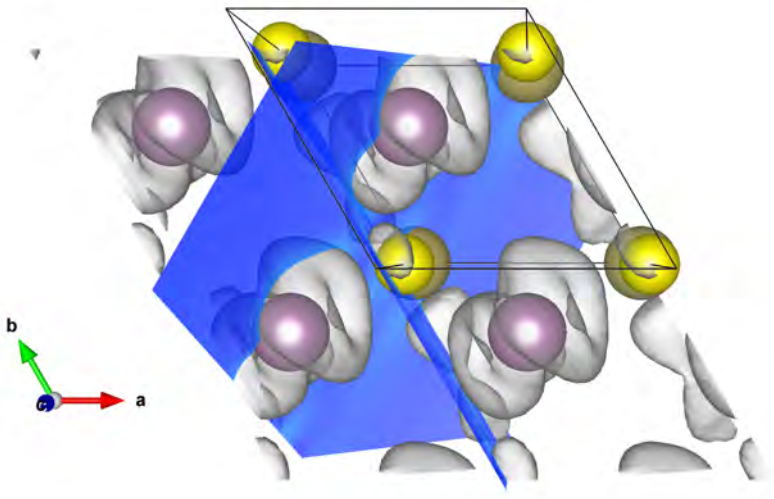

Figure 4.21: Charge density (top view) at conduction edge with isosurface for TeMoS.

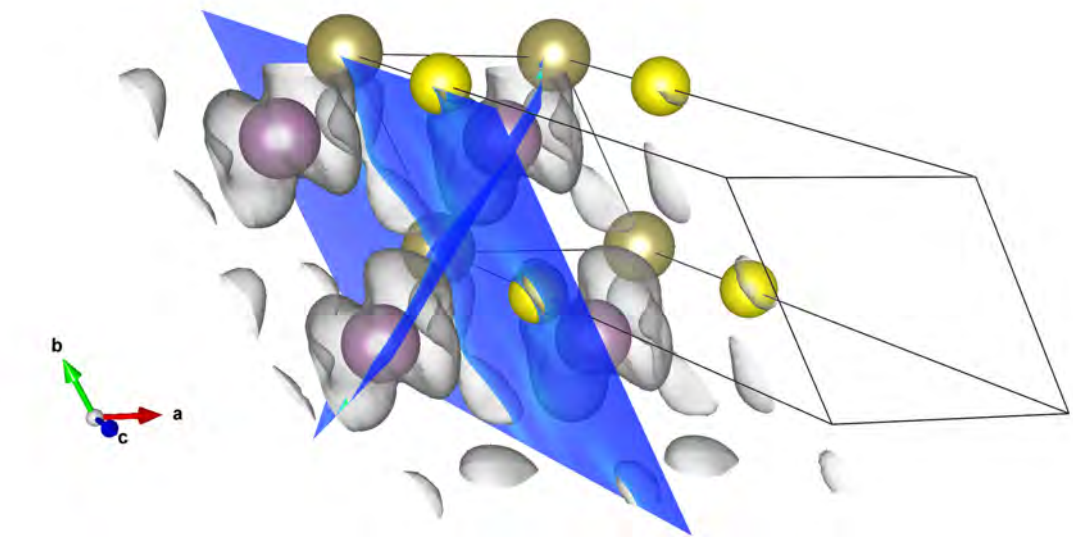

Figure 4.22: Charge density at conduction edge with isosurface for TeMoS.

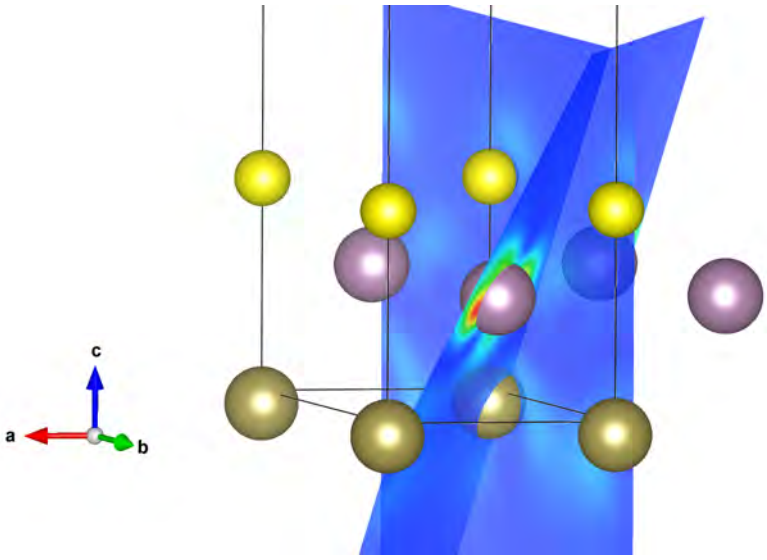

Figure 4.23: Charge density at conduction edge shown using slices for TeMoS. Most of the charge density surrounds the Mo ion, with slightly higher charge density at the bottom Te ion than the top S ion.

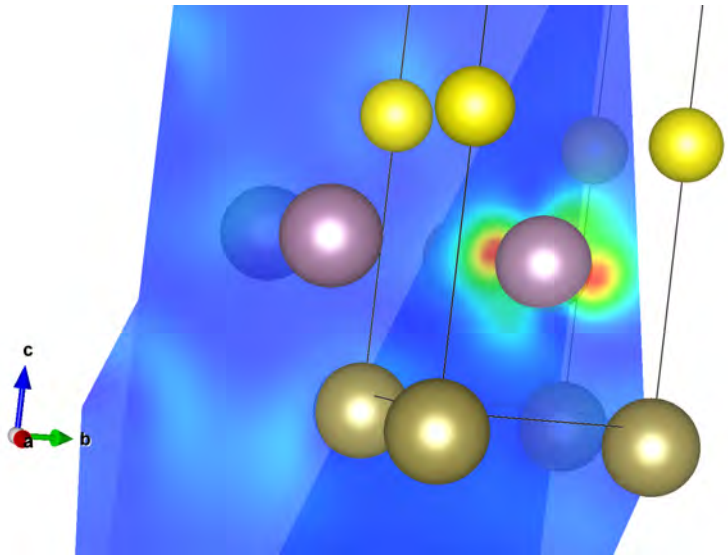

Figure 4.24: Charge density at conduction edge shown using slices for TeMoS.

that the Te atoms appear to protrude out significantly, with the middle Mo and S atoms closer to one another. This is due to the high electron density in the middle of such a small nanotube which repels the Te atoms outwards.

Figures 4.35 and 4.36 show the equilibrium charge density for the *optimal* armchair TeMoS nanotube defined in table 3.5, whose radius is large. However, due to time constraint and more expensive DFT computation (there are more ions in a primitive cell for zigzag nanotubes), the relaxation for the *optimal* zigzag nanotube is not complete and is left to be done as future work.

4.3.2 Energy vs. radius of curvature

For carbon or symmetric TMD nanotubes, we do not expect a minimum in the energy vs. radius of curvature plot [8]. This is because their lowest-energy structure is flat. However, the difference in the M-X and M-Y bonds for aTMDs means that the least-energy structure is curved and that there is an optimal radius of curvature. Thus we expect a minimum in the energy vs. radius of curvature plot for aTMD nanotubes. Figure 4.37 illustrates this point.

Figures 4.38 and 4.39 show the average energy per atom F/N vs. radius of curvature r_0 for the armchair TeMoS nanotube, where F is the total energy per primitive cell and N is the number of atoms in the primitive cell. Since the primitive lattice constant L along the tube's axis is kept fixed for all plotted points, the plotted points do not represent fully relaxed structures. However, the presence of a minima shows that aTMDs indeed curl up. This natural radius of curvature may make aTMDs better candidates for fabricating nanotubes; graphene is naturally flat and experiences significant strain when rolled into

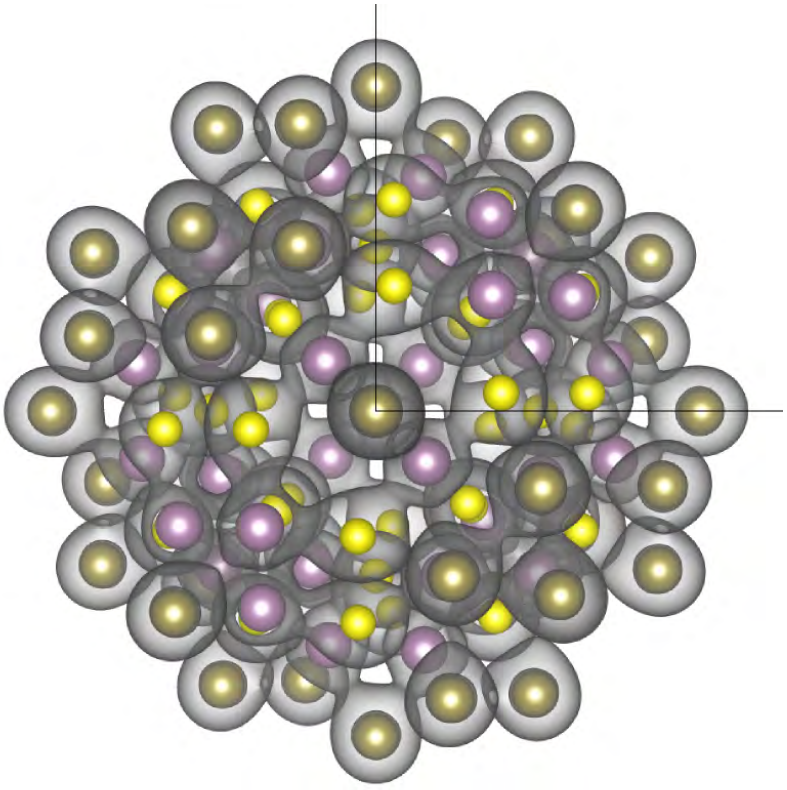

Figure 4.25: Equilibrium ionic positions and charge density for reduced spherical TeMoS after ionic relaxation. The inner, middle and outer spheres comprise S, Mo and Te atoms respectively. Charge density isosurface is shown here.

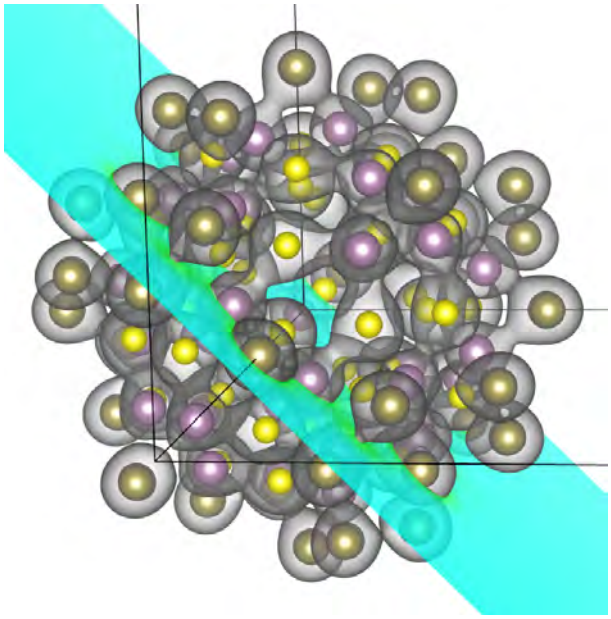

Figure 4.26: Equilibrium ionic positions and charge density for reduced spherical TeMoS after ionic relaxation. The inner, middle and outer spheres comprise S, Mo and Te atoms respectively. Charge density isosurface showing slice position and orientation is drawn here.

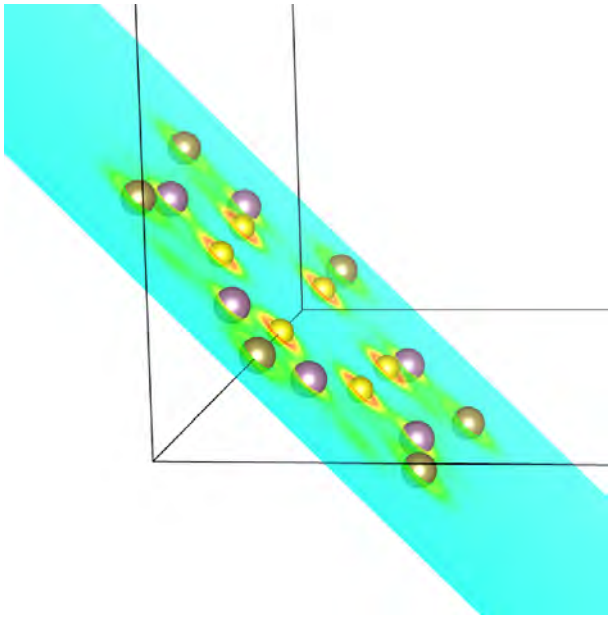

Figure 4.27: Equilibrium ionic positions and charge density for reduced spherical TeMoS after ionic relaxation. The inner, middle and outer spheres comprise S, Mo and Te atoms respectively. Only the slice and atoms that it cuts through is shown here.

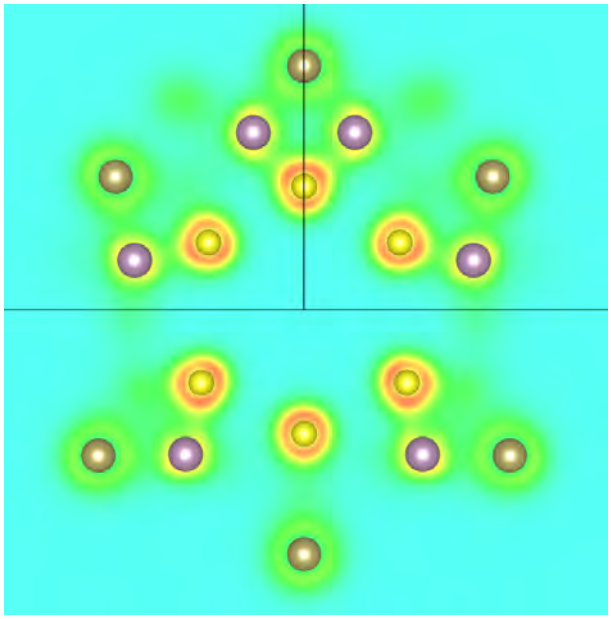

Figure 4.28: Equilibrium ionic positions and charge density for reduced spherical TeMoS after ionic relaxation. The inner, middle and outer spheres comprise S, Mo and Te atoms respectively. Only the slice and atoms that it cuts through is shown here. As expected, there is a higher charge density around the S ions than the Te ions.

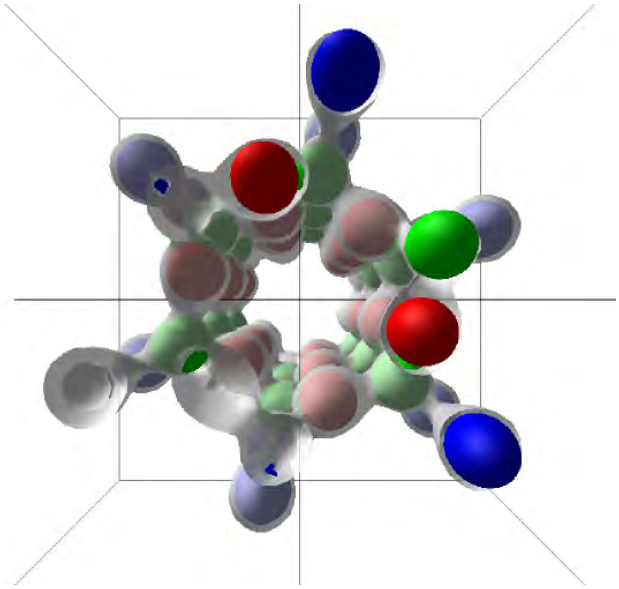

Figure 4.29: Equilibrium charge density (front *perspective* view) for $(-3, 3)$ *armchair* nanotube TeMoS. Inner red atoms are S atoms, middle green atoms are Mo atoms, and outer blue atoms are Te atoms. The grey surface is a charge density isosurface.

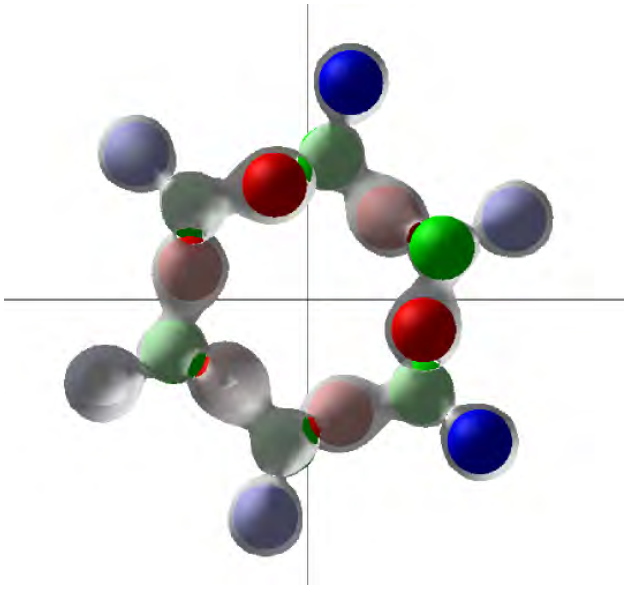

Figure 4.30: Equilibrium charge density (front *orthographic* view) for $(-3, 3)$ *armchair* nanotube TeMoS. Inner red atoms are S atoms, middle green atoms are Mo atoms, and outer blue atoms are Te atoms. The grey surface is a charge density isosurface.

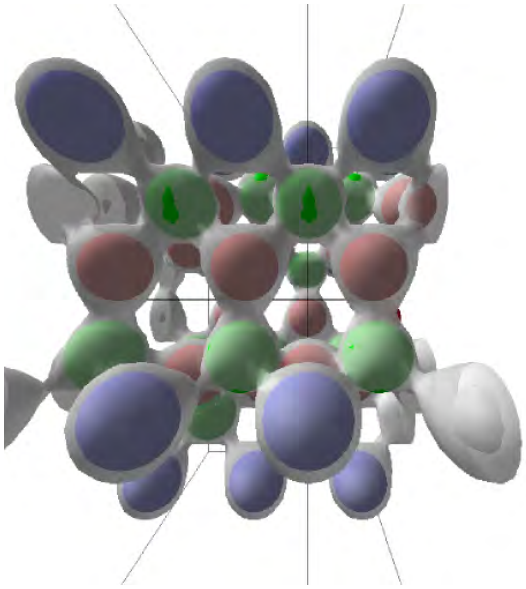

Figure 4.31: Equilibrium charge density (side view) for $(-3, 3)$ *armchair* nanotube TeMoS. Inner red atoms are S atoms, middle green atoms are Mo atoms, and outer blue atoms are Te atoms. The grey surface is a charge density isosurface.

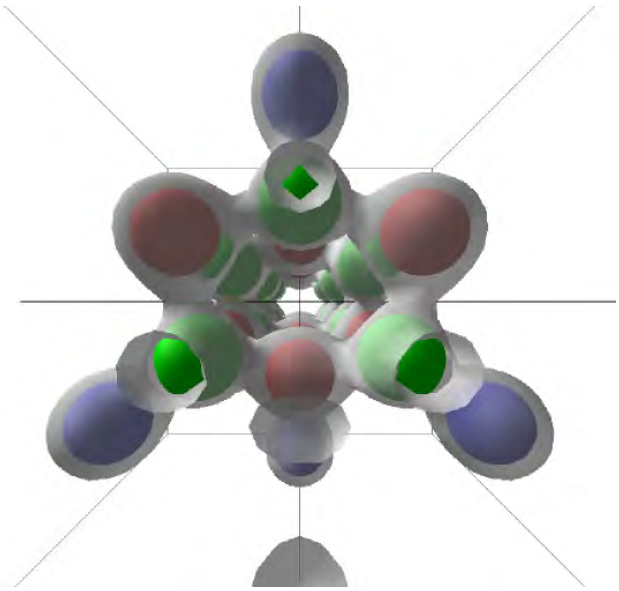

Figure 4.32: Equilibrium charge density (front *perspective* view) for $(0, 3)$ *zigzag* nanotube TeMoS. Inner red atoms are S atoms, middle green atoms are Mo atoms, and outer blue atoms are Te atoms. The grey surface is a charge density isosurface.

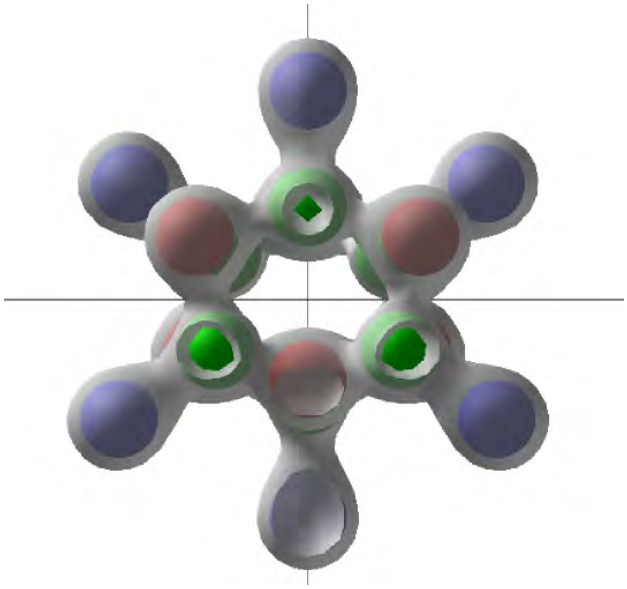

Figure 4.33: Equilibrium charge density (front *orthographic* view) for $(0, 3)$ *zigzag* nanotube TeMoS. Inner red atoms are S atoms, middle green atoms are Mo atoms, and outer blue atoms are Te atoms. The grey surface is a charge density isosurface.

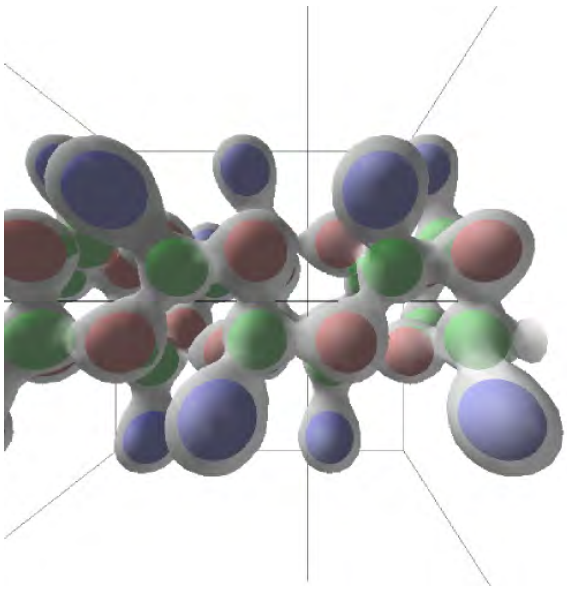

Figure 4.34: Equilibrium charge density (side view) for $(0, 3)$ *zigzag* nanotube TeMoS. Inner red atoms are S atoms, middle green atoms are Mo atoms, and outer blue atoms are Te atoms. The grey surface is a charge density isosurface.

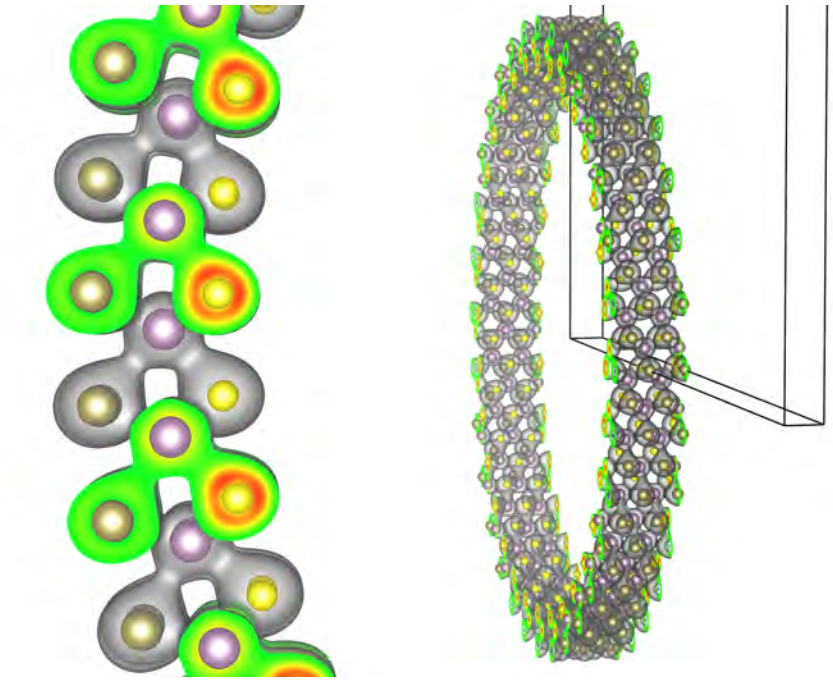

Figure 4.35: Equilibrium charge density for optimal armchair nanotube with parameters listed in table 3.5. The radius is large for a nanotube. Inner yellow ions are S ions, middle purple ions are Mo ions, and outer greyish-brown ions are Te ions. As expected, the more electronegative S atoms capture a greater charge density.

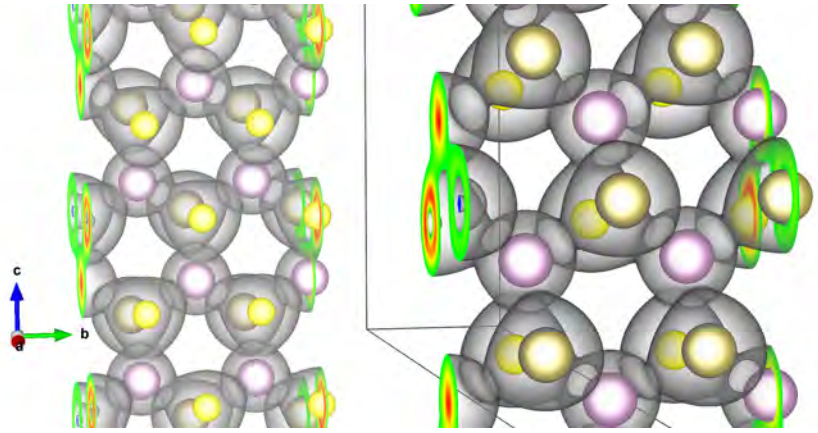

Figure 4.36: Another view of equilibrium charge density for optimal armchair nanotube. Inner yellow ions are S ions, middle purple ions are Mo ions, and outer greyish-brown ions are Te ions.

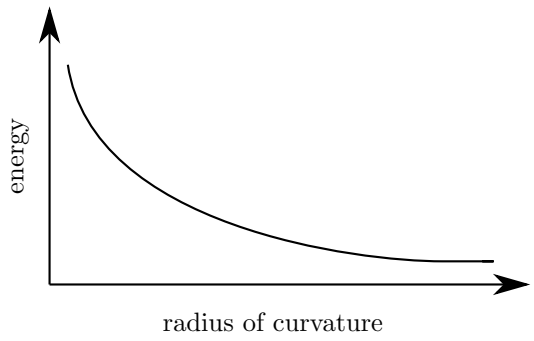

(a) No minimum for carbon or symmetric TMD nanotubes. Their lowest energy state is flat, which means the lowest energy occurs at an infinitely large radius of curvature.

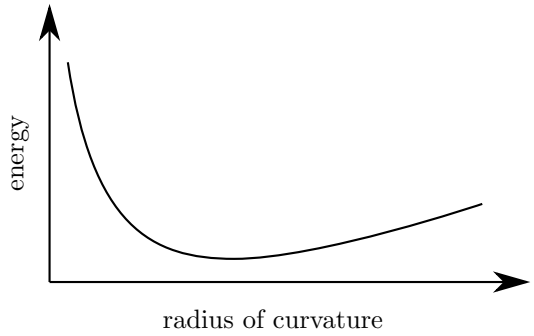

(b) Expected minimum for aTMD nanotubes. Asymmetry causes aTMDs to curl up to an optimal radius of curvature, which means the lowest energy occurs at a finite radius of curvature.

Figure 4.37: Difference in energy vs. radius of curvature between symmetric and asymmetric TMD nanotubes.

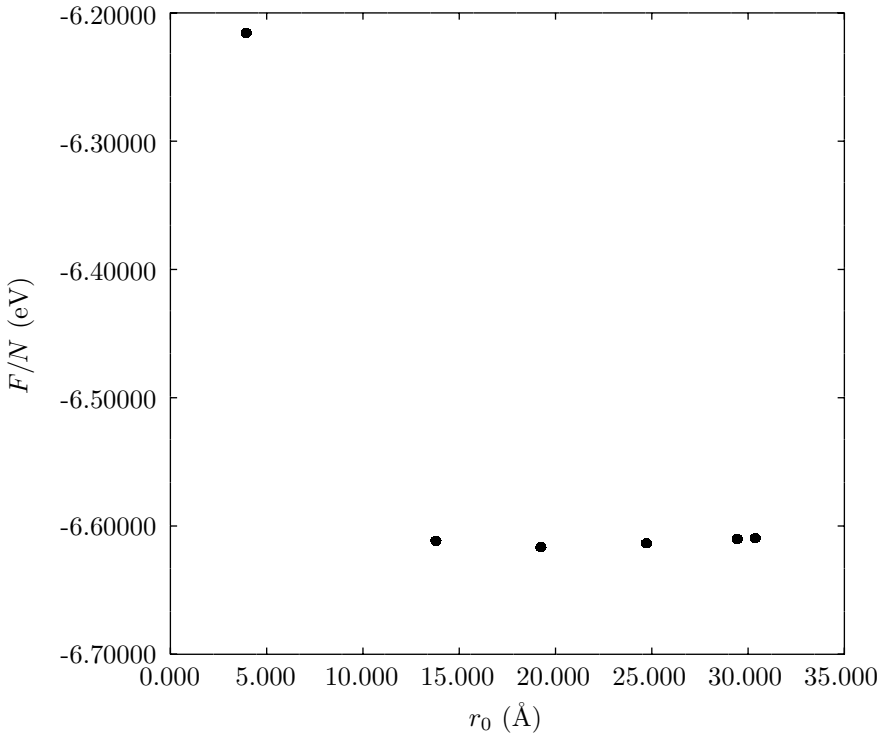

Figure 4.38: Average energy per atom F/N vs. radius of curvature r_0 for *arm-chair* nanotube, where F is the total energy per primitive cell and N is the number of atoms in the primitive cell. The primitive lattice constant L along the tube's axis is kept fixed for all plotted points.

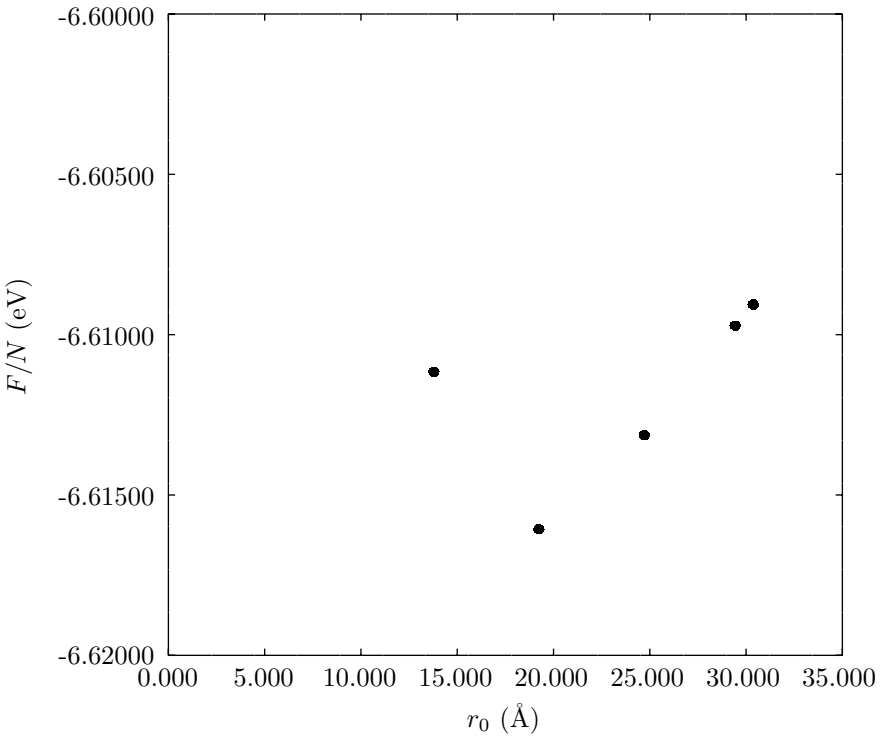

Figure 4.39: Average energy per atom F/N vs. radius of curvature r_0 (zoomed in) for *armchair* nanotube, where F is the total energy per primitive cell and N is the number of atoms in the primitive cell. The difference in energy for different radii is around 0.005 eV and is small, which means that aTMDs are not very sensitive to changes in radius of curvature.

carbon nanotubes. The insensitivity of aTMDs to changes in radius of curvature agrees intuitively with the fact that TMDs are flexible and can bend easily without breaking [2].

Figures A.34 and A.35 show the energy vs. radius plot for zigzag TeMoS nanotubes. However, due to time constraint and more expensive DFT computation (there are more ions in a primitive cell for zigzag nanotubes), the plot is not complete and is left to be done as future work.

Chapter 5

Conclusion

We set out to optimise the flat, nanotube and spherical structures of monolayer aTMDs by minimising their energy with respect to parameters, such as the lattice constant and radius of curvature. Special attention was given to TeMoS because the electronegativities of Te and S are most different among suitable chalcogens, and we expect its highest asymmetry to give it the most interesting properties.

Forcing monolayer aTMDs to be flat, we optimised the lattice parameter for various aTMDs and symmetric TMDs. We expect these values for aTMDs to be accurate because our results for TMDs agree well with experimental data. As expected, we found significant charge transfer and a corresponding dipole moment for flat aTMDs. We also found that among all the (a)TMDs, TeMoS is the only material with an indirect band gap. This can be explained by strain effects felt by the Te and S chalcogens.

However, due to different M-X and M-Y bond lengths for a aTMD XMY, the aTMD should curl up into a sphere naturally. In principle, we should minimise the energy of such a spherical structure with respect to the radius of curvature. However, an estimate of the optimal radius of curvature for TeMoS, based on the lattice parameters of MoS_2, $MoTe_2$ and TeMoS, is so large that the sheer number of ions involved makes DFT computation too expensive. We only gave a method for initialising the spherical structure using geodesic spheres. Perhaps when computers become faster or when DFT computation becomes more efficient, other researchers can complete our work to investigate such a large spherical structure.

A direct proof of the natural curvature of aTMDs requires a minimum in the energy vs. radius of curvature plot. Although DFT treatment for spherical aTMDs is too expensive, we can still obtain the energy vs. radius plot for nanotube aTMDs. This is because the periodic boundary condition applies along the tube's axis, thereby drastically reducing the number of ions in the primitive unit cell. We then showed that there is indeed a minimum in the energy vs. radius plot for armchair TeMoS under the constraint of a fixed lattice constant (along the tube's axis). In the future where the time constraint of this project

does not apply, we should let L vary to obtain the fully relaxed states near the minimum of the energy vs. radius plot. We should also complete the plot for zigzag variants. Additionally, we can compute the band structures for these two types of nanotubes.

aTMDs, by virtue of their dipole moment may lead to superlattices with interesting properties. Their dual surface properties may be used to fabricate new interesting devices. Moreover, aTMDs' natural curvature may make them stabler nanotubes. In this work, we optimised the electronic structure of various structures of aTMDs, but we did not have the time to explore many other mechanical and electrical properties. Nevertheless, many mechanical properties are actually based on the derivatives of energy. Having found the electronic and ionic charge distributions, as well as energies of aTMD nano-structures, we hope to have laid the foundations and paved the way for future studies of aTMDs.

Appendix A

Extra figures

A.1 Flat TMDs and aTMDs

A.1.1 Equilibrium lattice parameter

Figures A.1 to A.10 show the energy vs. lattice parameter plots for various (a)TMDs. For every material, there is a rough plot which identifies the rough location of the minimum, and a fine plot which fits a quadratic curve to the points to find the equilibrium lattice parameter.

A.1.2 Dipole moment

Figures A.11 to A.15 show the sum of charge density $n(z)$ in the x-y plane of the primitive cell for a certain z for various flat (a)TMDs.

A.1.3 Density of states

Figures A.16 to A.21 show the atom and orbital decomposed density of states for various (a)TMDs.

A.1.4 Band structure

Figures A.22 to A.33 show the band structures for various (a)TMDs. For every material, there is the overall and enlarged (near the Fermi level) band structure.

A.2 Nanotube aTMDs

A.2.1 Energy vs. radius of curvature

Figures A.34 and A.35 show the energy vs. radius plot for the zigzag nanotube.

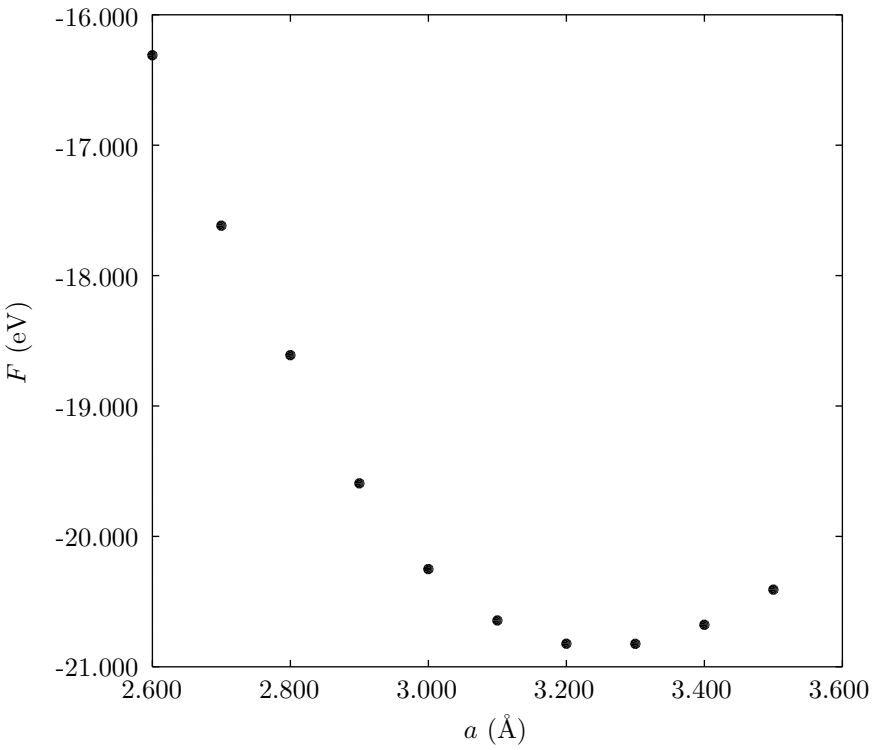

Figure A.1: Rough plot of total energy F per super-cell defined by vectors $\mathbf{a}_1$, $\mathbf{a}_2$ and $\mathbf{a}_3$ vs. lattice parameter $a = |\mathbf{a_1}| = |\mathbf{a_2}|$ for SeMoS.

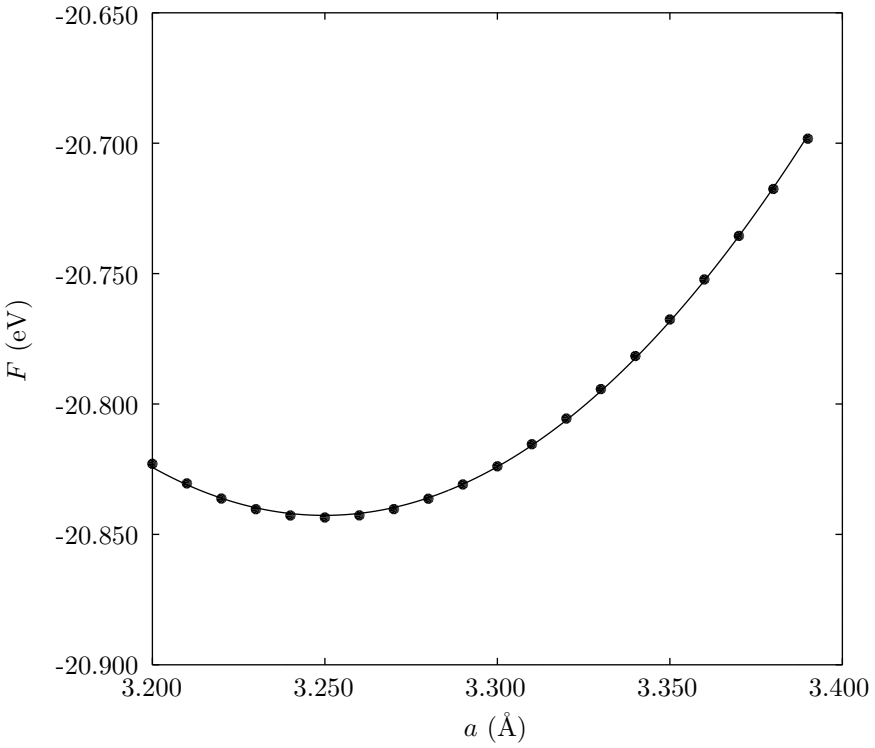

Figure A.2: Fine plot of total energy F per super-cell vs. lattice parameter $a = |\mathbf{a_1}| = |\mathbf{a_2}|$ for SeMoS.

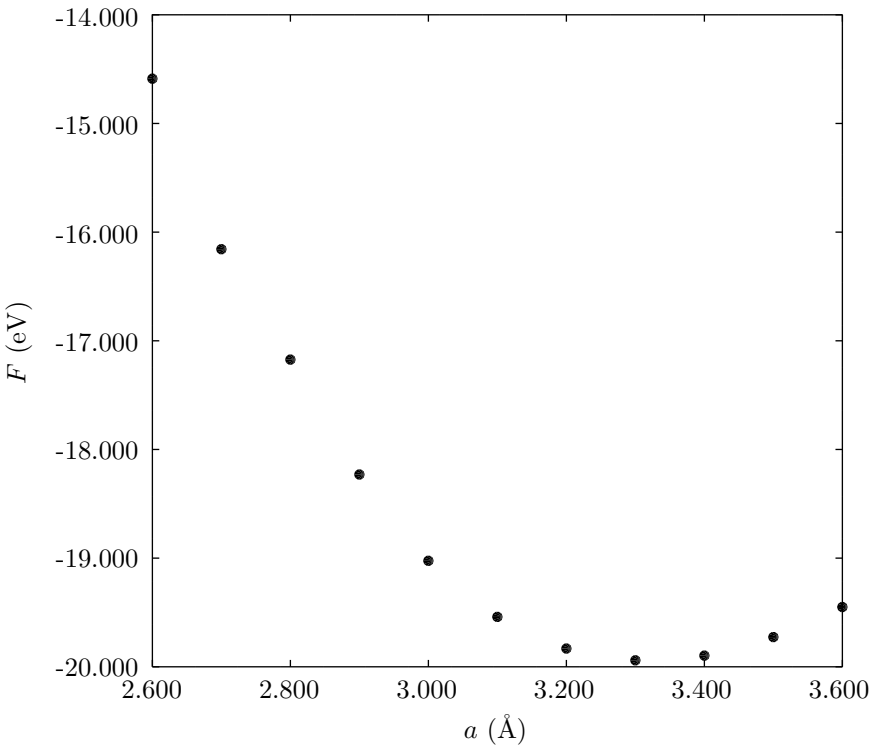

Figure A.3: Rough plot of total energy F per super-cell defined by vectors $\mathbf{a}_1$, $\mathbf{a}_2$ and $\mathbf{a}_3$ vs. lattice parameter $a = |\mathbf{a_1}| = |\mathbf{a_2}|$ for $MoSe_2$.

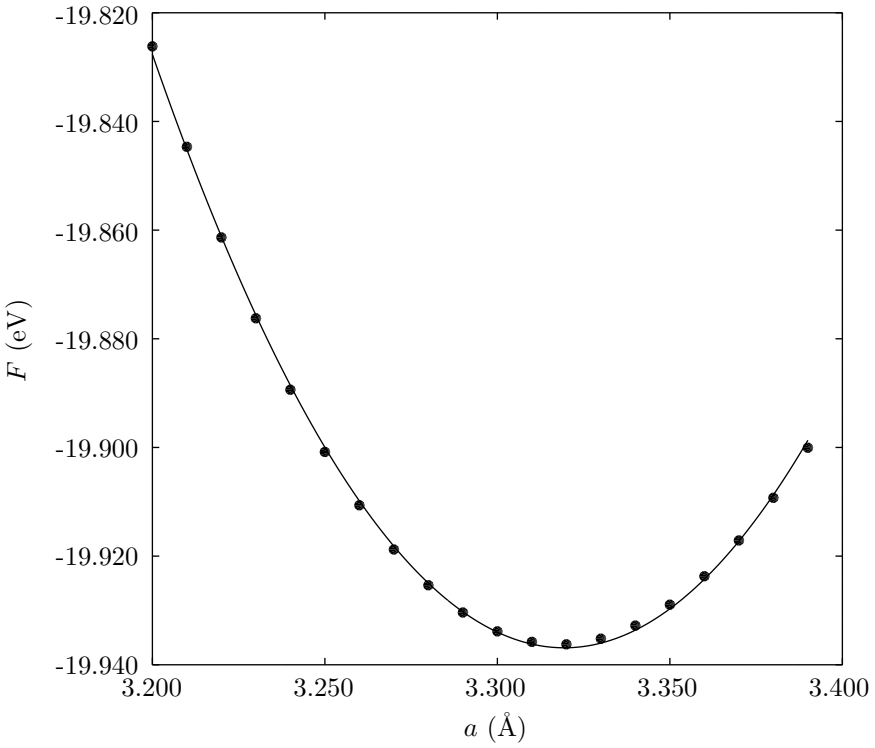

Figure A.4: Fine plot of total energy F per super-cell vs. lattice parameter $a = |\mathbf{a_1}| = |\mathbf{a_2}|$ for $MoSe_2$.

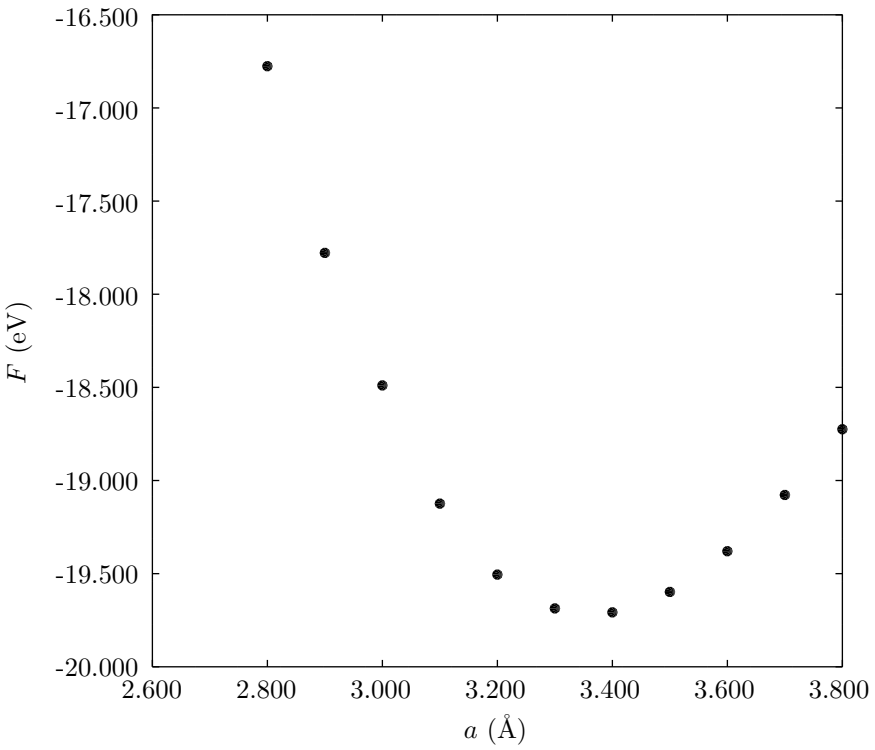

Figure A.5: Rough plot of total energy F per super-cell defined by vectors $\mathbf{a}_1$, $\mathbf{a}_2$ and $\mathbf{a}_3$ vs. lattice parameter $a = |\mathbf{a_1}| = |\mathbf{a_2}|$ for TeMoS.

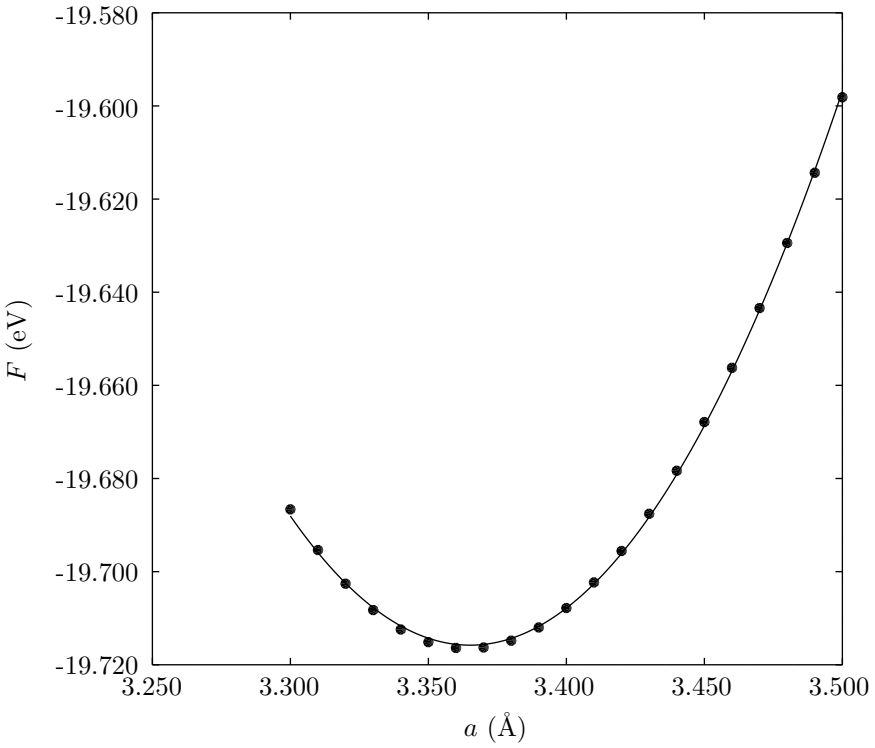

Figure A.6: Fine plot of total energy F per super-cell vs. lattice parameter $a = |\mathbf{a_1}| = |\mathbf{a_2}|$ for TeMoS.

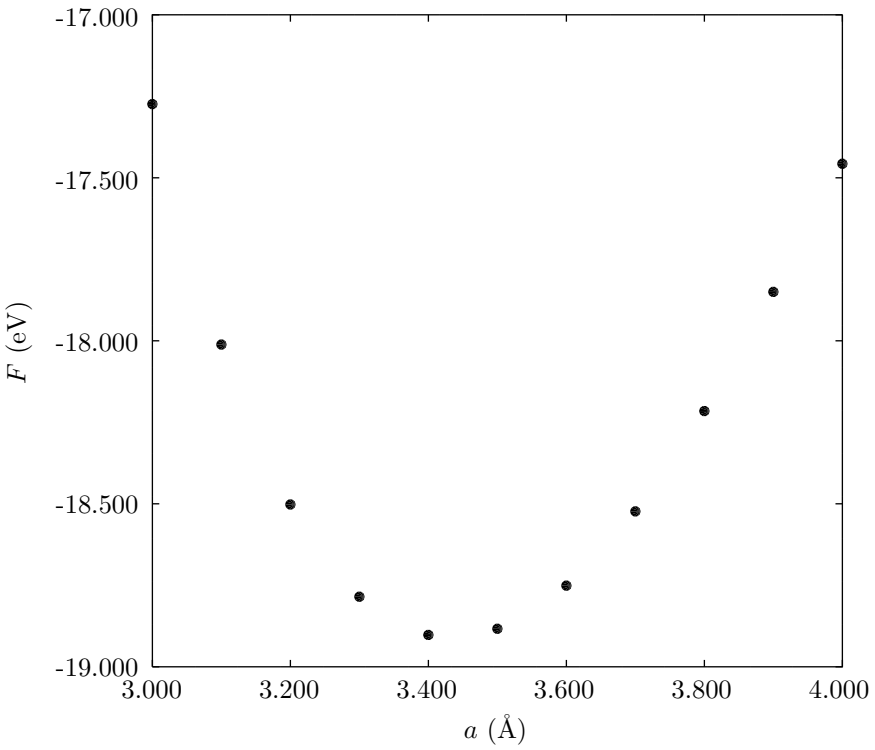

Figure A.7: Rough plot of total energy F per super-cell defined by vectors $\mathbf{a}_1$, $\mathbf{a}_2$ and $\mathbf{a}_3$ vs. lattice parameter $a = |\mathbf{a_1}| = |\mathbf{a_2}|$ for SeMoTe.

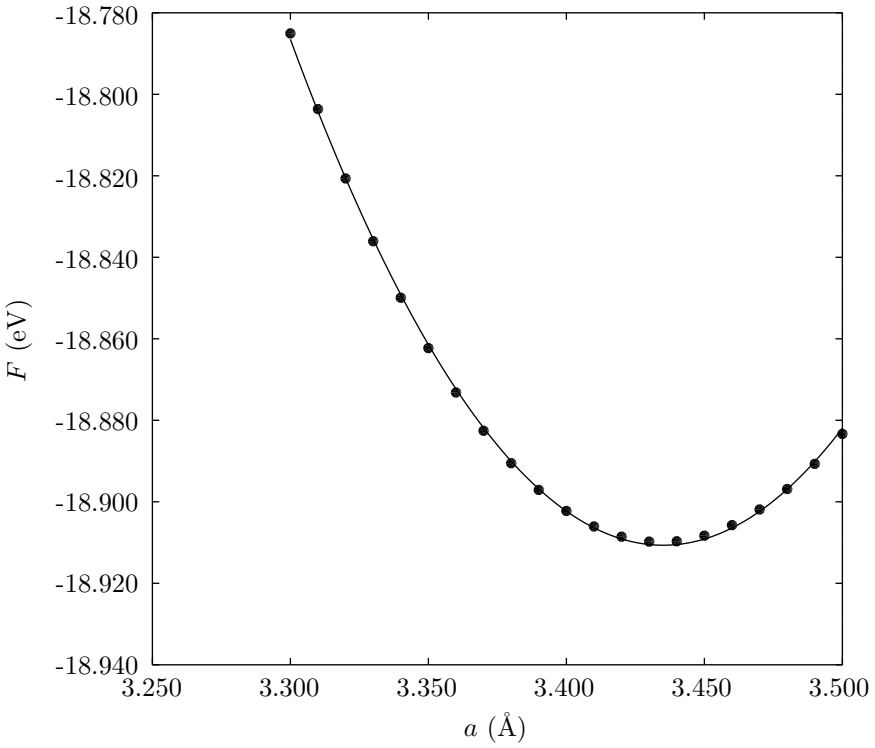

Figure A.8: Fine plot of total energy F per super-cell vs. lattice parameter $a = |\mathbf{a_1}| = |\mathbf{a_2}|$ for SeMoTe.

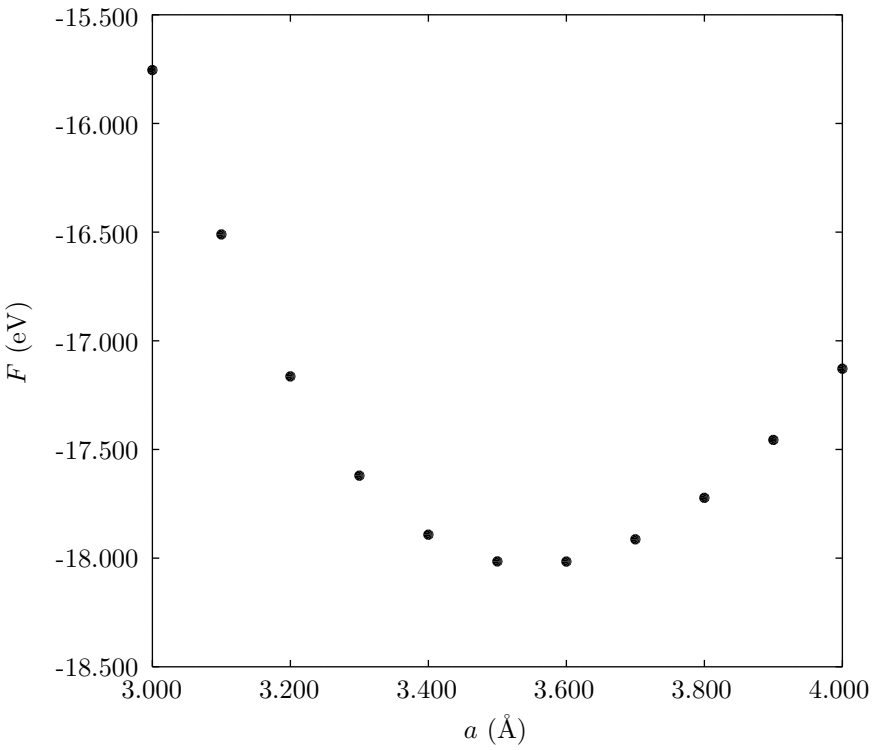

Figure A.9: Rough plot of total energy F per super-cell defined by vectors $\mathbf{a}_1$, $\mathbf{a}_2$ and $\mathbf{a}_3$ vs. lattice parameter $a = |\mathbf{a_1}| = |\mathbf{a_2}|$ for $MoTe_2$.

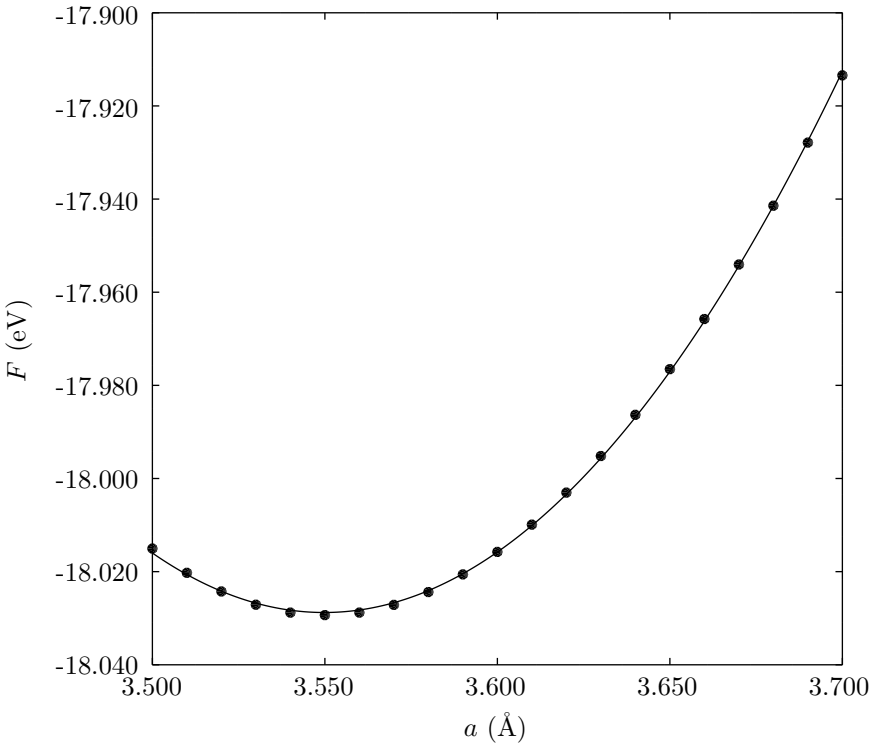

Figure A.10: Fine plot of total energy F per super-cell vs. lattice parameter $a = |\mathbf{a_1}| = |\mathbf{a_2}|$ for $MoTe_2$.

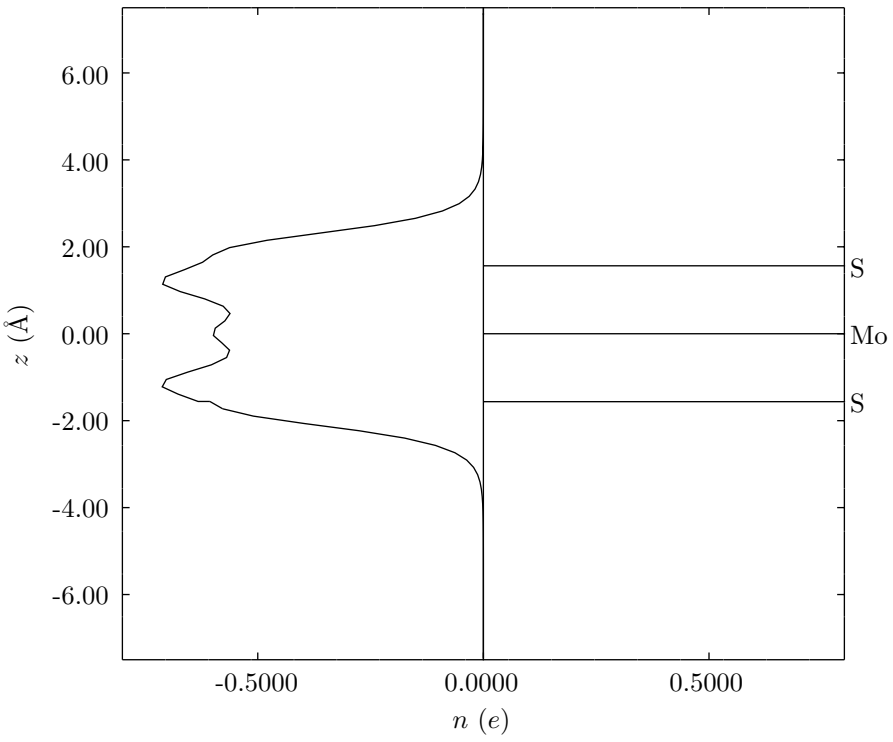

Figure A.11: Charge density $n(z)$ for MoS_2.

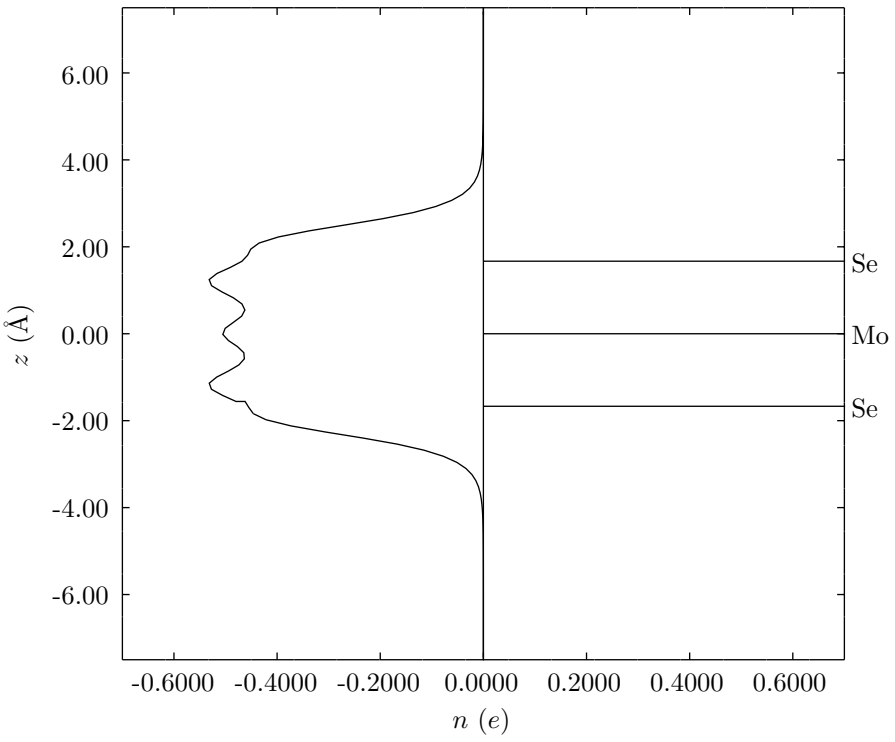

Figure A.12: Charge density $n(z)$ for $MoSe_2$.

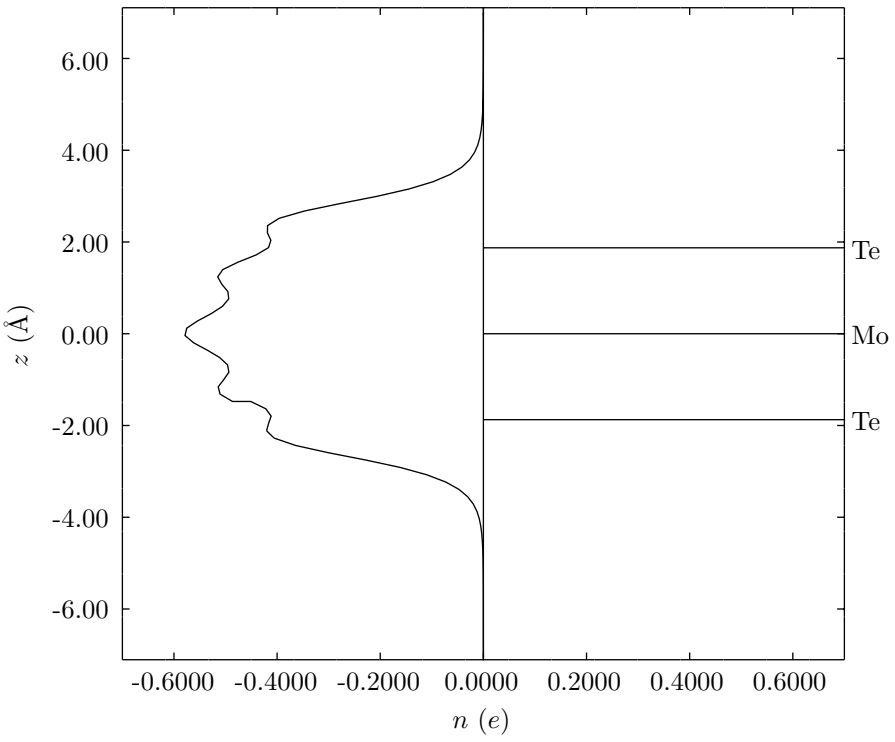

Figure A.13: Charge density $n(z)$ for $MoTe_2$.

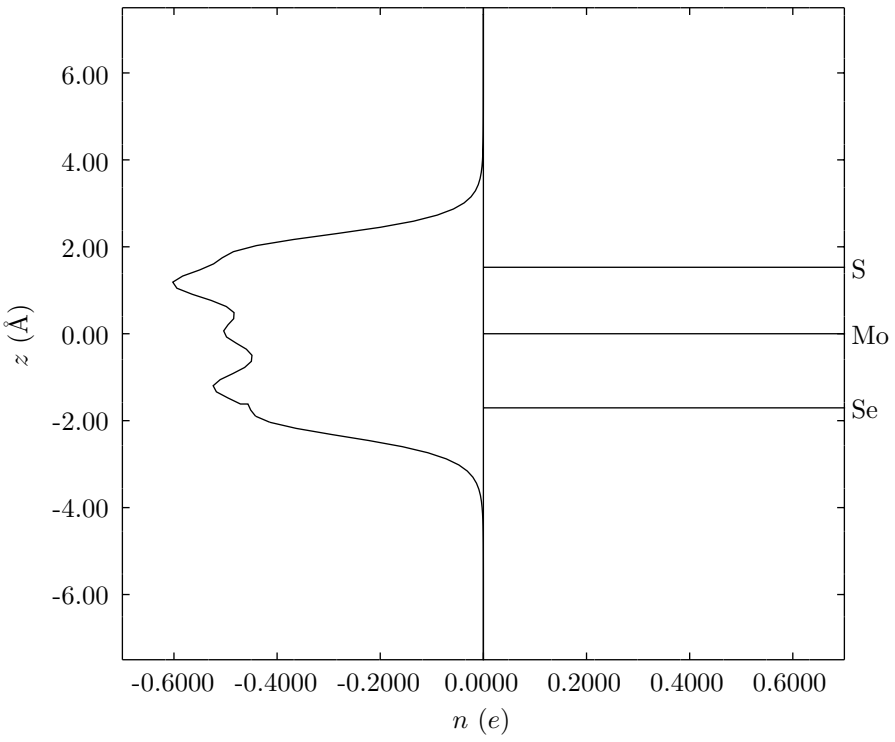

Figure A.14: Charge density $n(z)$ for SeMoS.

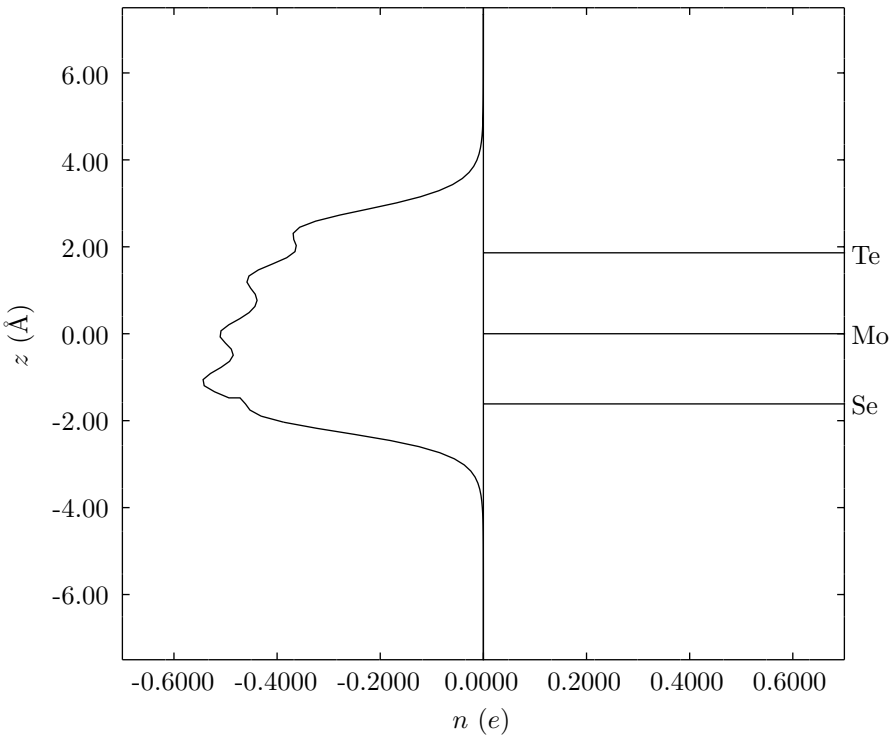

Figure A.15: Charge density $n(z)$ for SeMoTe.

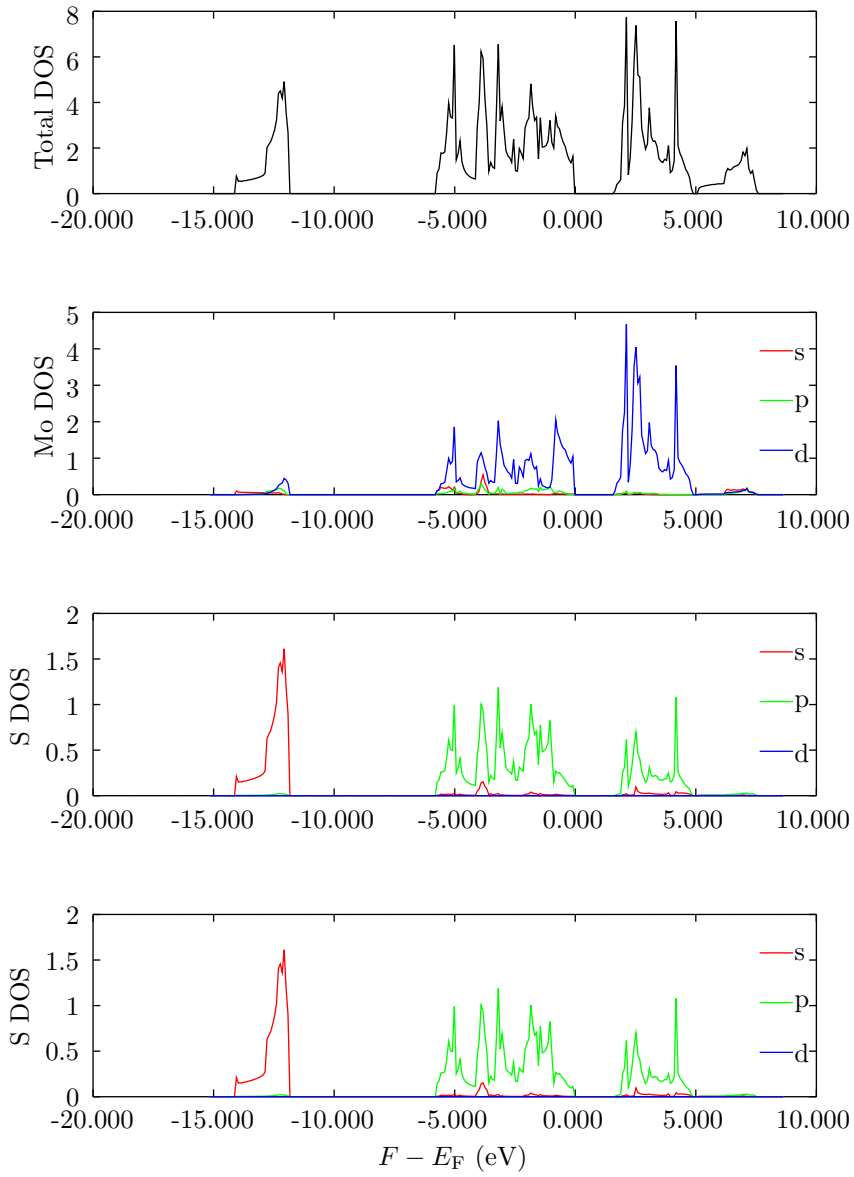

Figure A.16: Atom and orbital decomposed density of states for MoS_2.

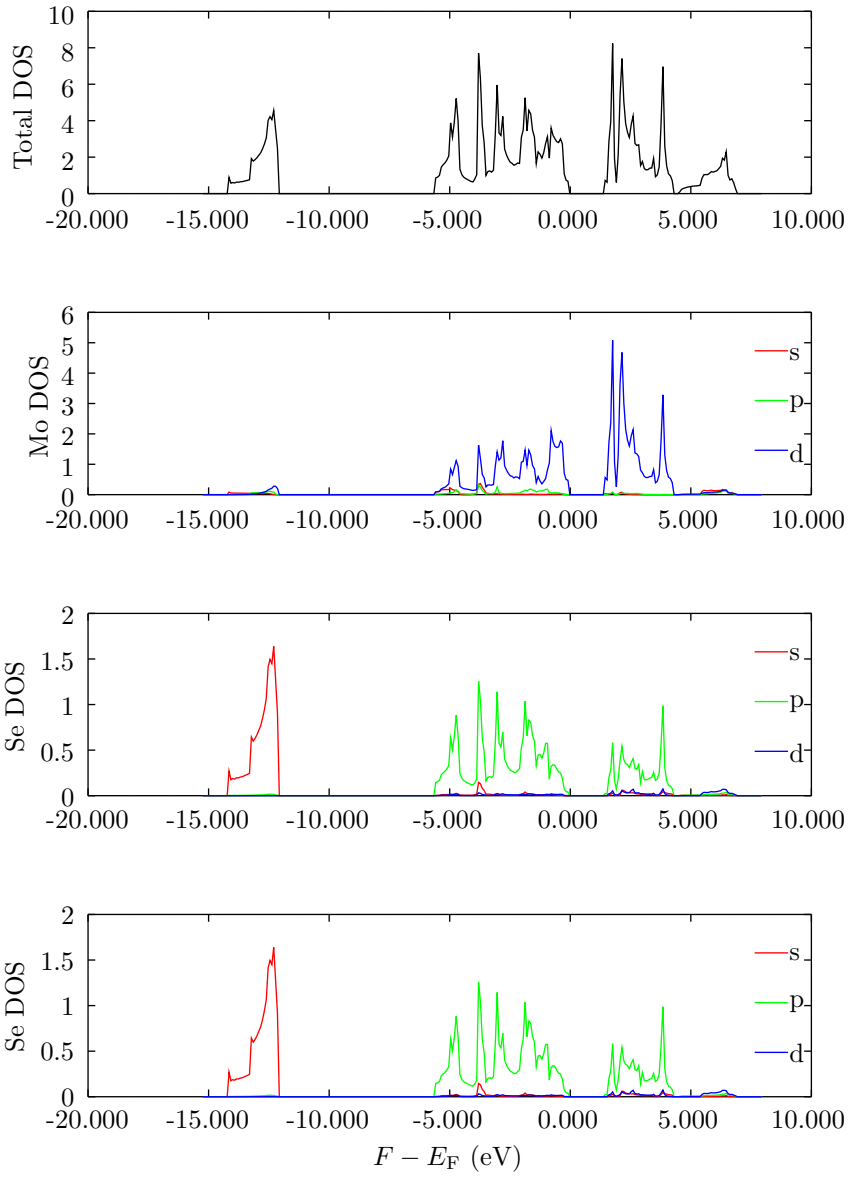

Figure A.17: Atom and orbital decomposed density of states for $MoSe_2$.

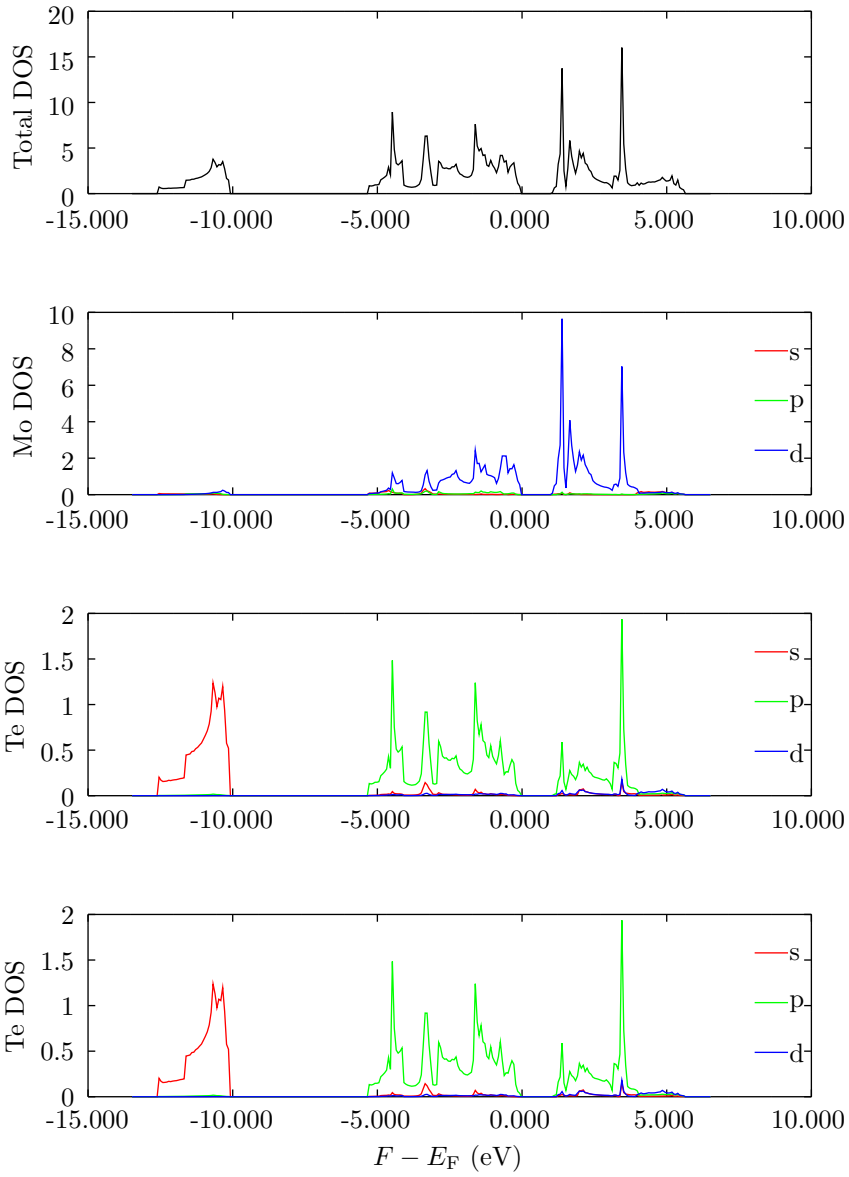

Figure A.18: Atom and orbital decomposed density of states for $MoTe_2$.

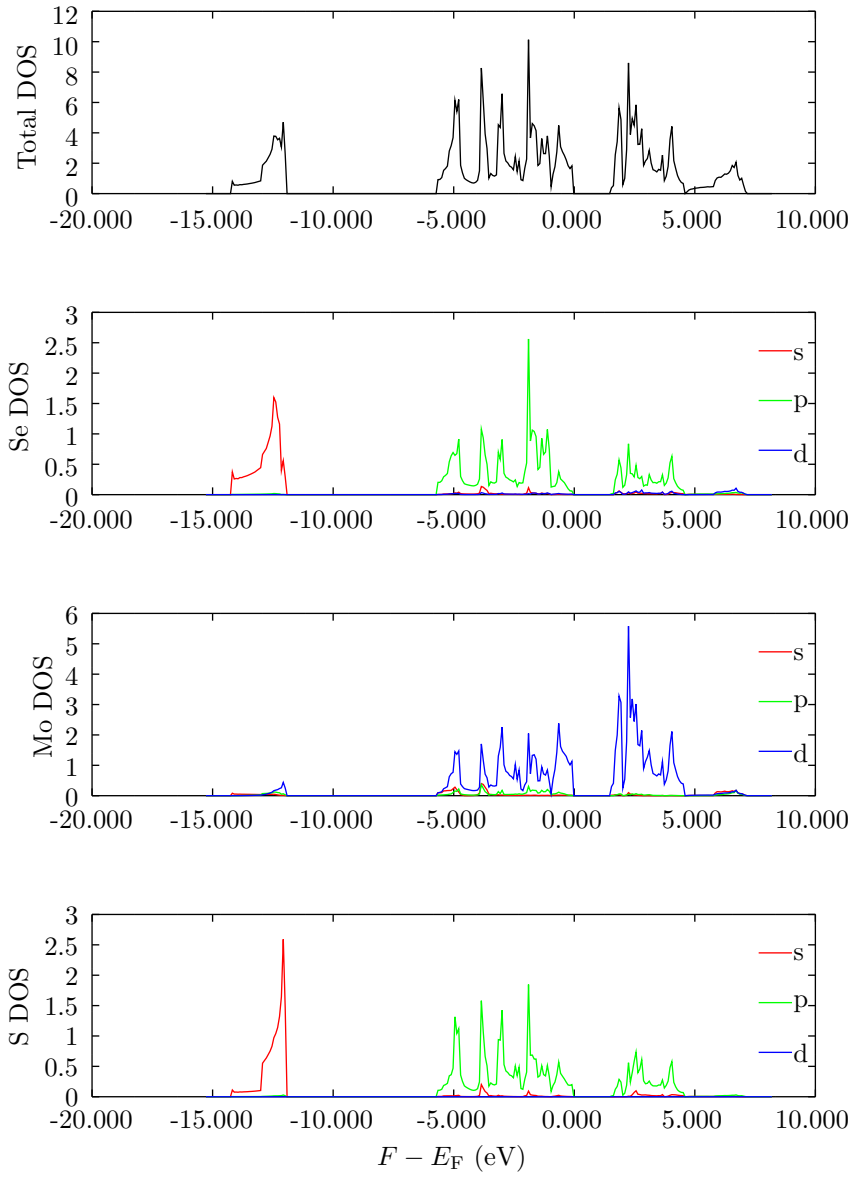

Figure A.19: Atom and orbital decomposed density of states for SeMoS.

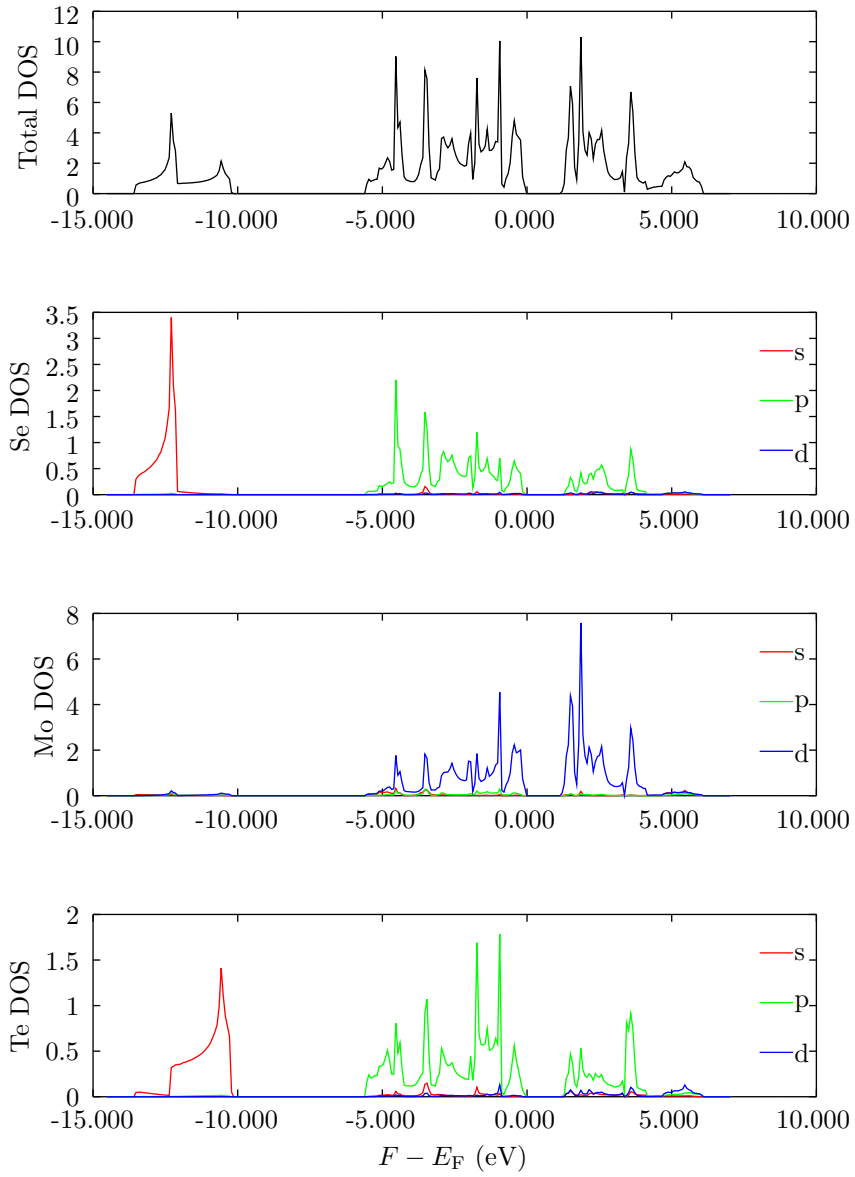

Figure A.20: Atom and orbital decomposed density of states for SeMoTe.

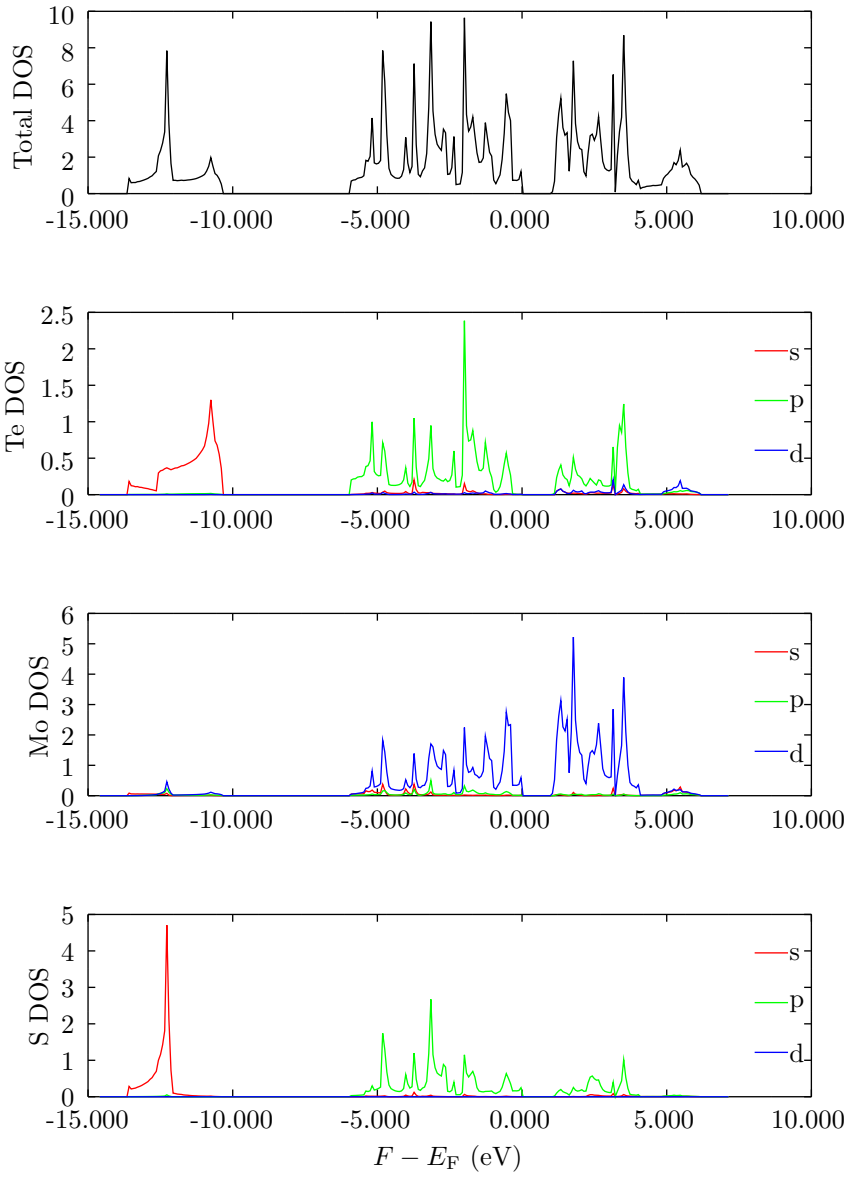

Figure A.21: Atom and orbital decomposed density of states for TeMoS.

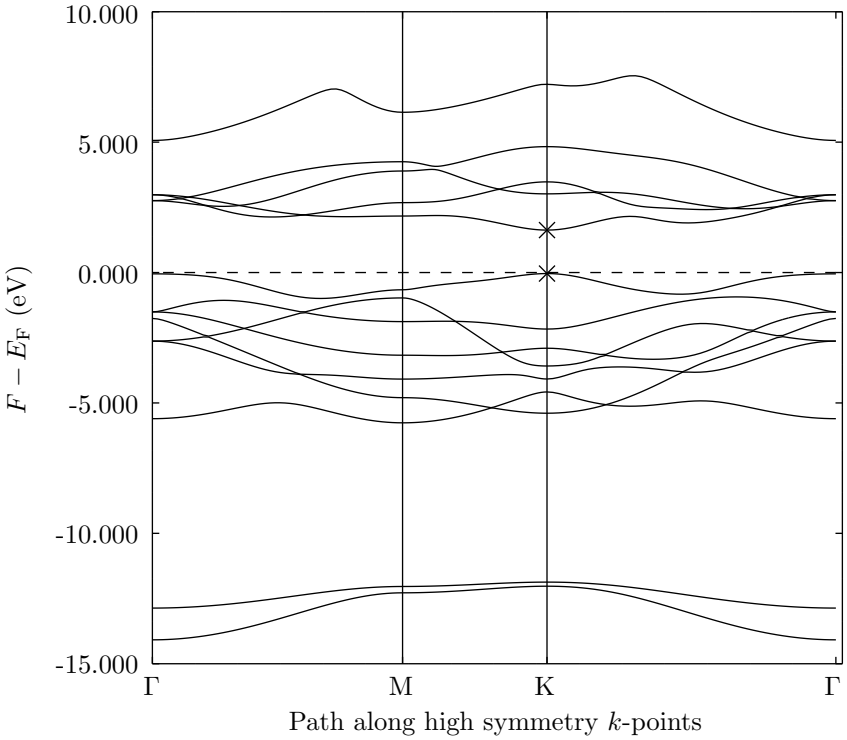

Figure A.22: Band structure for MoS_2.

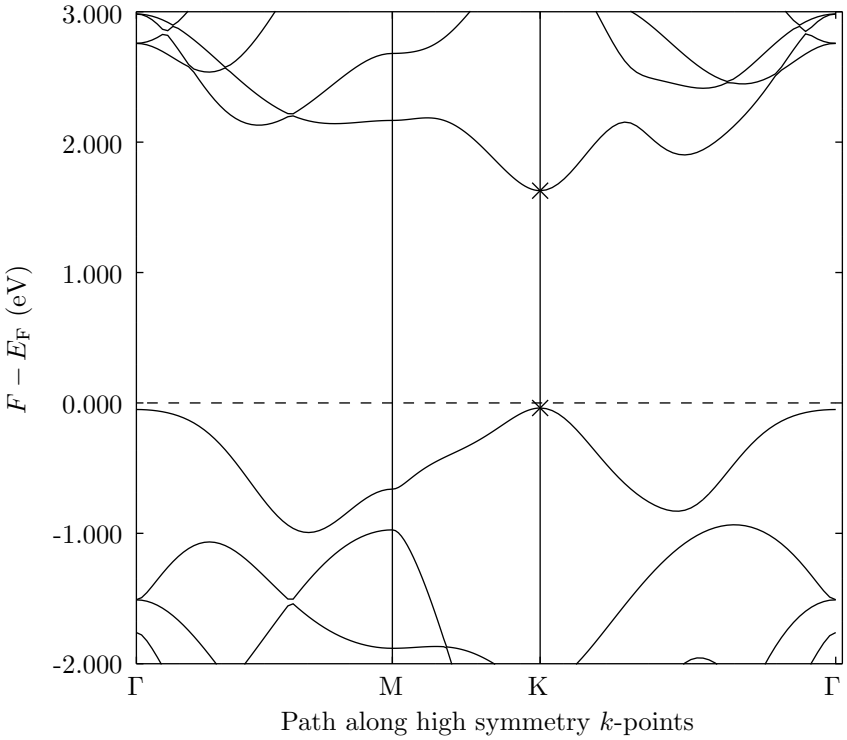

Figure A.23: Band structure (enlarged) for MoS_2.

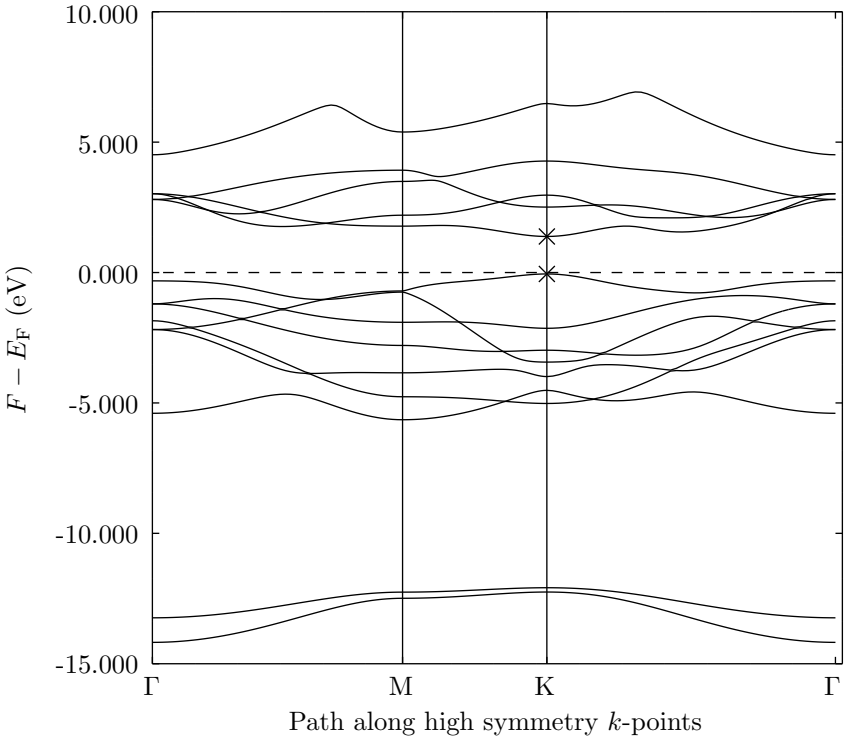

Figure A.24: Band structure for $MoSe_2$.

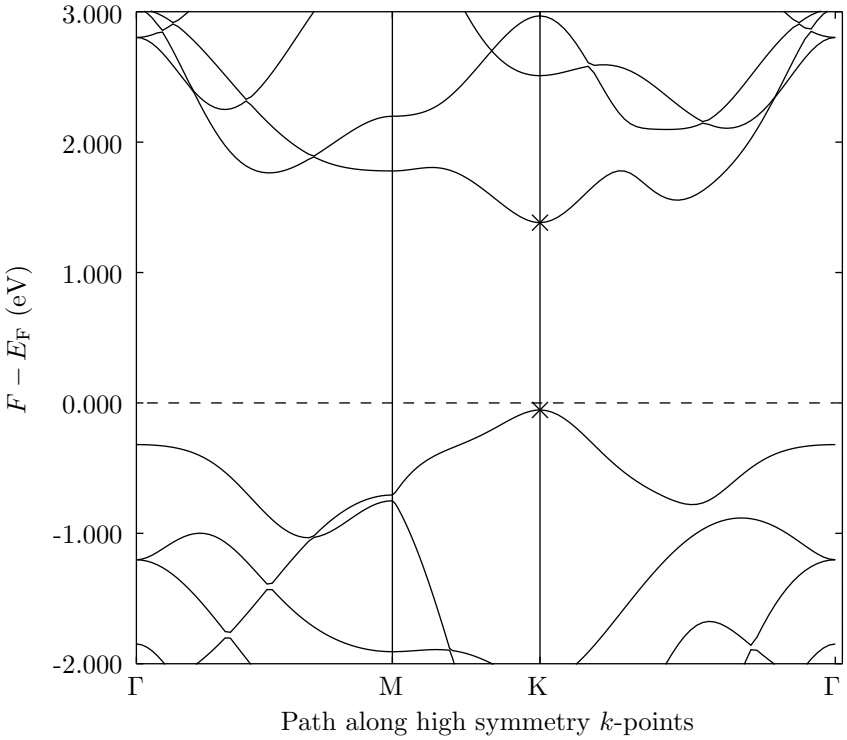

Figure A.25: Band structure (enlarged) for $MoSe_2$.

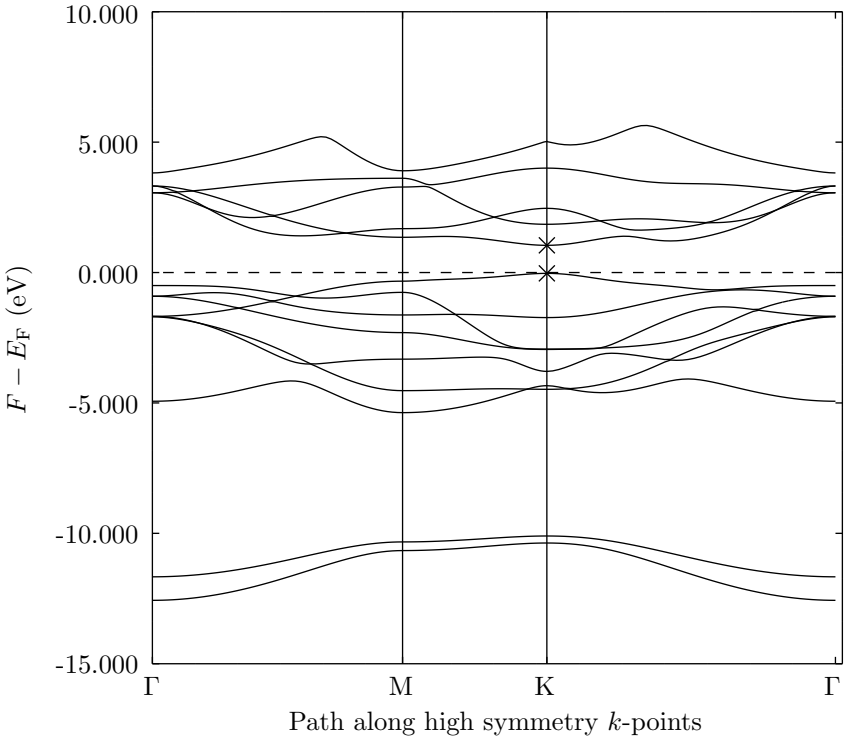

Figure A.26: Band structure for $MoTe_2$.

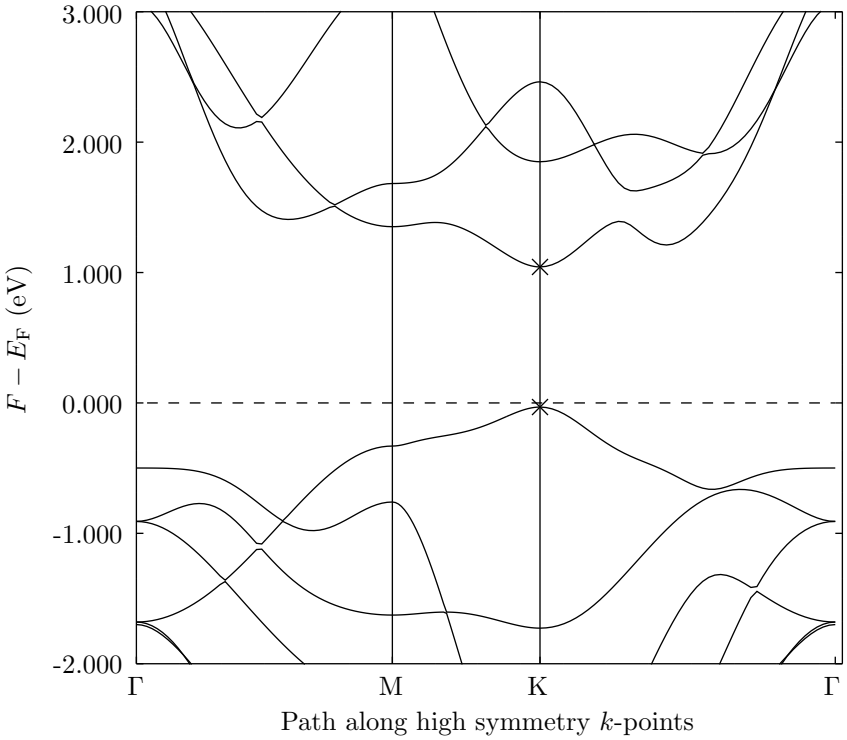

Figure A.27: Band structure (enlarged) for $MoTe_2$.

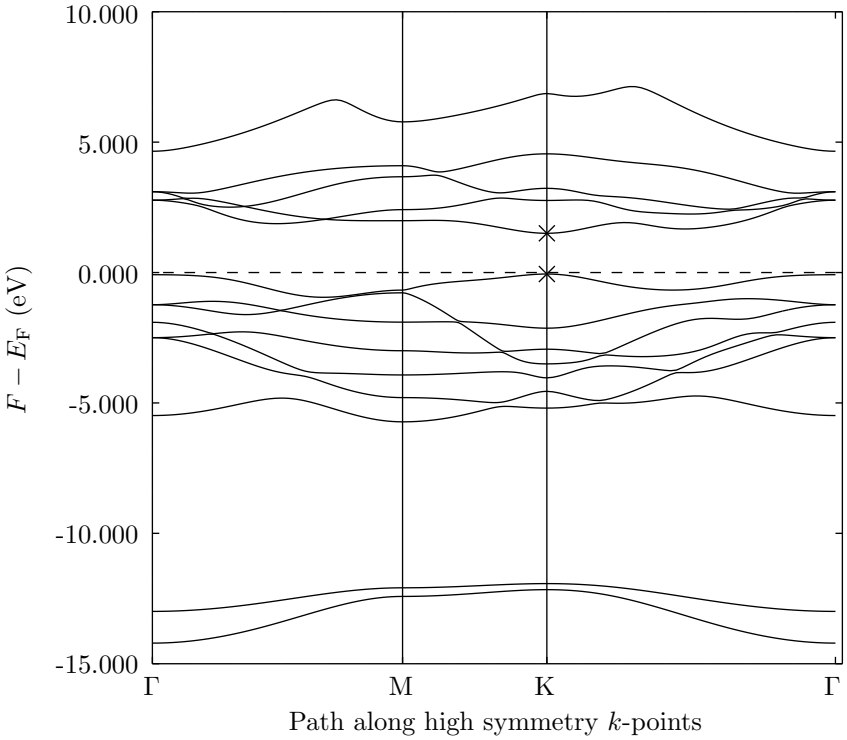

Figure A.28: Band structure for SeMoS.

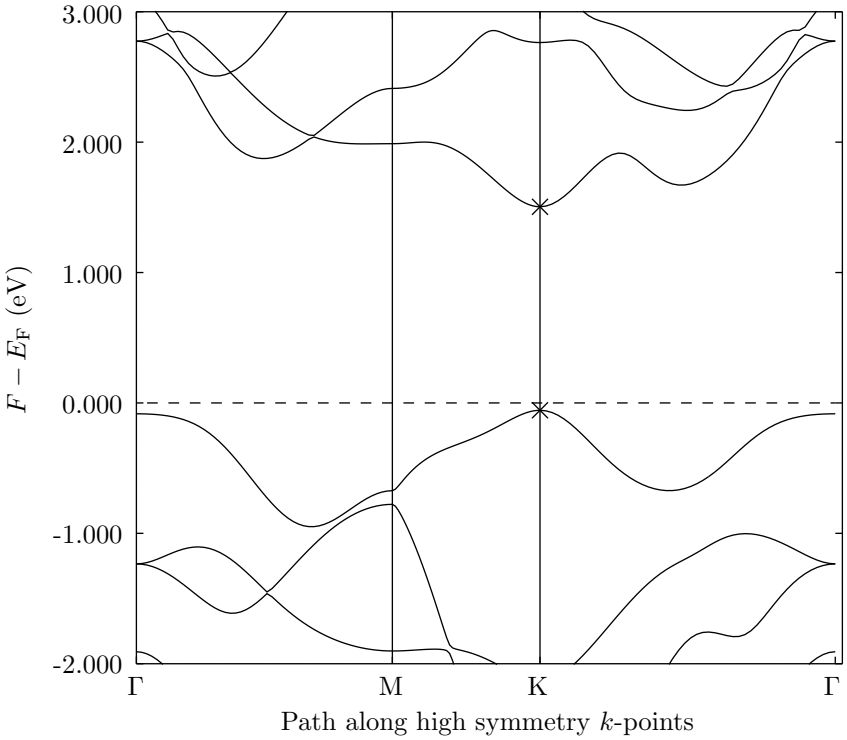

Figure A.29: Band structure (enlarged) for SeMoS.

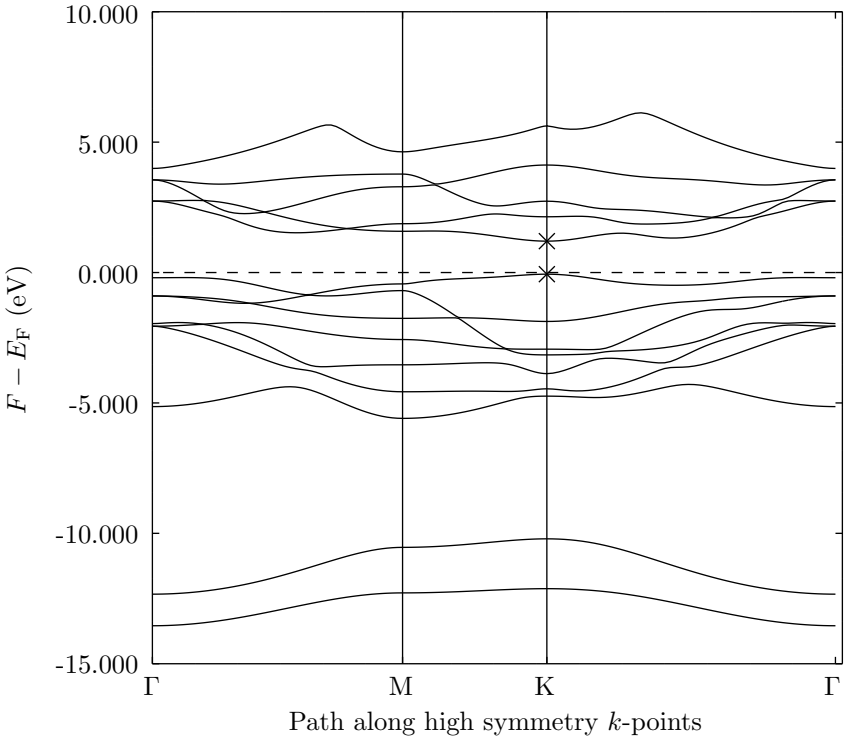

Figure A.30: Band structure for SeMoTe.

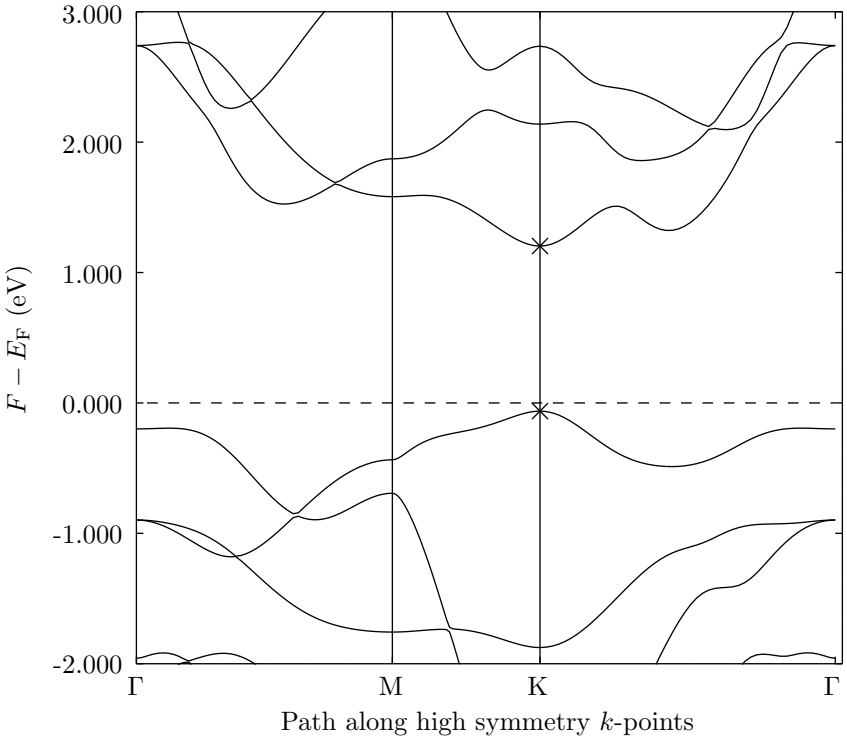

Figure A.31: Band structure (enlarged) for SeMoTe.

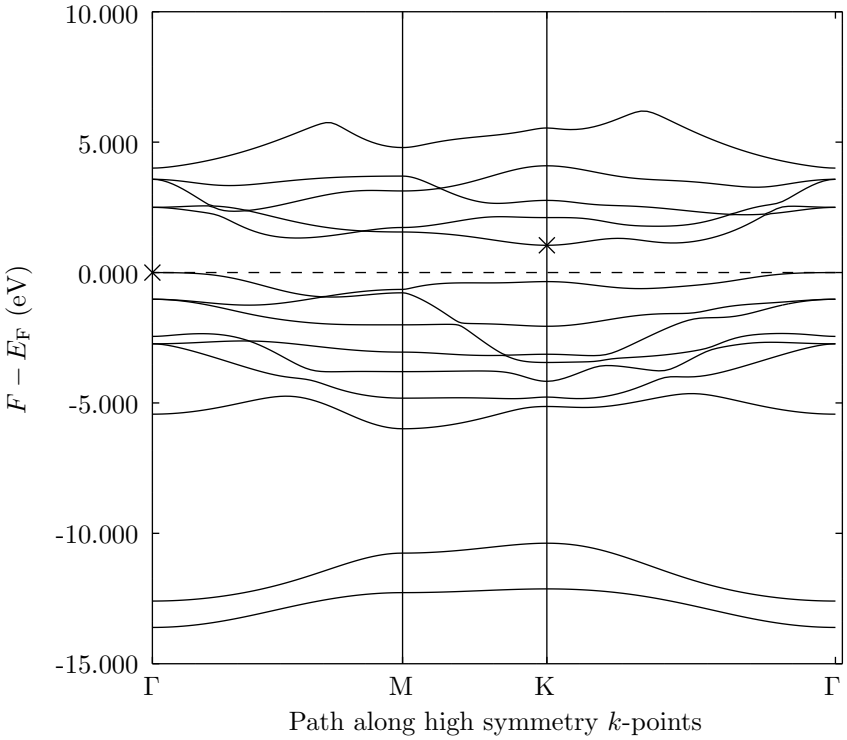

Figure A.32: Band structure for TeMoS.

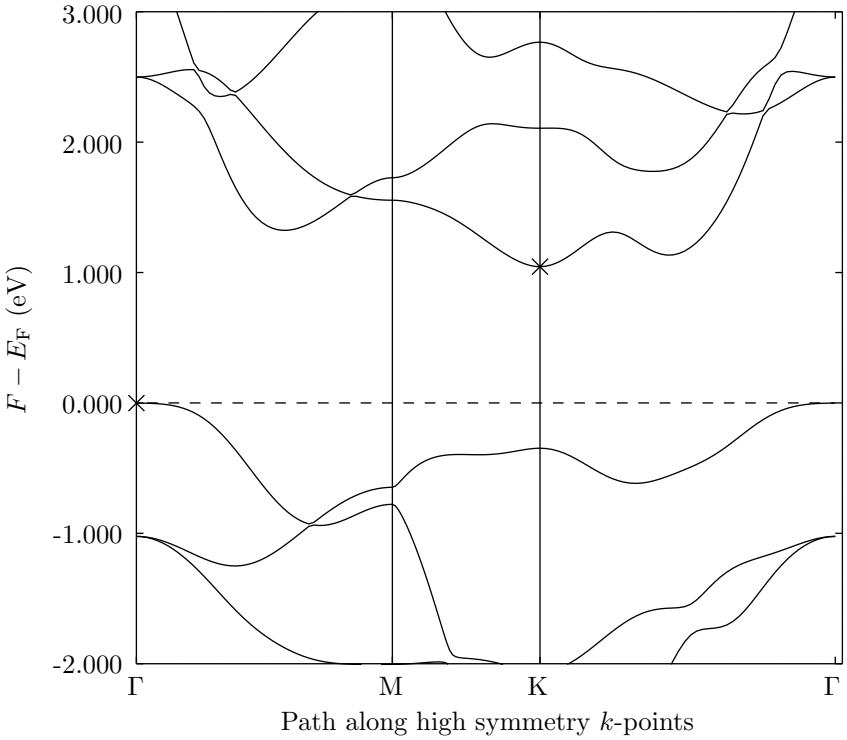

Figure A.33: Band structure (enlarged) for TeMoS.

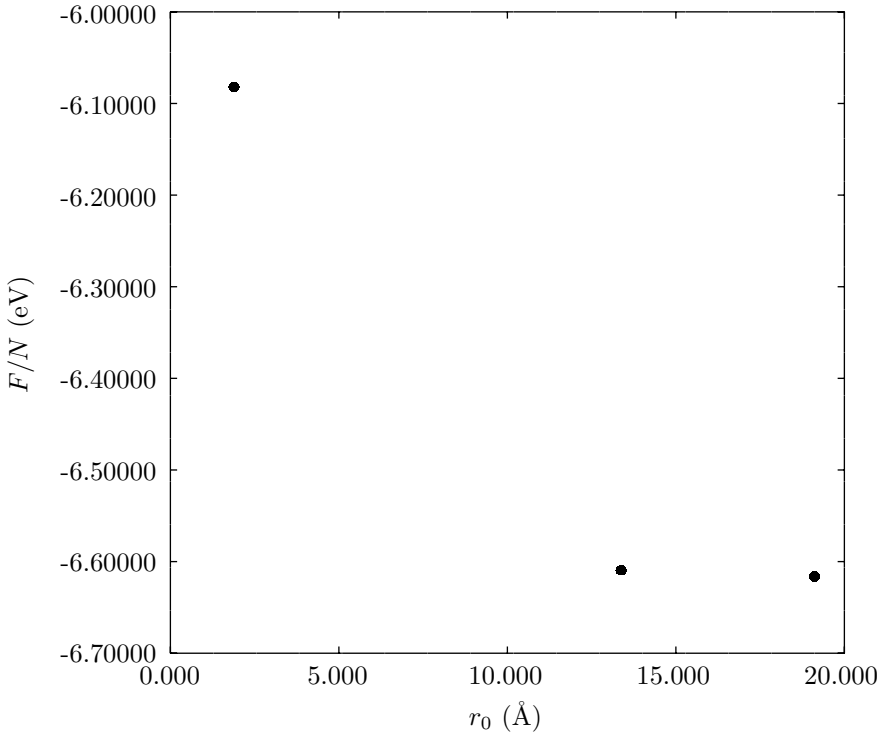

Figure A.34: Average energy per atom F/N vs. radius of curvature r_0 for *zigzag* nanotube, where F is the total energy per primitive cell and N is the number of atoms in the primitive cell.

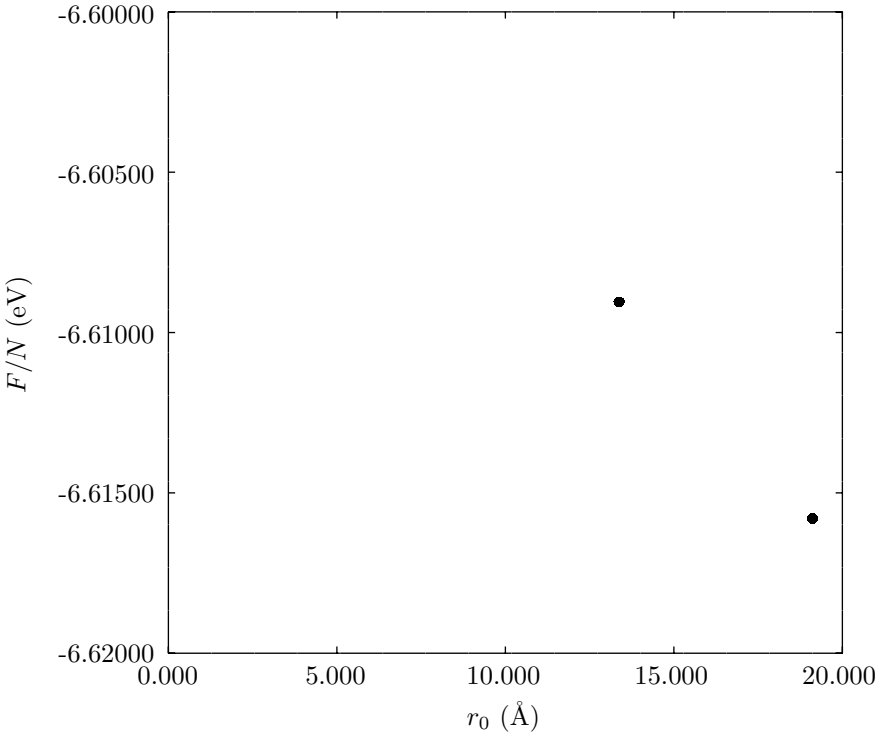

Figure A.35: Average energy per atom F/N vs. radius of curvature r_0 (zoomed in) for *zigzag* nanotube, where F is the total energy per primitive cell and N is the number of atoms in the primitive cell.

Bibliography

[1] Richard F. W. Bader. "A quantum theory of molecular structure and its applications". In: *Chemical Reviews* 91.5 (1991), pp. 893–928. DOI: 10.1021/cr00005a013. eprint: http://dx.doi.org/10.1021/cr00005a013. URL: http://dx.doi.org/10.1021/cr00005a013.

[2] Simone Bertolazzi, Jacopo Brivio, and Andras Kis. "Stretching and Breaking of Ultrathin MoS_2". In: *ACS Nano* 5.12 (2011), pp. 9703–9709.

[3] Peter E Blöchl. "Projector augmented-wave method". In: *Physical Review B* 50.24 (1994), p. 17953.

[4] K. D. Bronsema, J. L. De Boer, and F. Jellinek. "On the structure of molybdenum diselenide and disulfide". In: *Zeitschrift fur anorganische und allgemeine Chemie* 540.9-10 (1986), pp. 15–17. ISSN: 1521-3749. DOI: 10.1002/zaac.19865400904. URL: http://dx.doi.org/10.1002/zaac.19865400904.

[5] John W. Eaton et al. *GNU Octave version 4.0.0 manual: a high-level interactive language for numerical computations*. 2015. URL: http://www.gnu.org/software/octave/doc/interpreter.

[6] D. C. Elias et al. "Dirac cones reshaped by interaction effects in suspended graphene". In: *Nat Phys* 7.9 (Sept. 2011), pp. 701–704. ISSN: 1745-2473. DOI: 10.1038/nphys2049. URL: http://dx.doi.org/10.1038/nphys2049.

[7] Ji Feng et al. "Strain-engineered artificial atom as a broad-spectrum solar energy funnel". In: *Nat Photon* 6.12 (Dec. 2012), pp. 866–872. ISSN: 1749-4885. DOI: 10.1038/nphoton.2012.285. URL: http://dx.doi.org/10.1038/nphoton.2012.285.

[8] Guanghua Gao, Tahir Cagin, and William A Goddard III. "Energetics, structure, mechanical and vibrational properties of single-walled carbon nanotubes". In: *Nanotechnology* 9.3 (1998), p. 184.

[9] Jurgen Hafner et al. *Vienna Ab initio Simulation Package*. Version 4.6. 2015. URL: https://www.vasp.at/.

[10] A. Stephen K. Hashmi and Matthias Rudolph. "Gold catalysis in total synthesis". In: *Chem. Soc. Rev.* 37 (9 2008), pp. 1766–1775. DOI: 10.1039/B615629K. URL: http://dx.doi.org/10.1039/B615629K.

[11] W.M. Haynes. *CRC Handbook of Chemistry and Physics, 95th Edition*. CRC Press, 2014. ISBN: 9781482208689. URL: https://books.google.com.sg/books?id=bNDMBQAAQBAJ.

[12] Keliang He et al. "Experimental Demonstration of Continuous Electronic Structure Tuning via Strain in Atomically Thin MoS_2". In: *Nano Letters* 13.6 (2013), pp. 2931–2936.

[13] S. Helveg et al. "Atomic-Scale Structure of Single-Layer MoS_2 Nanoclusters". In: *Phys. Rev. Lett.* 84 (5 Jan. 2000), pp. 951–954. DOI: 10.1103/PhysRevLett.84.951. URL: http://link.aps.org/doi/10.1103/PhysRevLett.84.951.

[14] Graeme Henkelman, Andri Arnaldsson, and Hannes Jonsson. "A fast and robust algorithm for Bader decomposition of charge density". In: *Computational Materials Science* 36.3 (2006), pp. 354–360. ISSN: 0927-0256. DOI: http://dx.doi.org/10.1016/j.commatsci.2005.04.010. URL: http://www.sciencedirect.com/science/article/pii/S0927025605001849.

[15] Accelrys Software Inc. *BIOVIA Materials Studio*. Version 6.1. BIOVIA, 2012. URL: http://accelrys.com/products/collaborative-science/biovia-materials-studio/.

[16] Peng Lu et al. "Strain-dependent electronic and magnetic properties of MoS2 monolayer, bilayer, nanoribbons and nanotubes". In: *Phys. Chem. Chem. Phys.* 14 (37 2012), pp. 13035–13040. DOI: 10.1039/C2CP42181J. URL: http://dx.doi.org/10.1039/C2CP42181J.

[17] Kin Fai Mak et al. "Atomically Thin MoS_2: A New Direct-Gap Semiconductor". In: *Phys. Rev. Lett.* 105 (13 Sept. 2010), p. 136805.

[18] Mito. *PyDome Tutorial*. Australian Rocket Company blog. Mar. 21, 2013. URL: http://ausrockets.blogspot.sg/2013/03/pydome-tutorial.html.

[19] H. Mohwald. "Chapter 4 - Phospholipid Monolayers". In: *Structure and Dynamics of MembranesFrom Cells to Vesicles*. Ed. by R. Lipowsky and E. Sackmann. Vol. 1. Handbook of Biological Physics. North-Holland, 1995, pp. 161–211. DOI: http://dx.doi.org/10.1016/S1383-8121(06)80021-7. URL: http://www.sciencedirect.com/science/article/pii/S1383812106800217.

[20] Koichi Momma and Fujio Izumi. "*VESTA3* for three-dimensional visualization of crystal, volumetric and morphology data". In: *Journal of Applied Crystallography* (2011).

[21] John P. Perdew, Kieron Burke, and Matthias Ernzerhof. "Generalized Gradient Approximation Made Simple". In: *Phys. Rev. Lett.* 77 (18 Oct. 1996), pp. 3865–3868. DOI: 10.1103/PhysRevLett.77.3865. URL: http://link.aps.org/doi/10.1103/PhysRevLett.77.3865.

[22] D. Puotinen and R. E. Newnham. "The crystal structure of MoTe2". In: *Acta Crystallographica* 14.6 (1961), pp. 691–692. ISSN: 0365-110X. DOI: 10.1107/S0365110X61002084. URL: http://dx.doi.org/10.1107/S0365110X61002084.

[23] B. Radisavljevic et al. "Single-layer MoS_2 transistors". In: *Nat Nano* 6.3 (Mar. 2011), pp. 147–150. ISSN: 1748-3387.

[24] J. C. Slater. "Atomic Radii in Crystals". In: *The Journal of Chemical Physics* 41.10 (1964), pp. 3199–3204. DOI: http://dx.doi.org/10.1063/1.1725697. URL: http://scitation.aip.org/content/aip/journal/jcp/41/10/10.1063/1.1725697.

[25] Timothy B. Terriberry. *Vasp Data Viewer*. Version 1.05. 2001.

[26] Qing Hua Wang et al. "Electronics and optoelectronics of two-dimensional transition metal dichalcogenides". In: *Nature nanotechnology* 7.11 (2012), pp. 699–712.

[27] J. C. Wildervanck and F. Jellinek. "Preparation and Crystallinity of Molybdenum and Tungsten Sulfides". In: *Zeitschrift fur anorganische und allgemeine Chemie* 328.5-6 (1964), pp. 309–318. ISSN: 1521-3749. DOI: 10.1002/zaac.19643280514. URL: http://dx.doi.org/10.1002/zaac.19643280514.

[28] Mark Winter. *WebElements Periodic Table*. The University of Sheffield. URL: http://www.webelements.com/.